University of California
Los Angeles

Particle Geometry and Its Effect on Optical Trapping

A dissertation submitted in partial satisfaction
of the requirements for the degree
Doctor of Philosophy in Chemistry

by

Rachael Victoria Harper

2013

Abstract of the Dissertation

Particle Geometry and Its Effect on Optical Trapping

by

Rachael Victoria Harper

Doctor of Philosophy in Chemistry

University of California, Los Angeles, 2013

Professor Alex J. Levine, Chair

The ability to manipulate small particles with light has opened new avenues for synthesis and experimentation. Building upon expansive previous work in the theoretical study of light scattering, the forces which make optical manipulation of matter possible have been extensively studied both analytically and computationally. In this dissertation we will examine the forces on complex particle geometries, in the presence of a focused beam of light, using a two dimensional geometric optics simulation. We begin with a brief overview on the background of optical trapping as well as the theoretical approaches available to model optical trapping forces both analytically and numerically. The results of our numerical geometric optics simulation are shown to be in exact agreement with a previously published, closed form, analytic solution for the optical forces on a solid homogeneous sphere in the geometric optics regime.[1] The trapping behavior of two dimensional circles with an inner cavity of varying size is then investigated. Generalized Lorenz-Mie theory is employed to calculate the force on the particle interacting with an unfocused beam. An infinite cylinder with an inner cavity size on the order of the wavelength of incident light and an unfocused beam, incident normal to the cylinder axis, are used. This result is compared to that found with our geometric optics

simulation. We find that, for an inner cavity diameter an order of magnitude or smaller than the wavelength of the incident light, the geometric optics simulation underestimates this force. The same holds true for very large inner cavities, where the dielectric wall thickness is less than half the wavelength. For cavity sizes between these two extremes we find the geometric optics simulation overestimates the force in the direction of beam incidence, by as much as a factor of two. Finally the effect of breaking axial symmetry on the trapping behavior of a two dimensional planar shape is studied qualitatively using an analytic approach and quantitatively using the geometric optics simulation. Beginning with an axially symmetric rectangular shape, a small leg is added and the trapping behavior as well as the torques examined. We find stable trapping and balanced torques, with the long axis of the shape both parallel and perpendicular to the direction of beam incidence, for an axially symmetric rectangle. Once axial symmetry is broken all trapping is found to occur with the long axis perpendicular to the direction of beam incidence and the lowest plane of the shape above the focal point of the beam.

The dissertation of Rachael Victoria Harper is approved.

Robijn Bruinsma

Miguel A. Garcia-Garibay

William M. Gelbart

Alex J. Levine, Committee Chair

University of California, Los Angeles

2013

To my Grandfathers,

William Edward von Kaenel, M.D.

and

Ernest Embree Harper II

We've never met but you've been a part of my life through stories told by some of the most incredible people I know.

Table of Contents

List of Figures

Acknowledgments

I would like to express my deep appreciation and gratitude to my advisor, Professor Alex J. Levine, for years of teaching, guidance and patience. Thank you for teaching me that intellectual capacity is attached to hard work rather than innate ability. I would like to thank the members of my dissertation committee, Professor William Gelbart, Professor Miguel Garcia-Garibay and Professor Robijn Bruinsma for all they have taught me as well as their continued support and advocacy. I am indebted to Dr. James Wilking and Professor Thomas Mason, for invaluable experimental data on the optical trapping of colloidal dielectric particles.

I have been incredibly fortunate to have amazing and supportive people in my life. Dr. Glenna Sowa has been both a mentor and friend from the beginning of my graduate career to this day, thank you for being there every step of the path. Steve Macy, Tina Clifford and Kevin Evey first helped me find my way. Rodney Oka inspired me to be even half the teacher he was to me. Professor Nick Winter, Professor Ilan Benjamin and Professor Jin Zhang first introduced me to research, physical chemistry and the idea of grad school.

Veronica Strong thank you for lost erasers in coffee cups, absurd games no one else would want to play, making me get in the car and the opportunity to experience having a sister. Jon Strong, thank you for sneak attack oil changes, home security and repair, suffering through nine thousand conversations about science, cut-throat UNO games and for keeping us all functional. Yuen Lau thank you for being there at three am, for remembering every birthday, and your boundless capacity for love and devotion to your friends. Lisa Dudek, thank you for endless trips to mailboxes, drives to the OC, lady science days and for consistently looking for the best in people. I can honestly say this

dissertation would not have been completed without you.

I have to thank my Grandma Donna and Grandma Jean for showing me what stubborn, smart and spirited look like. My cousin, Krystal Owens, is an inspiration. Tatay Ted, Tito Edgardo, Tita Deng, Pam and the entire Lacbay clan, thank you for welcoming me with open arms and making me a part of the family.

My Mom is the reason I started back to school and is unwavering in her belief that I can do anything. My Dad is the person who taught me to keep showing up, that science was an option and who I count on to tell me when I am wrong. My brother is by far my most enthusiastic supporter and my model for a life well lived.

Finally, Vince, thank you for being a bottomless fount of support, for rolling with all the punches, for laundry, sinigang and giniling, for patience, back scratches, computer fixes, and boundless love. I can not wait to start our lives together.

Vita

1977	Born, Santa Clara, California, USA.
2006	B.S. (Chemistry), University of California, Santa Cruz.
2006–2010	Teaching Assistant, Department of Chemistry and Biochemistry, UCLA.
2010-2011	SEE-LA NSF GK-12 Graduate Fellow, UCLA.
2011–2012	Teaching Assistant, Department of Chemistry and Biochemistry, UCLA.
2012 – present	Research Scientist, Applied Medical Resources.

CHAPTER 1

Introduction

Since the seminal work of Arthur Ashkin,[2] that demonstrated the acceleration and trapping of dielectric particles by a single focused laser beam, optical trapping has been an invaluable and much utilized tool. Optical trapping has been used to manipulate particles with length scales from the tens of nanometers to the hundreds of microns; it has measured forces ranging from femtonewtons to nanonewtons and has done so on time scales ranging upward from the microsecond.[3] An invaluable experimental tool, optical tweezers have been used to probe the force generated by the portal complex as it packs double stranded DNA into a viral capsid,[4] the isometric forces generated by single molecules of kinesin[5] and the mechanical properties of red blood cells in different osmotic conditions.[6] The trapping ability of single beam optical tweezers is not limited to single biological molecules; they have been used to trap individual gold nanorods,[7] to probe the deformation mechanics of lipid bilayers,[8] and to examine how particle symmetry effects the trapping behavior of micron sized particles.[9] Ashkin's early work with single beam optical traps has been extended to a variety of trap shapes; including holographic optical trapping arrays,[10–13] anisotropic traps generated by scanning the beam along a single line,[14–16] optical vortex traps,[17–19] traps generated using zeroeth-order Bessel beams,[20,21] and optical traps which abandon the beam completely and use the evanescent field of a waveguide.[22]

Optical trapping and scattering has also been extensively studied using

theoretical methods. A short, and hardly exhaustive, list of methods includes Generalized Lorenz-Mie Theory, The Discrete-Dipole Approximation, Geometric Optics and Rayleigh Scattering.

Generalized Lorenz-Mie Theory (GLMT), which applies Maxwell's equations to an electromagnetic wave illuminating a homogeneous sphere of known size and refractive index,[23] provides an exact analytical description of the scattered fields and, as a result, the forces imparted to the dielectric particle. As no approximations are made the GLMT provides accurate results for particles on all length scales. The GLMT dependence on partial wave vectors, however, limits its application to spherical or cylindrical particles. The GLMT has been used to describe the forces on a spherical dielectric particle arbitrarily located in relation to the focal point of a single beam gradient trap,[24,25] scattering from multilayer concentric spheres[26] or infinite cylinders,[27] and to calculate the stresses on homogeneous spheroids in an optical stretcher.[28]

The Discrete Dipole Approximation (DDA), first developed by Purcell and Pennypacker,[29] treats any dielectric particle as a collection of discrete dipoles, which interact with each other and the incident field. These interactions give rise to a system of linear equations. This system of linear equations can be solved for the dipole polarizations, from which all scattering quantities can be obtained.[30] The discrete nature of the DDA makes it possible to model all geometries, however the approximation is only applicable on length scales on the order of, or smaller than, the wavelength of the incident light. The DDA has been used to calculate the forces on a spherical dielectric particle,[31] to calculate the radiation pressure cross section for fluffy aggregates,[32] to calculate the laser trapping particles on non-spherical particles[33] and to explicitly compute the gradient and non-gradient components of the optical force on neutral, polarizable particles in a field.[34]

Geometric optics treats incident light as a collection of discrete rays; as a

result the Geometric Optics approximation is only valid if the particle being investigated is much larger than the wavelength of the incident light. Rayleigh Scattering is applicable if the particle is much smaller than the wavelength of incident light and can therefore be treated as a single discrete dipole. The theory and history of both geometric optics and Rayleigh scattering will be discussed in greater detail in the next section.

1.1 Optical trapping background

To understand the forces that drive optical trapping one can begin with electrostatics, specifically the force on a dielectric slab inside a parallel place capacitor. The presence of an external, static, electric field serves to polarize the dielectric. As the force on a single electric dipole within the dielectric is given as $\mathbf{F}_{dipole} = (\mathbf{p} \cdot \nabla)\,\mathbf{E}$ the total force on the dielectric slab can be found by integrating the force on each individual dipole over the volume of the dielectric

$$\mathbf{F}_{dielectric} = \iiint (\mathbf{P} \cdot \nabla)\,\mathbf{E}\; d\tau, \tag{1.1}$$

where $\mathbf{P}$ is the polarizability of the material, $\mathbf{E}$ is the electric field of the capacitor and $d\tau$ is the volume element. We note from equation 1.1 that any forces on the dielectric require an electric field gradient, which cannot exist within the parallel plate capacitor. Rather the fringe fields at the edges of the capacitor, illustrated in figure 1.1, generate forces which serve to pull the dielectric slab into the capacitor. These forces are driven by a lowering of the overall potential energy of the system; moving the dielectric into the parallel plate capacitor places material with greater polarizability into the high field region, decreasing the energy between the plates. Returning to equation 1.1, we see that increasing the electric field gradient serves to increase the force. From Gauss's law, these field gradients (which are necessary for a potential minimum) are not possible in a static field in the absence of charge density,

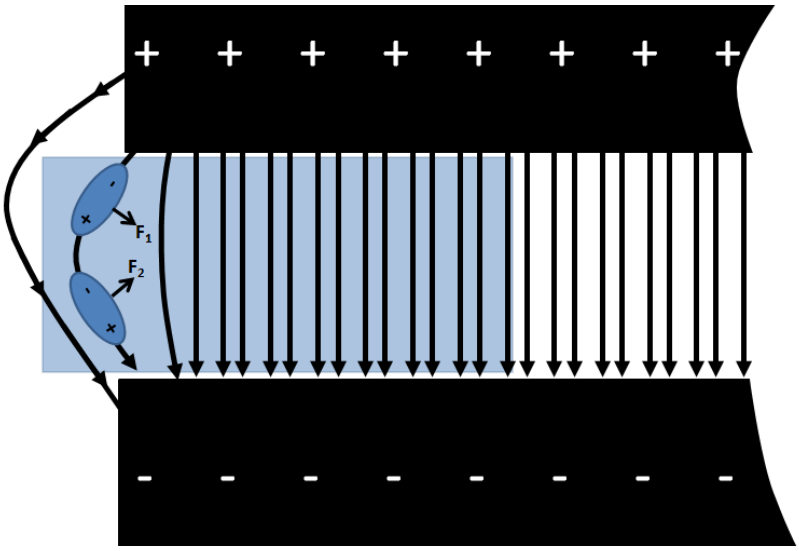

Figure 1.1: The fringe fields and forces resulting from individual dipoles for a dielectric slab partially inserted into a parallel plate capacitor.

$\nabla \cdot \mathbf{E} = \rho$. This is commonly expressed as Earnshaw's theorem, it is not possible to electrostatically generate a local minima or maxima of the field potential only saddle points. A stable equilibrium position for the particle within the electric field cannot exist.

Dynamically one can generate a large field gradient in the absence of charge density. The electric and magnetic fields that make up light can be highly focused, giving rise to exactly the electric field gradients necessary to generate stable trapping. Using a highly focused beam of light does not simply generate a trapping, or *gradient force*. As light carries momentum any changes to the light's momentum vector will result in a force. In optical trapping applications changes in the light's momentum are due to reflection or refraction, and will result in an equal and opposite change to the body which caused the reflection or refraction. Termed the *scattering force*, in the physical optics regime this force can be in any direction. In the geometric optics regime the gradient force refers to any forces which act to restore the particle to the focal point of the beam and the scattering force refers to any forces which push

the particle away from it. For the remainder of this dissertation the geometric optics definition of the terms scattering and gradient force will be used.

1.1.0.1 The Rayleigh Regime

Limiting ourselves, momentarily, to the Rayleigh regime, wherein the particle diameter is much less than the wavelength of the incident light, we can treat a spherical dielectric particle in this regime essentially as a collection of dipoles. The polarization is therefore given as[35]

$$\mathbf{P} = n_b^2 \left(\frac{n^2 - 1}{n^2 + 2} \right) r^3 \mathbf{E} = \alpha \mathbf{E}, \tag{1.2}$$

where n_b is the refractive index of the media surrounding the dielectric, $n = \frac{n_a}{n_b}$, n_a is the refractive index of the dielectric sphere, r is the sphere radius and α is the polarizability of the sphere in the surrounding dielectric media. As we can treat the sphere as a dipole the force due to the dipoles interaction with the electric field gradient, or the *gradient force*, can be expressed as

$$\mathbf{F}_{grad} = (\mathbf{P} \cdot \nabla)\, \mathbf{E} = \frac{\alpha \nabla E_\circ^2}{2}. \tag{1.3}$$

Using light to generate the high electric field gradient necessary to trap the particle does not come without an associated cost. From Maxwell's equations, $\nabla \times \mathbf{E} = -\frac{\delta \mathbf{B}}{\delta t}$, the electric field comes with an associated magnetic field. Light therefore carries momentum,

$$\mathbf{p} = \sqrt{\frac{\epsilon_\circ}{\mu_\circ}}\, (\mathbf{E} \times \mathbf{B})\,. \tag{1.4}$$

This light is scattered from within the dielectric sphere and off its surface. As momentum must be conserved each scattering event results in a force, the *scattering force*,

$$\mathbf{F}_{scatt} = \frac{d\mathbf{p}}{dt}. \tag{1.5}$$

It is the balance of these two forces which results in stable trapping, with the scattering force pushing the particle away from the region or high gradient, or the focal point of the beam, and the gradient force pulling it back.

1.1.0.2 Geometric Optics Regime

One can understand trapping in the geometric optics approach as long as one recognizes that light carries momentum. Reflection and refraction events, analyzed within the geometric optics framework, then result in a momentum transfer between the beam and the object. This allows computation of the force exerted by the light field in its interaction with the object. Conservation of momentum accounts for both the gradient and scattering forces in the geometric optics regime, where the particle diameter is much larger than the wavelength of the incident light. In this regime the particle cannot be treated as a dipole and instead acts as a lens, redirecting the incident light. From Fermat's principle light traveling through any homogeneous medium will always travel the shortest possible optical path. In media with spatially homogeneous indices of refraction this results in straight line paths. These straight line segments, termed rays, can describe the path of a beam of light between intersections with the dielectric interfaces. Following Ashkin's first experiments with optical levitation[2] Roosen and Imbert[36] used geometric optics to calculate the forces parallel and perpendicular to the direction or propagation for two parallel laser beams.

$$\begin{aligned}\mathbf{F}^{\parallel} &= -\int_0^{\pi/2} d\theta \int_0^{2\pi} d\phi \left[\frac{E^2 r^2}{\mu_\circ c^2} \sin\theta_i \cos\theta_i\right] \\ &\times \left[R\cos 2\theta_i + 1 - \frac{T^2(\cos 2(\theta_i - \theta_t) + R\cos 2\theta_i)}{1 + R^2 + 2R\cos 2\theta_t}\right], \qquad (1.6)\\ \mathbf{F}^{\perp} &= -\int_0^{\pi/2} d\theta \int_0^{2\pi} d\phi \left[\frac{E^2 r^2}{\mu_\circ c^2} \sin^2\theta_i \sin\phi\right] \\ &\times \left[R\sin\theta_i - \frac{T^2(\sin 2(\theta_i - \theta_t) + R\sin 2\theta_i)}{1 + R^2 + 2R\cos 2\theta_t}\right], \qquad (1.7)\end{aligned}$$

where θ_i and θ_t are the angles of incidence and transmission, ϕ is the azimuthal angle, measured from the vector normal to the perpendicular and parallel directions. The terms R and T are the Fresnel coefficients which, averaged over polarizations, can be expressed as

$$R_{avg} = \frac{1}{2}\left[\left(\frac{n_b\cos\theta_i - n_a\cos\theta_t}{n_b\cos\theta_i + n_a\cos\theta_t}\right)^2 + \left(\frac{n_a\cos\theta_i - n_b\cos\theta_t}{n_b\cos\theta_t + n_a\cos\theta_i}\right)^2\right], \tag{1.8}$$

$$T_{avg} = \frac{n_a\cos\theta_t}{n_b\cos\theta_i}\left[\left(\frac{2n_b\cos\theta_i}{n_b\cos\theta_i + n_a\cos\theta_t}\right)^2 + \left(\frac{2n_b\cos\theta_i}{n_b\cos\theta_t + n_a\cos\theta_i}\right)^2\right]. \tag{1.9}$$

Roosen and Imbert assumed that the light intensity within the beam had a Gaussian profile, peaked at the beam's center and having a $\frac{1}{2}$ width of w. The electric field intensity is then given by

$$E^2 = E_\circ^2 exp\left[-\frac{2\left(r^2\sin^2\theta_i + \rho_\circ^2 - 2r\rho_\circ\sin\theta_i\sin\phi\right)}{w^2}\right], \tag{1.10}$$

where $\rho_\circ$ is the distance between the beam axis and the center of the sphere.

1.2 Ashkin's closed form solution

Building upon Roosen and Imbert's calculations, Ashkin was able to derive a closed form solution for the scattering and gradient forces on a spherical particle in the geometric optics regime. On the basis that a Gaussian beam profile provided a poor description of the high convergence beams used in good traps[37] the beam waist was instead treated as a point. By using a discrete point and the highly symmetric spherical dielectric shape, Ashkin was able to define the angles of incidence, transmission and reflection for an infinite number of intersections made by a single ray. As is illustrated in figure 1.2, for a single ray of power P at the first point of intersection some fraction of the incident power will be reflected, carrying power PR, where R is the Fresnel coefficient in equation 1.8. The transmitted ray will carry a fraction of the

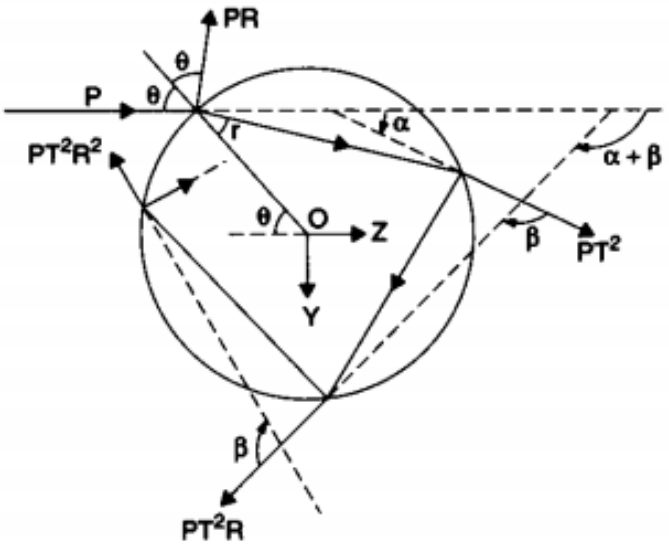

Figure 1.2: The angles and fractions of power carried for each intersection of single ray with a homogeneous spherical particle in the geometric optics regime. Used with permission © Biophysical Society.

initial power, PT. At the first intersection of the transmitted ray, a fraction of the power being carried, PT will be reflected and carry power PTR and a fraction will be transmitted, carrying away power PT^2. Following Ashkin's derivation,[37] the force resulting from a single ray in directions both parallel and perpendicular to the direction of beam propagation can be expressed as

$$F^{\parallel} = \frac{n_b P}{c} - \left[\frac{n_b PR}{c} \cos(\pi + 2\theta_i) + \sum_{n=0}^{\infty} \frac{n_b P}{c} T^2 R^n \cos(\alpha + n\beta) \right], \quad (1.11)$$

$$F^{\perp} = 0 - \left[\frac{n_b PR}{c} \sin(\pi + 2\theta_i) - \sum_{n=0}^{\infty} \frac{n_b P}{c} T^2 R^n \sin(\alpha + \beta) \right], \quad (1.12)$$

where $\alpha = 2\theta_i - 2\theta_t$ and $\beta = \pi - 2\theta_t$. As suggested by Ashkin,[37] Roosen[36] and van de Hulst,[38] one can sum the total rays scattered by a sphere by considering the total force in the complex plane, $F_{tot} = F^{\parallel} + iF^{\perp}$, which gives

$$F_{tot} = \frac{n_b P}{c} \left(1 + R\cos 2\theta + iR \sin 2\theta - T^2 \sum_{n=0}^{\infty} R^n e^{i(\alpha + n\beta)} \right). \quad (1.13)$$

Substituting the value of the convergent geometric series, rationalizing the complex denominator and taking the real and imaginary parts of equation 1.13 one can, with a good deal of algebraic manipulation, arrive at the following expressions:

$$F^{\parallel} = \frac{n_b P}{c}\left(1 + R\cos 2\theta_i - \frac{T^2\left[\cos\left(2\theta_i - 2\theta_t\right) + R\cos 2\theta_i\right]}{1 + R^2 + 2R\cos 2\theta_t}\right), \tag{1.14}$$

$$F^{\perp} = \frac{n_b P}{c}\left(R\sin 2\theta_i - \frac{T^2\left[\sin\left(\left(2\theta_i - 2\theta_t\right) + R\sin 2\theta_i\right]\right.}{1 + R^2 + 2R\cos 2\theta_t}\right). \tag{1.15}$$

Using equations 1.14 and 1.15 one can account for the momentum transferred per second by a single ray to a spherical particle. By integrating over the area of the beam aperture, the total scattering force, $F^{\parallel}$ and gradient force, $F^{\perp}$ can be calculated. Additionally as the beam is simply described as a set of rays, beams of complex intensity profile can be modeled.

The geometric optics approach was first expanded to account for the intensity profile of the beam being used by Gauthier,[39] in an approach called "the photon stream method". Using rays to define the path of a stream of photons, Gauthier developed analytic expressions for the force components perpendicular and parallel to the direction of beam incidence acting upon a solid dielectric sphere in the presence of a Gaussian beam profile. This work was later applied to systems with both transparent and perfectly reflecting spheres in the presence of a Gaussian beam,[40] for spheres suspended in inhomogeneous media[41] and used as a means to design optimized optical trapping systems.[42] Using Ashkin's definitions for the scattering and gradient force, Zhou and coworkers[43] used a vector ray tracing approach to numerically model the forces on a solid dielectric sphere in the presence of both Gaussian and circularly polarized beam profiles.

Homogeneous spheres and the forces upon them in the presence of a beam are well understood. Inhomogeneous spherical particles have also been studied extensively. Initial work focused on the trapping behavior of composite

microspheres composed of layers of differing dielectric indices.[19,44–47] With the advent of lab on a chip systems, interest was peaked in the trapping and sorting of double emulsion spheres[48,49] and lipid vesicles.[50] Later work pushed the lower limits of vesicle diameter down to 50 nm; experimentally trapping unilamellar lipid vesicles with a high refractive index sucrose core.[51]

Interest in the trapping behavior of symmetric particles is not limited to spheres. The trapping of cylindrical and rod shaped particles has been studied both in light of the torques inherent to a rod shaped particle[52–54] and for biological molecules, for example *E. Coli*.[13,55] The vector ray tracing approach was recently applied by Zhou and coworkers[56] in computational simulations to model the forces and torques on an ellipsoidal particle in the presence of a Gaussian beam. Sraj and coworkers[57] used a similar approach to simulate the transient deformation of spherical, ellipsoidal and biconcave capsules due to optical forces resulting from particle interaction with a single diode bar optical trap.

1.3 Thesis overview

Ashkin's research allowed a close approximation of the scattering and gradient forces for any incident beam interacting with a spherical dielectric particle with radii much larger than the wavelength of incident light. For more complex shapes, for example shapes with multiple cavities or non-symmetric geometries, Ashkin's approach becomes intractable. An example of the dependence of trapping behavior on particle geometry is beautifully illustrated in Wilking and Mason's[9] experiments in which they examined the effect of particle shape on the trapping force for a series of polymeric colloidal particles constructed using photolithographic techniques. They studied the trapping forces on the letters of the Latin alphabet and found that, even for an essen-

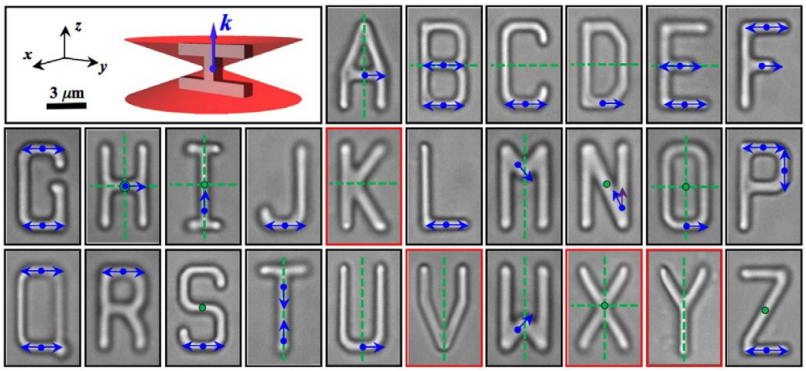

Figure 1.3: Trapping behavior of the colloidal dielectric alphabet, with particle dimensions 4 μm $\times$ 7 μm $\times$ 1 μm. The particles were trapped using an expanded TEM_{00} Gaussian beam at a maximum laser power of 17 mW and wavelength $\lambda = 633$nm. Blue arrows denote the direction of beam propagation and blue circles the focal point of the beam when stable trapping occurred. Red squares mark shapes that do not trap. Green lines and circles denote mirror planes and twofold rotation axes, respectively. Used with permission © Europhysics Letters Association.

tially fixed amount of the same dielectric material for each letter, some letters were not able to be trapped, some could be trapped in only one position and orientation, while some had multiple trapping positions and orientations, as illustrated in figure 1.3. This trapping behavior of complex shapes and the viability of modeling the trapping behavior of any shape, using computational geometric ray optics simulations, is the focus of this dissertation. Utilizing Ashkin's beam decomposition approach we focus on the momentum transfer at each intersection of each ray of the beam at the interface of two dielectric media; as any particle geometry can be decomposed into a set of interfaces. Summing the momentum transfer at each intersection generates the net momentum transfer to the particle.

1.3.1 Ray optics simulations

While the generation of a transmitted and reflected ray at each intersection would appear to generate an unbounded and steady increase in the number of rays to account for, there are two mitigating factors. First as the momentum transfer is being calculated for a single dielectric body, any rays which are directed away from the particle are accounted for and then no longer tracked. Second, at each intersection of the ray with the interface from higher dielectric to lower the bulk of the momentum is refracted, and we find convergence within $\mathcal{O}(10^{-4})$, accounting for six or less intersections of each ray. As will be discussed and demonstrated in the next chapter, we find close agreement with Ashkin's closed form solution for a solid dielectric sphere using this approach. Additionally an overview of the functions and parameters used in our simulations for any shape will be given.

1.3.2 Increased scattering interfaces

The natural first step in increasing shape complexity is to add to the number of scattering interfaces. In chapter three the force field, or a map of the forces acting upon a particle held statically at some position relative to the focal point of the beam, are presented. Force field plots for a two dimensional system consisting of a high numerical aperture beam and a circular dielectric with a cavity, the size of which is steadily increased, are shown. This is an ideal test system as the effect of cavity size on the forces imparted to the particle by the beam can be predicted on the basis of electrodynamics and experimental results for similar shapes from the previous work of Wilking.[9]

One would expect the addition of a cavity to increase the force in the direction of beam incidence as there are now more interfaces off which the incident light can scatter. The gradient force should also decrease as there is less dielec-

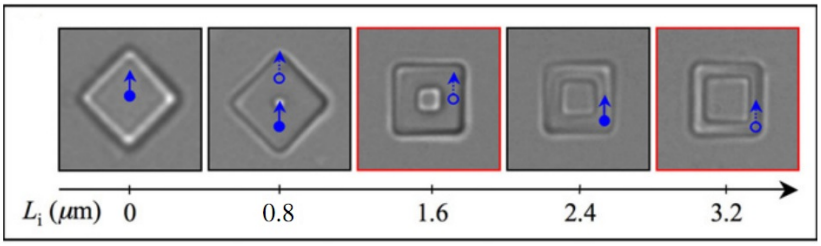

Figure 1.4: Trapping behavior of the colloidal dielectric square plate-like particle, outer edge length $L_\circ = 4.5\mu$m and inner cavity dimensions L_i. Used with permission © Europhysics Letters Association.

tric material to be drawn in the direction of highest field gradient. As a result the point at which the gradient force balances the scattering force should shift away from the focal point of the beam, in the direction of beam propagation. By symmetry the circular shape will trap with its center aligned with the center of the beam; any shift perpendicular to the direction of beam propagation will result in a restoring gradient force towards the center of the beam.

From our numerical simulations we find the results agree with expectations. Increasing the size of the inner cavity shifts the stable trapping point for the shape away from the beam waist, in the direction of beam incidence. For cavity sizes small relative to the radius of the circle the simulated stable trapping point is close to that found experimentally by Wilking for a similar shape, illustrated in figure 1.4. As the cavity size is increased, however, we find that stable trapping is lost. This in contradiction to the experimental findings of Wilking. Defining L_i as the inner cavity diameter or length and $L_\circ$ as the outer edge length, Wilking's experiments show the expected loss of trapping for $\frac{L_i}{L_\circ} = 0.35$, stable trapping for $\frac{L_i}{L_\circ} = 0.53$ and a loss of trapping once again for $\frac{L_i}{L_\circ} = 0.71$. We posit the cause of this disagreement is twofold. Firstly ray optics does not account for diffraction and should therefore overestimate the scattering force, which will be discussed in detail in following sections. Secondly there are gradient forces resulting from the third plane of the dielec-

tric, coming into and out of the plane in figure 1.4, which are unaccounted for in the two dimensional simulations performed. These forces will be discussed in the next section, which examines the trapping behavior of a planar shape.

1.3.3 Breaking rotational symmetry

A reasonable approach to increasing the complexity of shape trapping behavior, beyond adding cavities, is to break the rotational symmetry of the particle. Within the set of shapes experimentally studied by Wilking, the simplest example of a non-rotationally symmetric shape is that of the L. Experimentally an L shape traps with the bulk of the scattering surfaces shifted out of the beam and the shorter leg oriented parallel to direction of beam incidence, as is illustrated in figure 1.3. Trapping a non-rotationally symmetric shape opens the possibility that while the scattering and gradient forces are in balance there can simultaneously be an unbalanced set of torques acting upon the shape, due to its interaction with the beam. In chapter five we investigate the role lack of rotational symmetry plays in the trapping behavior of a planar shape with two and then one plane of symmetry. Starting with a two dimensional rectangular shape, length $l_\circ$ and unit width, we add a small perpendicular segment, length l_i, and slowly increase its length, examining the resulting effect on both the trapping behavior and torques.

Each shape was allowed to sample the full field at all angles θ, with theta measured counterclockwise from the positive axis of beam incidence and $\Delta\theta = \frac{\pi}{50}$. For a rectangle length $l_\circ = 7\,\mu$m we find stable trapping for $0 \leq l_i \leq 0.3$ μm. Trapping is lost for values of $0.4\,\mu\text{m} \leq l_i \leq 2.2\,\mu$m and reemerges for values $2.3\,\mu\text{m}\ l_i \leq 3.0\,\mu$m, where $\Delta l_i = 0.1$. In the case of $l_i = 0$ stable trapping was found with the long axis of the rectangle oriented both parallel, $\theta = 0$, and perpendicular, $\theta = \pm\frac{\pi}{2}$ to the direction of beam incidence. All other values of l_i, for which stable trapping occurred, the long axis of the shape was oriented

perpendicular to the direction of beam incidence. In the single parallel case, $l_i = 0$, $\theta = 0$ the base of the shape was located slightly below the focal point of the beam. All perpendicular trapping occurred with the lowest boundary of the shape located above the beam's focal point.

While this trapping behavior diverges from that found experimentally by Wilking, it is the expected result from analytic ray optics calculations; outlined in chapter 5. Briefly, for two planar interfaces any internal ray intersecting an interface perpendicular to the interface from which it originated will experience a switch in the magnitude of its x and y components upon refraction to the lower index media. Any internal ray intersecting an interface parallel to the interface from which it originated will refract at an angle equal to its angle of incidence at its first low index to high index intersection. Parallel interface intersections can therefore only contribute a scattering force, pushing the particle away from the focal point of the beam, due to internal reflections. Intersections between perpendicular interfaces can contribute either a scattering or gradient force. Additionally these perpendicular intersections lead to total internal reflection for any ray which made its first intersection with the shape at angles smaller than $\theta_c = \sin^{-1}\left(\sqrt{\frac{n_b}{n_a}}\right)$.

Returning to the possible causes of the simulation's departure from Wilking's experimental results, discussed in section 1.3.2, and consulting figure 1.4, a possible cause for this disagreement is illustrated. If one imagines a line passing vertically through the beam axis shown in fig 1.4, $L_i = 2.4\mu m$, the incident rays are separated into those with positive and negative $\mathbf{k}_x$ components. For the rays on the left side of the beam axis all initial intersections are with the base of the shape. Even accounting for the transmitted ray bending inward towards the unit normal, the bulk of the rays will go on to intersect the right-most vertical boundary of the dielectric. At the second intersection the ray transmits with a larger $\mathbf{k}_y$ component than it had at the first intersection.

The net result for these two intersections is a gradient force.

For rays entering with $\mathbf{k}_x < 0$ there are two possible interfaces with which the ray can make its first intersection, the vertical dielectric boundary, or the base. In the case of initial intersection with the wall the ray can go on to intersect the parallel inner dielectric boundary, with the resulting internal transmitted ray going on to pass through the two parallel interfaces making up the top of the shape. This parallel interface to parallel interface passage generates no change in $\mathbf{k}_y$. A second possible path for the rays first intersecting the wall is to internally intersect the lower inner boundary of the dielectric. Each of these intersections will result in a transmitted ray with $\mathbf{k}_y$ less than that of the initial ray. In these interactions there is a net positive $\hat{y}$ momentum transfer to the particle. Incident rays with $\mathbf{k}_x > 0$ will either totally internally reflect, due to their small angles of incidence with the perpendicular right-most dielectric boundary, or will transmit. Each of these transmitted rays will carry $\mathbf{k}_y$ momentum in a greater fraction than they left the laser aperture with. As a result, each of these rays will contribute an overall negative net $\hat{y}$ force on the particle. For rays that experience total internal reflection upon reaching the top boundary of the dielectric they will transmit at an angle equal to their angle of incidence. These rays will therefore make no net contribution to the $\mathbf{k}_y$ component of the particle's momentum.

While this qualitatively explains the torque balance for the shape at its stable trapping position it does not go very far in explaining the total gradient force being high enough to generate stable trapping. If one, however, were to rotate the particle which displays reentrant trapping about the beam axis by $\frac{\pi}{2}$ the overall trapping behavior of the shape remains unchanged as the beam is symmetric about its central axis. The shape we are able to examine however, following this rotation, is now a plank. In the stable trapping position some of the incident rays will intersect the base of the plank and go on to

internally intersect a perpendicular wall, contributing to the gradient force. Some of the incident rays will intersect the side of the shape and go on to internally intersect a parallel wall, making no contribution to the scattering force. As the simulations were done in two dimensions they fail to account for the particle's second characteristic geometry. Additionally as a circular rather than planar structure was used in the initial simulations the effect of parallel and perpendicular interfaces would not be seen.

Regardless of the particle shape the possibility remains that stable trapping points will be missed by the simulation if any of the particles dimensions are on the order of, or smaller than, the wavelength of the incident light. The ray optics approach, which allows one to account for the dielectric boundaries simply using Euclidean geometries, comes at the cost of neglecting the effects of diffraction.

1.3.4 Effects that cannot be accounted for with Geometric Optics

1.3.4.1 Diffraction

For large spheres with diameters much larger than λ the diffraction contribution to the total forces on the particle are small enough that they can be safely neglected[38,58,59] . From the standpoint of the numerical simulations discussed in this dissertation it is fairly straightforward to add cavities within the particle much smaller than the wavelength of incident light or to design particles consisting of an array of diffractive knife edges. Doing so, however, introduces new forces that are attributed to either the wave or electromagnetic nature of light with diffraction resulting in the first regime and dipole scattering in the later. The classic geometric optics approach was originally modified to account for diffraction by Keller.[60] From the pure geometric optics standpoint, the interaction of the ray with the dielectric media is binary. The ray either

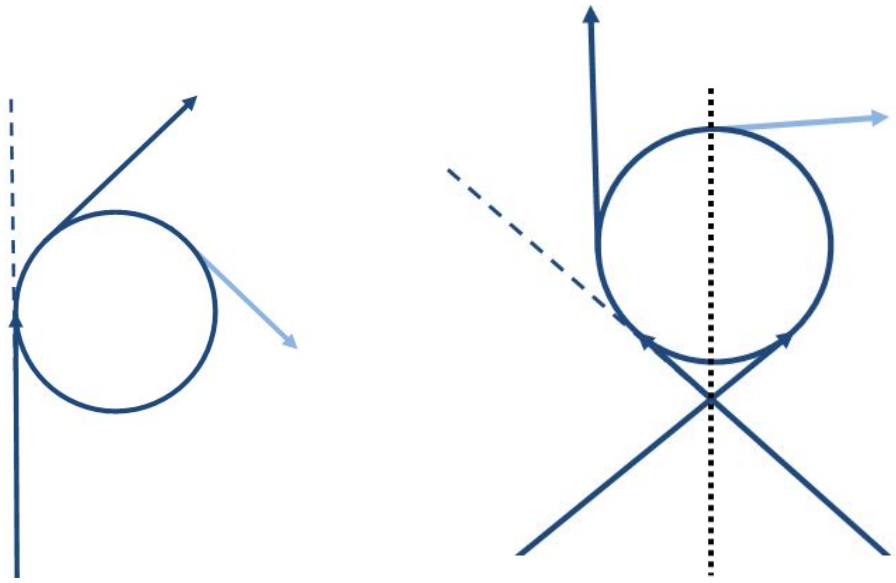

(a) Diffracted ray contributing to the scattering force.

(b) Diffracted ray contributing to the gradient force.

Figure 1.5: A ray path for which diffraction can contribute to the scattering force, figure 1.5a; where in the ray loses a portion of the $\mathbf{k}_y$ component of its incident momentum and transfers the same amount to the particle. A ray path for which diffraction can contribute to the gradient force on the particle, figure 1.5b. The second mirrored ray is included to define the point of highest beam focus and illustrate a position for the particle, relative to the beam, where gradient forces due to diffraction are likely to happen.

intersects, transferring some of its momentum in the process, or it misses the dielectric completely; making no impact on the particle's net momentum. We know this is not true that rays, in fact, diffract around small objects, and in doing so diverge slightly from their previous path, imparting a change in the particle's momentum. This change can contribute to either the scattering or gradient force, as is illustrated in figures 1.5.

1.3.4.2 Dipole Scattering

The Dipole scattering approximation can be applied if the characteristic dimensions of the particle are much smaller than the wavelength of the incident light. In this regime the particle is too small for the wave to diffract around and instead the electromagnetic fields which make up the Poynting vector interact with the particle as though it were a dipole, inducing electric and magnetic multipoles which can oscillate in definite phase relationship with the incident waves. These oscillations radiate energy in directions other than that of incidence.[61] The radiated fields can add constructively or destructively with the incident field and cause an overall change in the momentum flux through some closed surface surrounding the particle. In the presence of the highly focused beam of a laser our understanding of the particle's trapping behavior essentially returns to the electrodynamics discussion presented earlier in section 1.1.0.1.

1.3.4.3 Mie Scattering - The Full and Exact Solution

In both the case of geometric diffraction theory and dipole scattering the forces imparted to the particle will only hold if one remains in the length regime they were designed for. The impetus behind the development of any scattering approximation is to avoid doing the full Mie scattering calculation. The Mie scattering solutions to Maxwell's Equations for spherical and cylindrical particles are exact for all regimes, account for the boundary conditions at the dielectric interface and allow for interference between the incident and scattered fields. To correctly allow interference between the incident and scattered fields the incident wave is re-expressed in the vector wave harmonics basis set appropriate to the scattering body being studied, cylindrical or spherical.

With the advent of modern computers the Mie scattering calculation be-

came less intractable, but the intuitive ease with which one can envision the interaction of light with matter in geometric ray optics is lost in pursuit of exactness. It seems natural, therefore, to question how far outside of its prescribed regime our ray optics approach can safely take us. In chapter four of this dissertation we use the cylindrical vector harmonics to express both the electromagnetic fields incident upon and scattered from a dielectric particle with boundaries described by a pair of infinite concentric cylinders. We calculate the momentum flux through some surface for the interaction of a collimated incident plane wave with the dielectric boundaries described. The plane wave is described by time averaged total fields, incident plus scattered, and the double dot product of the Maxwell stress tensor with the direction of beam incidence used to calculate the total momentum flux.

As a first pass the momentum transfer to a homogenous two dimensional dielectric sphere cross section was calculated using the Mie fields and our numerical ray optics simulation. The ratio of these values was calculated for a sphere of size parameter ka ranging for $0.1 \leq ka \leq 100$, where $ka = \frac{2\pi a n_a}{\lambda}$. We find the geometric optics approach consistently overestimates the scattering force until ka approaches $\mathcal{O}(1)$. In this regime geometric optics underestimates the scattering force, supporting our earlier qualitative description of the diffraction effects in this regime. We note there is no gradient force in the model used here as the beam is collimated, but gradient forces due to diffraction should still be possible. For length scales $ka \geq \sim 50$ we find the numerical geometric optics result equal to those calculated using the Mie formulation.

With the scattering force understood for a homogeneous particle in the different size regimes we go on to explore the scattering force on non-homogeneous particles. Holding the outer bounds of the particle constant and slowly changing the radius of the inner dielectric boundary we are able to step seamlessly through multiple scattering regimes, calculating the total scattering force from

the Mie calculation at each step. The same approach was used in calculating the Mie and geometric optics scattering force, however both were then normalized by the incident momentum and directly compared.

Particles were modeled with ka consistently held at $ka \sim 100$ (which for the parameters used represents a particle approximately 16 microns in diameter) and an inner cavity of size parameter $kb = \frac{2\pi n_b b}{\lambda}$, where in this case the inner index of refraction was equal to that of the media surrounding the dielectric particle. The size parameter of the inner cavity was allowed to range from $0 \leq kb < 100$, with values of $kb < 48$ showing an underestimation of the scattering force on the part of the geometric optics simulation. As kb is increased from $48 \leq kb < 82$ the geometric optics calculation overestimates the total scattering force. For values of $kb > 82$, the geometric optics result once again underestimates the scattering force. In the small kb regime one finds some of the rays contained internally by the higher dielectric medium, which would either give rise to dipole scattering or diffract around the particle at grazing incidence in the full Mie calculation, instead are excluded from interaction in the geometric optics picture, the ray simply does not see the boundary. As the inner cavity size is increased more of the rays which bend inward towards the cavity, following their initial transmission into the high dielectric region, can now intersect the cavity. These rays could intersect the base at grazing incidence, imparting a gradient force from the geometric diffraction argument illustrated in figure 1.5b. In the numerical simulations these grazing rays are not allowed to interact with the inner cavity. Once kb reaches values above 82 the dielectric can essentially be described as a thin ring, failure to account for diffraction in this regime results in an underestimation of the scattering force.

CHAPTER 2

Simulation Methods

2.1 Introduction

As mentioned in chapter one, a closed form geometric ray optics solution for a solid spherical particle was derived by Ashkin in 1992. While there is a slight overestimation of the scattering force, geometric optics offers rapid and fairly accurate approximation of the forces acting on a symmetric particle in the presence of a focused beam, if the particle's smallest dimensions are within the ray optics regime. For more complex shapes, for example inhomogeneous shapes with cavities of a different dielectric constant or irregular geometries, a closed form solution is either impossible or intractable. We address these challenges with a numerical ray optics simulation which only requires the equations defining the boundaries of the shape, the indices of refraction and the numerical aperture of the beam allowing one to forgo most symmetry considerations and to calculate the momentum transfer to essentially any shape.

In the following sections the equations used to calculate the momentum transfer at each point of intersection are outlined and their methods of implementation are explained. The number of rays used for the beam decomposition and number of intersections allowed for each ray required to reach convergence are discussed, as well as the simulation parameters. Finally the simulation results for a two dimensional circle are compared to those found using Ashkin's closed form solution.

2.2 Methods

A single focused beam, averaged over polarizations and distributed across a two dimensional aperture, was used. A flat light distribution and a discrete point of focus were chosen as this allowed both direct comparison with results found using Ashkin's closed form solution and more rapid computation in running of the simulations. The focal point of the beam was selected to give a maximum angle of incidence, $\phi_i \approx 64^\circ$, mimicking the maximum angle of a 1.4 numerical aperture objective lens. The beam was decomposed into discrete rays, propagating through a homogeneous medium. The particle being modeled was described by a set of boundaries surrounding a region of higher dielectric constant.

In all simulations the beam was held stationary and the particle translated across an array of positions in discrete steps. The area sampled was selected such that positions were available which placed all of the particle bounds, in any orientation, at least one internal length unit away from the focal point of the beam. Fifty steps were used per internal length unit. For any shape the boundaries were defined from the point in the array at which the shape had been positioned. The specific equations used to describe the boundaries of the shape will be discussed in subsequent chapters. At each step the total force on the particle was calculated and these values were used to generate a force vector field. A static potential surface was calculated using the vector field and the curl of the field determined with a line integral about each point, using the average of two adjacent force vectors.

2.2.1 Calculating the momentum transfer to any shape

The beam is initially discretized into unit ray vectors, directed from the aperture to the focal point of the beam. All possible points of intersection for the

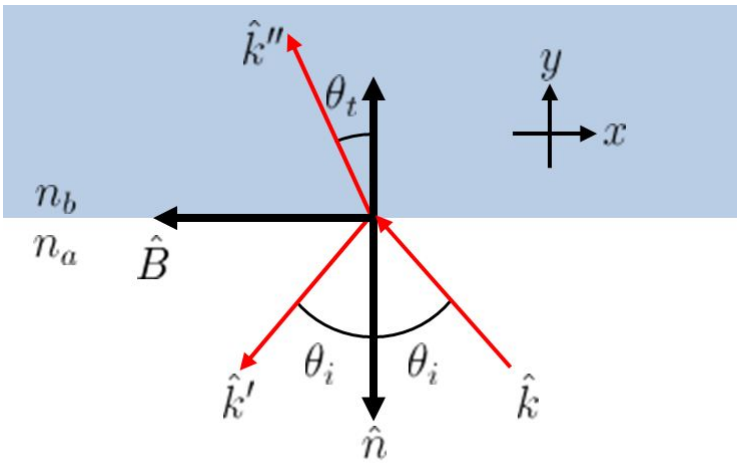

Figure 2.1: The incident $(\hat{k})$, reflected $(\hat{k}')$, transmitted $(\hat{k}'')$, unit normal $(\hat{n})$, and unit tangential $(\hat{B})$ vectors; as well as the angles of incidence and transmission and the indices of refraction.

ray with the boundaries of the shape are found and the closest point of intersection selected. At each intersection the unit normal, $\hat{n} = \frac{\vec{\nabla} r}{|\vec{\nabla} r|}$ for circular shapes and $\hat{n} = \frac{\vec{l}_{seg} \times \hat{z}}{|\vec{l}_{seg} \times \hat{z}|}$ for line segments, was calculated. The tangential vector, $\hat{B} = \hat{n} \times \hat{z}$ is used with the unit normal to calculate the direction of the reflected,

$$\hat{k}' = \hat{n}\left(\hat{k} \cdot \hat{n}\right) + \hat{B}\left(\hat{k} \cdot \hat{B}\right), \tag{2.1}$$

and transmitted,

$$\hat{k}'' = \frac{-\hat{n} + \tan\left(\theta_t\right)\hat{B}}{\sqrt{1 + \tan\left(\theta_t\right)}}, \tag{2.2}$$

rays. For ease of visualization all of these variables as are illustrated in figure 2.1.

$$\tan\left(\theta_t\right) = \frac{-\frac{n_r}{n_t}\sqrt{1 - \left(\hat{k} \cdot \hat{n}\right)^2}}{\hat{k} \cdot \hat{n}}. \tag{2.3}$$

The fraction of the incident momentum carried by the transmitted and reflected rays was calculated using Fresnel's equations. Each ray is injected

with unit initial momentum. Averaging over polarities the net momentum transfer to the particle, at each intersection, is calculated using conservation of momentum,

$$\vec{p}_{particle} = -\left[\hat{k} - \left(T\,\hat{k''} + R\,\hat{k'}\right)\right] \tag{2.4}$$

2.2.2 The total momentum transfer

With the previously described mechanism for determining the points of intersection, as well as the directions and magnitude for the incident, reflected and transmitted momentum vectors in place, the code is implemented as follows:

- A single ray is injected, labeled j_0^0, and the closest point of intersection is determined.
- The direction and magnitude of the reflected and transmitted momentum vectors are found.
  - If total internal reflection occurs no transmitted vector is calculated and the reflected ray is assigned all of the incident momentum.
- These values are utilized to calculate the momentum transfer to the particle.
- Using the indexing process illustrated in Figure 2.2
  - The reflected ray is assigned index j_0^1, with the direction, magnitude and origin resulting from the intersection of j_0^0 updated appropriately.
  - The transmitted ray is assigned index j_1^0, and the ray's direction and magnitude stored.

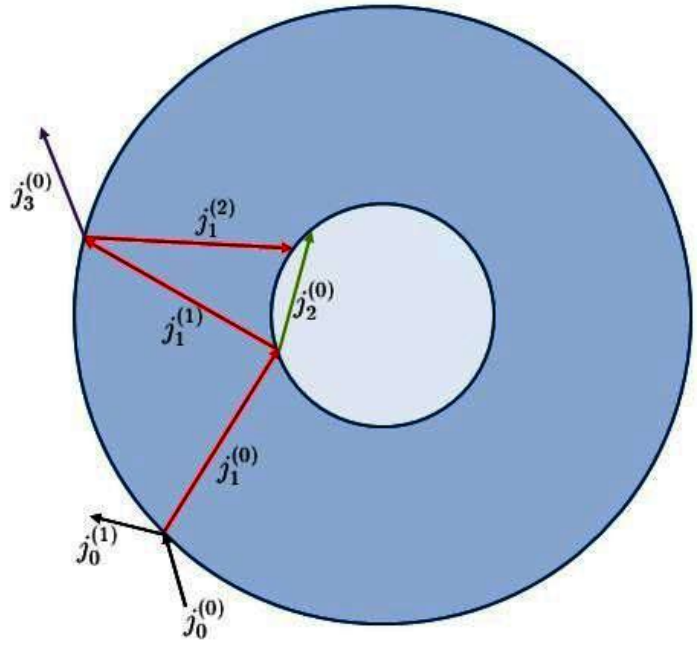

Figure 2.2: The indexing process for a single ray.

The ray, index j_l, is allowed to intersect each subsequent point in its path, with the above process repeated, until it either fails to intersect or a cutoff number of intersections are reached. The index of the ray is then incremented and the next ray, index j_{l+1}, followed.

2.3 Convergence

From the description of the code implementation above it would appear the numerical simulation would run for infinitely long time scales, as at each intersection two new rays are generated, leading to an exponential increase in the number of rays. Discretizing the beam into a reasonable number of incident rays would only serve to exacerbate the problem. Adding scattering interfaces to the particle geometry serves to further increase the number of rays the simulation must keep track of. A pair of concentric circles therefore serves as an

excellent test case to determine the minimum number of rays with which to decompose the beam and the minimum number of intersections to allow each constituent ray for convergence to be reached.

A concentric circle geometry was used, with the outer radius held constant and the inner radius varied. The particle was consistently placed at the same position and all of the rays making up the beam injected. Each ray over the entire index was allowed to intersect the particle ten times and the net momentum transferred to the particle as a function of the number of rays initially injected was calculated. The difference in efficiency $\Delta Q = Q_{n+1} - Q_n$, defined as transferred momentum normalized by the total incident momentum, was calculated for 10^n rays. As is shown in figure 2.3a, ΔQ reaches $\mathcal{O}(10^{-5})$ following the injection of 10^5 rays. For the $\frac{r_{inner}}{r_{outer}} = 0.1$ case approximately 16% of the rays experienced total internal reflection off the inner boundary of the shape, leading to more slowly converging values of Q. To determine the minimum number of intersections each ray segment must be allowed, the process was repeated; this time holding the number of rays injected at a constant value of 10^4 and increasing the number of allowed intersections. Figure 2.3b illustrates differences $\Delta Q < 10^{-3}$, which for a 10 mW beam is ± 0.04 pN of force, within 6 intersections for all geometries tested.

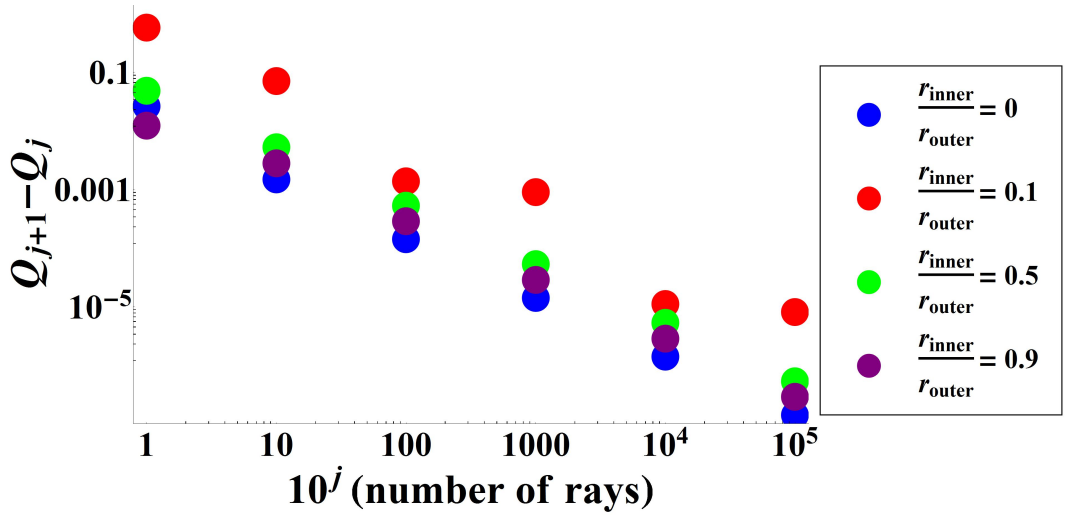

(a)

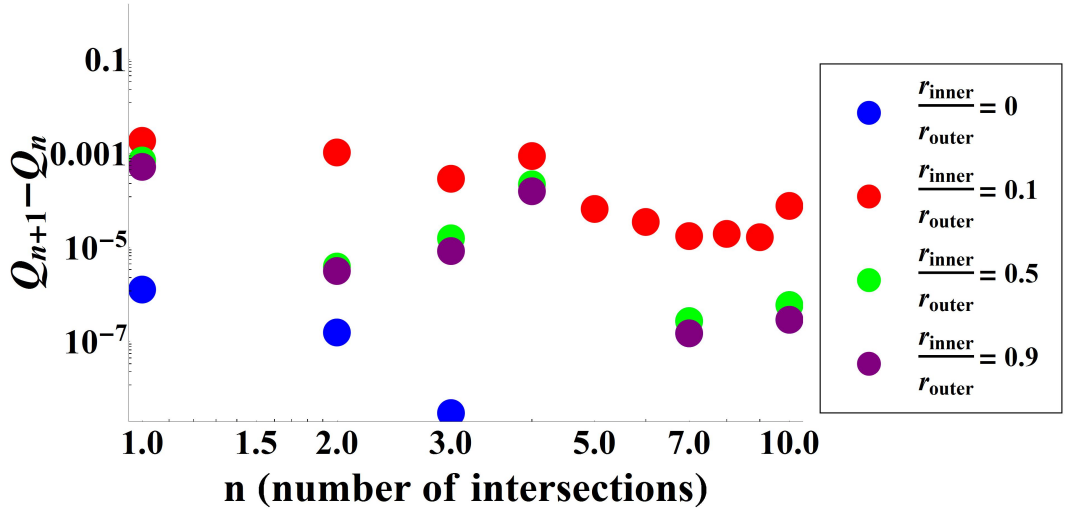

(b)

Figure 2.3: (a) The change in efficiency ($Q = \frac{p_{mag}}{p_{incident}}$) as a function of the number of incident rays and (b) as a function of the number of allowed intersections for each ray. For $\frac{r_{inner}}{r_{outer}} = 0.1$, approximately 16% of the incident rays undergo total internal reflection with the inner wall of the shape, accounting for the slower convergence.

2.4 Comparison with the closed form solution

The numerical ray optics simulation gives an approximation of the exact forces imparted to the particle by a focused beam. Future chapters will compare the scattering forces calculated using the numerical simulation to those found analytically using Maxwell's equations. As a first pass in testing the accuracy, one can reasonably demand that the numeric method be in close agreement with the analytic closed form solution for a solid homogeneous particle. To verify that this was the case, we directly compared the efficiency for a single ray, as a function of angle of incidence, and for the complete beam; calculated using both methods. As is shown in figure 2.4 we find exact agreement with Ashkin's solution for a single ray.

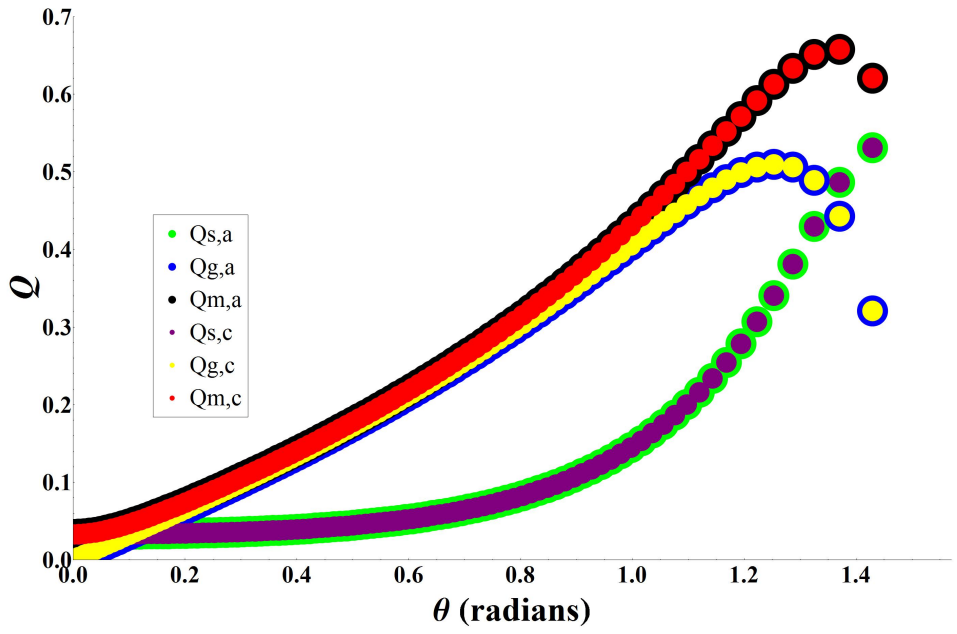

Figure 2.4: Scattering, gradient and total efficiency (Qs, Qg and Qt) for a single ray as a function of angle of incidence. Subscript *a* denotes efficiency from the closed form analytic solution, subscript *c* denotes efficiency found using the numerical simulation.

This process was repeated, this time integrating along the beam aperture,

using both methods. The particle was translated along the beam axis and the total efficiency analytic efficiencies calculated using the code generated angle of incidence. The numeric efficiency is simply the normalized force in the direction of beam incidence. All of these values were calculated as a function of displacement from the focal point of the beam, S, with $S < 0$ corresponding to the circles center placed below the focal point of the beam and $S > 0$ for positions above the focal point, as is illustrated in figure 2.5.

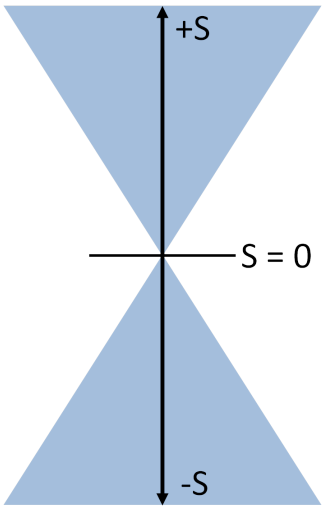

Figure 2.5: S, or displacement from the focal point of the beam. $S < 0$ corresponds to positions below the focal point of the beam, $S > 0$ corresponds to positions above the focal point of the beam. The beam propagates in the positive S direction.

The values for Q_s, Q_g and Q_{tot} calculated analytically, as well as the value of Q_{tot} found using the numerical geometric optics simulation, are shown in figure 2.6.

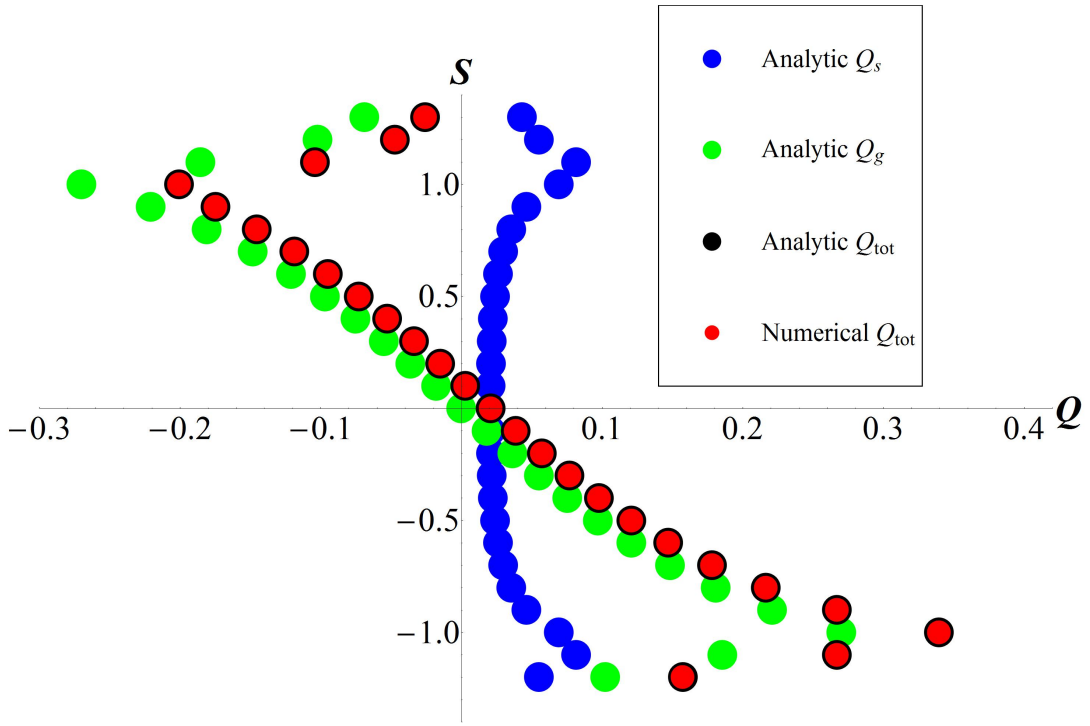

Figure 2.6: Scattering (Q_s), gradient (Q_g) and total efficiency ($Q_{tot} = Q_s + Q_g$), as a function of displacement from the beam focus, S, for the Ashkin solution (analytic) and the ray optics code (numeric).

We find almost exact agreement between the analytic and numerical solutions, with the relative error

$$\frac{Q_{tot,numerical} - Q_{tot,analytic}}{Q_{tot,analytic}}, \tag{2.5}$$

never reaching values above 0.1%, as is illustrated in figure 2.7.

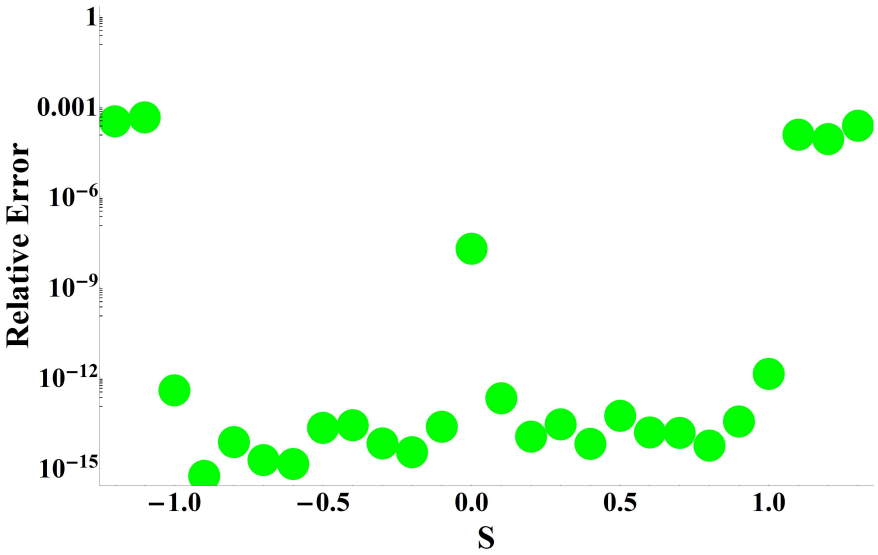

Figure 2.7: The relative error in the total efficiency calculated using the numerical simulation.

CHAPTER 3

Trapping Behavior of Symmetric Shapes

3.1 Introduction

The symmetric spherical dielectric particle remains an archetypical geometry in optical trapping applications. Spherical dielectric particles have been used as probes for the application of forces to DNA[4,62,63] or the deformation of red blood cells,[6] in measurement of the forces applied by single kinesin molecules,[5] to examine the forces imparted by novel beams; including holographic optical tweezer arrays,[10,11] multi-ringed beams[64] and in the simultaneous trapping of high and low index particles using optical vortices.[17]

Recently Ramsay and co-workers reported on the trapping of a hollow, cylindrical microsyringe.[65] Using a three beam trap they were able to both hold a borosilicate microcapillary (1 to 10 μm in diameter and 5 to 150 μm in length) stationary, long axis perpendicular to the direction of beam incidence, while translating a microsphere through the microcapillary. Modeling this system using physical optics, accounting for the boundary conditions and solving Maxwell's equations for both trapping particles, would be intractable. A basis set which allowed the description of cylindrical, spherical and planar wave vectors would have to be employed, allowing interference between the incident and scattered fields. With a cylinder wall thickness of 2 to 4 μm and a trapping wavelength of 1.06 μm, the primary dimension of the microsyringe involved in trapping is not even twice the incident wavelength and therefore

well outside the accepted length scales for geometric optics. The overall geometry of the system, however, makes our rather straightforward numerical approach very attractive. The natural question is how inappropriate is it to use a geometric optics approximation for particles on length scales near the wavelength of the incident light?

In previous chapters we discussed our numerical approach to calculating the total forces on a dielectric particle in the geometric optics regime. Having established near exact agreement between the results of the numerical approach and the analytic solution for a solid homogeneous particle we now investigate the trapping behavior for a rotationally symmetric shape with increased scattering interfaces, in other words the cross section of a hollow cylinder. In the following sections we will examine the force vector fields for a 1 μm outer diameter cylinder cross section, with a hollow cavity of steadily increasing inner diameter. The scalar potential surface as well as the ratio of the curl to the potential shall be given for each case. In chapter 4 we will determine the level of agreement in the scattering force found using the exact physical optics solution and that found using our numerical optics simulation.

3.2 Background

The physical phenomena of optical trapping results from a balance of the scattering and gradient forces. The gradient force, as discussed in chapter 1, is driven by the reduction of the system's potential energy as the dielectric material moves to the region of highest field gradient. The scattering force is the consequence of radiation pressure, resulting from reflection of the light off of the dielectric interface. If these forces can be balanced in the beam stable trapping results.

3.2.1 Choosing points of intersection for symmetric shapes

The symmetric shape studied consisted of two concentric cylinders with radii R_1 and R_2 where $R_1 > R_2$. As discussed in chapter two, the beam is decomposed into discrete rays. The closest point of intersection, if any, for each ray is determined as follows; for a ray originating at point $(x_\circ, y_\circ)$ to intersect either circle, centered at (a, b), with $\overline{x} = x_\circ - a$ and $\overline{y} = y_\circ - b$,

$$(R_{1,2})^2 = \left(\overline{x} + q_{1,2}\hat{k}_x\right)^2 + \left(\overline{y} + q_{1,2}\hat{k}_y\right)^2. \tag{3.1}$$

Solving for q,

$$\pm q_{1,2} = -\gamma \pm \sqrt{\gamma^2 - R_{1,2}^2 - \left(\overline{x}^2 + \overline{y}^2\right)}, \tag{3.2}$$

with $\gamma = \overline{y}\hat{k}_y + \overline{x}\hat{k}_x$, the smallest positive root, $\pm q_1$ or $\pm q_2$ is chosen.

3.2.2 Stable trapping, the scalar potential

The stable trapping point is found by scanning through the complete force vector array and selecting any or all of the points within the array at which all of the surrounding force vectors are directed inward, towards that point. Of the points found which meet this condition the point with the lowest total force magnitude is assigned as the stable trapping point. Once the stable trapping point is found the effective potential of the trapping force is calculated using the work required to move outward from the stable trapping point.

Using Green's theorem,

$$\oint \mathbf{F} \cdot d\mathbf{s} = \int\int (\nabla \times \mathbf{F}) \cdot d\mathbf{a}, \tag{3.3}$$

to verify the force field is conservative, the net work for a closed path surrounding each point in the vector array was calculated. It is only in the case that this value is small that the calculated potential energy surface is meaningful. Generally we find that near stable trapping points there is a well defined

potential energy well but significant values for the net work, $\oint \mathbf{F} \cdot d\mathbf{s} > 0$, further away. The presence of nonconservative forces away from the stable trapping point is not surprising given the nonconservative nature of the scattering force.

The optical forces scale linearly with the power of the incident beam and are thus of no consequence for the analysis of the effect of particle geometry on trapping. Nevertheless is is of some interest to compare the depths of local trapping potential wells to thermal energy $\left(k_B T \approx \frac{1}{40}\, eV\right)$ in order to assess whether the calculated wells could, in fact, trap micron-scale particles at room temperature. Consequently, hereafter we assume the trapping beam has a power of 10 mW (typical for laser trapping experiments). Similarly we take the maximum angle of incidence to be 70°, modeling a high numerical aperture lens (for example a N.A. 1.25 water immersion microscope objective), as is typically used in optical trapping experiments.

The shape is modeled as two concentric circles marking the bounds of a homogeneous dielectric with index of refraction $n_b = 1.6$. This particular value was chosen as it approximates that of polystyrene (n = 1.617 - 1.572 for λ = 400 - 1010 nm at 20°C)[66] which is commonly used in optical trapping experiments. The surrounding media was assigned a refractive index of $n_a = 1.33$, to approximate the values found for water (n = 1.343-1.33 for λ = 400 to 1010 nm at 20°C).[67] These parameters can easily be changed and a different maximum angle of incidence or dielectric mismatch will change the trapping behavior of the shape being modeled. An outer radius of 1 μm was chosen an the inner radius varied from $0\,\mu m \leq R_{inner} \leq 0.9\,\mu m$. A unit outer radius was selected as, for geometric optics, particle size does not enter into the force calculations. Additionally selecting this size allowed a shorter focal length and therefore a smaller beam aperture, leading to a larger number of rays per unit length of the aperture.

3.3 Results

If we consider a homogeneous sphere interacting with a focused beam and position the center of the particle along the central beam axis, all forces perpendicular to the direction of beam incidence will cancel. With this simplified system we need only consider the forces parallel to the direction of beam propagation. For this example the scattering force will be in the direction of beam propagation and the gradient force can either be in the direction of beam propagation or against it, pushing the particle towards the focal point of the beam. At the point along the central beam axis at which the gradient force balances the scattering force stable trapping will occur. As, for particle positions below the focal point of the beam, the scattering and gradient forces have the same sign, in this particular example force balance is only possible if the center of the particle is positioned at or above the focal point.

With this understanding one would expect that if we were to remove dielectric material from the center of the sphere it would serve to reduce the gradient force, as there is less dielectric to interact with the high electric field gradient of the beam focus; and increase the scattering force, as the number of scattering interfaces has doubled. The stable trapping point should then be shifted away from the focal point of the beam. This is in fact the case for all inner cavity sizes. A single stable trapping point can be followed along the direction of beam incidence, moving away from the beams focal point as the inner cavity diameter is increased. Additionally the introduction of a cavity introduces new trapping points, off-axis from the beam, as will be shown.

For all shape geometries the force field, units pN, the scalar potential and the net work for a closed path surrounding each point in the force array, units $k_B T$ at $25^{\circ}C$, were calculated. Each plot of the scalar potential and the net work includes a white circle, denoting the stable trapping point, determined

as mentioned previously. The potential at the stable trapping point was set as the zero of the potential surface.

3.3.1 Solid dielectric circle, $R_{inner} = 0$

For $R_{inner} = 0$, the trapping behavior matches that of Ashkin's analytic calculations. Examination of the force field, figure 3.1a, shows stable trapping along the beam axis and slightly above the focal point of the beam, at $S = 0.12$; where $S = b - foc$ and b corresponds to the y-coordinate of the particle's center. The scalar potential, figure 3.1b, reinforces the stable trapping point found in the force field, with an overall well depth of $\approx 700\,k_BT$. Examining a close-up of the same potential surface, figure 3.1c shows a well, $\approx 1.2\,\mu m$ in diameter, with a depth of $560\,k_BT$. As is illustrated in figure 3.1d, the net work, normalized by the potential at each point, displays values below $0.05\,k_BT$ within the region of the potential well.

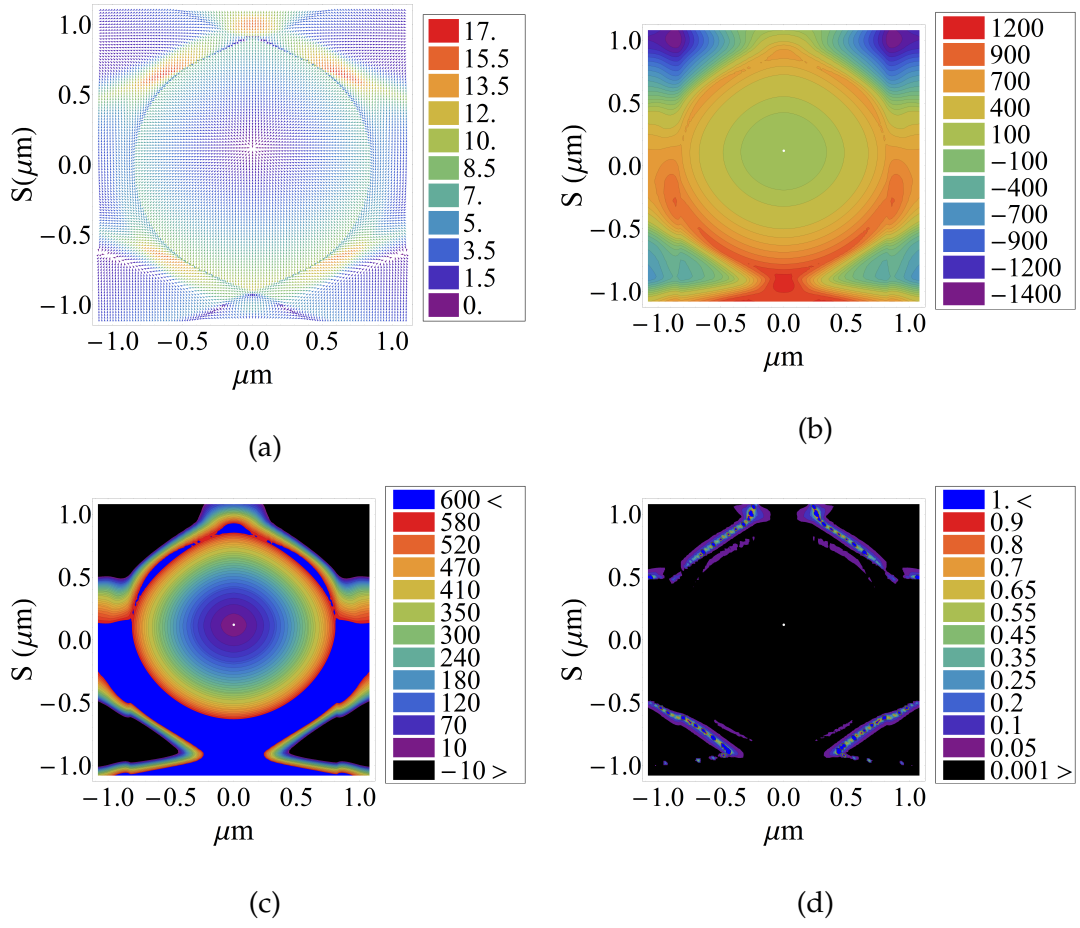

Figure 3.1: (a) The force field for a solid circle, $R_{inner} = 0$. A stable trapping point is illustrated along the beam axis, at $S = 0.12$. (b) The scalar potential calculated from the full force field, and (c) a close-up of the potential. (d) The absolute value of the net work normalized by the potential, $\left|\frac{W_{net}(x,y)}{U(x,y)}\right|$.

3.3.2 Dielectric circle with a cavity

The addition of a small cavity shifts the axial trapping position, found for the $R_{inner} = 0$ case, away from the focal point and along the direction of beam incidence. Additionally off-axis trapping points appear. For all trapping points near the focal point of the beam the net work shows a marked increase in the non-conservative scattering force for shifts in the particle position perpendic-

ular to the beam axis.

3.3.2.1 $R_{inner} = 0.1$

The addition of even a small cavity shifts the axial trapping point in the direction of beam incidence, by 0.2 μm from $S = 0.12\,\mu m$ in the $R_{inner} = 0$ case to $S = 0.32\,\mu m$, figure 3.2a. In the region surrounding the focal point of the beam, coordinates $(0\,\mu m, 0\,\mu m)$, we see the particle is actually pushed away from the focal point with the addition of a small cavity. As will be shown in the force field plots to follow, the size of this region of repulsion, surrounding the focal point, scales directly with the size of the cavity radius. The depth of the potential well is also greatly decreased. Where a well depth of $560\,k_BT$ was found for the case of the solid circle, $R_{inner} = 0$ we find a local potential, well depth $31\,k_BT$, with the addition of a cavity with a $0.1\,\mu m$ radius.

Off-axis two new trapping points appear, below the focal point of the beam at $(\pm 0.7\,\mu m, -0.8\mu m)$ and a metastable trapping point parallel to the focal point, with local minima at $(\pm 0.3\,\mu m, 0\mu m)$ and $(\pm\,0.5\,\mu m\,, 0.2\,\mu m)$, figure 3.2a. The potential minimum below the focal point of the beam has a well depth of $\approx 250\,k_BT$. In the region of metastable trapping the upper potential minimum has a well depth of approximately $35\,k_BT$, while the lower has a depth of approximately $90\,k_BT$. Near the focal point of the beam the net work, figure 3.2d, is highly affected by the scattering force. We see much higher values for the net work, compared to the potential at each point, as the particle is moved perpendicular to the beam axis. The local minimum below the focal point of the beam displays very small values for the net work, compared to the potential in this region, with values below 1%.

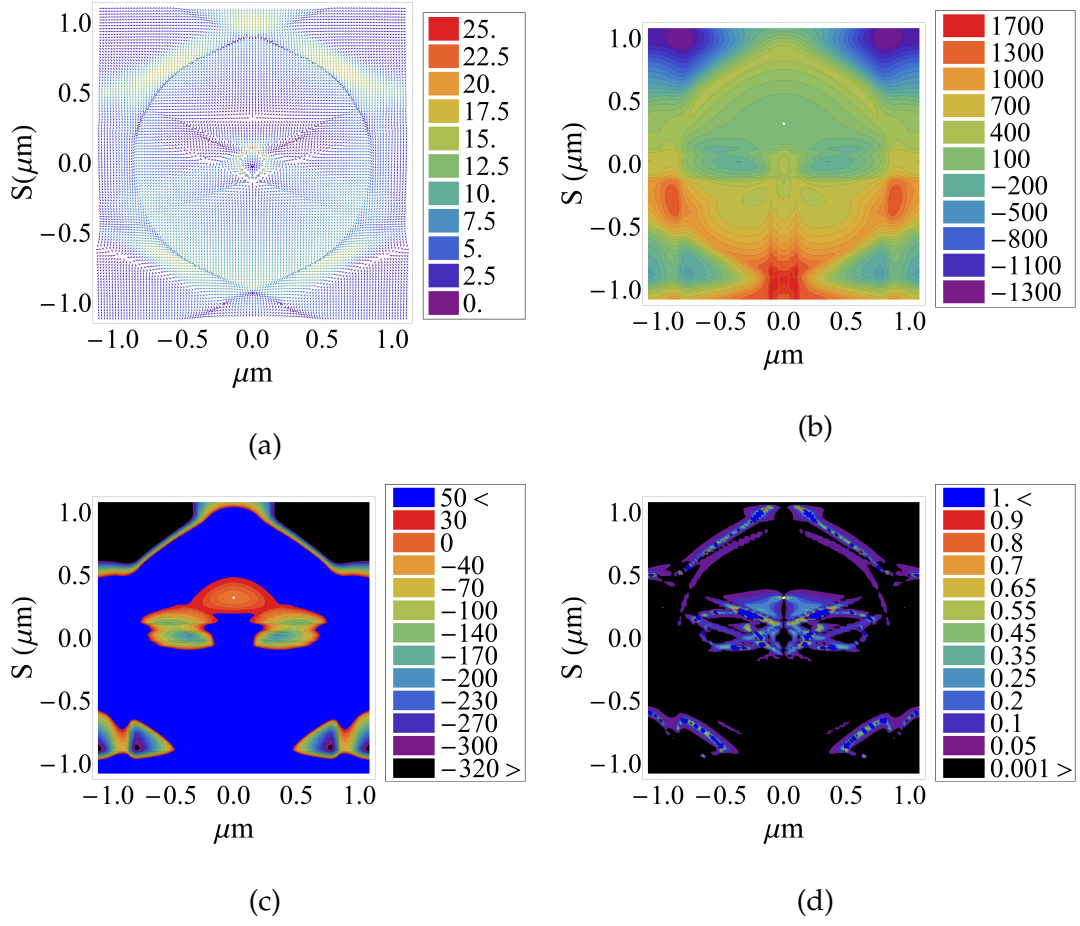

Figure 3.2: (a) The force field for a particle with an inner cavity $R_{inner} = 0.1$. A stable trapping point is illustrated along the beam axis, at $S = 0.32$. (b) The scalar potential calculated from the full force field, and (c) a close-up of the potential, local minima are displayed at positions $(\pm 0.7\,\mu m, -0.8\mu m)$, $(\pm 0.3\,\mu m, 0\mu m)$, $(\pm 0.5\,\mu m, 0.2\,\mu m)$ and $(0\,\mu m, 0.32\,\mu m)$, with potential well depths of $\approx 250\,k_BT$, $\approx 90\,k_BT$, $\approx 35\,k_BT$ and $\approx 31\,k_BT$ respectively. (d) The absolute value of the net work normalized by the potential, $\left|\frac{W_{net}(x,y)}{U(x,y)}\right|$.

3.3.2.2 $R_{inner} = 0.2$

Increasing the cavity size serves to further shift the axial stable trapping point away from the focal point of the beam, $S = 0.46\,\mu m$, and create more clearly

defined off-axis trapping points, figure 3.3a. The well depth at the on-axis trapping point increases by $27\,k_BT$ to $58\,k_BT$. Off-axis all of the local potential minima increase in well depth. The trapping point at $(\pm 0.7\,\mu m,\, -0.8\,\mu m)$ has a well depth of approximately $485\,k_BT$. The upper and lower metastable points display well depths of $125\,k_BT$ and $420\,k_BT$ respectively, figure 3.3c. The normalized net work reaches values as high as 100% within the metastable trapping region, but does not rise above 10% within the region defining the base of the potential well. For the trapping point below the focal point of the beam the normalized net work is less than 0.1% near the base of the potential well.

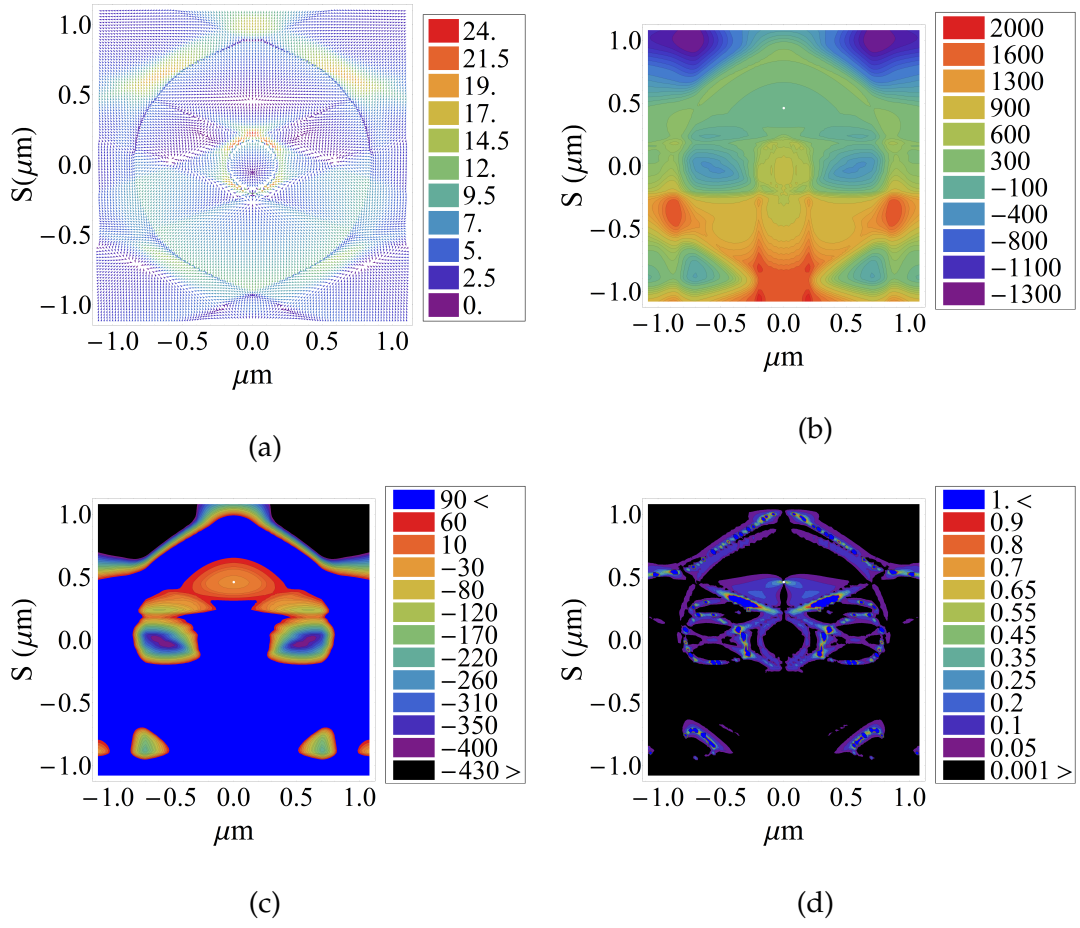

Figure 3.3: (a) The force field for a 1 μm radius circle with a small cavity, $R_{inner} = 0.2$. A stable trapping point is illustrated along the beam axis, at $S = 0.46$. (b) The scalar potential calculated from the full force field, and (c) a close-up of the potential, local minima are displayed at positions $(\pm 0.7\,\mu m, -0.8\mu m)$, $(\pm 0.3\,\mu m, 0\mu m)$, $(\pm\, 0.5\,\mu m\,, 0.2\,\mu m)$ and $(0\,\mu m, 0.32\,\mu m)$, with potential well depths of $\approx 485\,k_BT$, $\approx 420\,k_BT$, $\approx 125\,k_BT$ and $\approx 27\,k_BT$ respectively. (d) The absolute value of the net work normalized by the potential, $\left|\frac{W_{net}(x,y)}{U(x,y)}\right|$.

3.3.2.3 $R_{inner} = 0.3$

Taking the increase in the cavity size one step further, $R_{inner} = 0.3$ we see a loss of definition in the off-axial trapping points, figure 3.4a, and a more clearly

defined on-axis trapping point at $S = 0.58\,\mu m$. The on-axis potential well deepens as a result, reaching a depth of $90\,k_BT$. Off-axis we see well depths of $180\,k_BT$, $625\,k_BT$ and $725\,k_BT$ for the trapping points at $(\pm 0.6\,\mu m,\ 0.38\,\mu m)$, $(\pm 0.65\,\mu m,\ -0.1$ and $(\pm 0.65\,\mu m,\ -0.88\,\mu m)$ respectively. We once again see high sensitivity to the scattering force for the axial trapping point, in examination of the net work, figure 3.4d. The off-axis local potential minimums all exist in regions with relatively low net work, $\leq 0.1\%$.

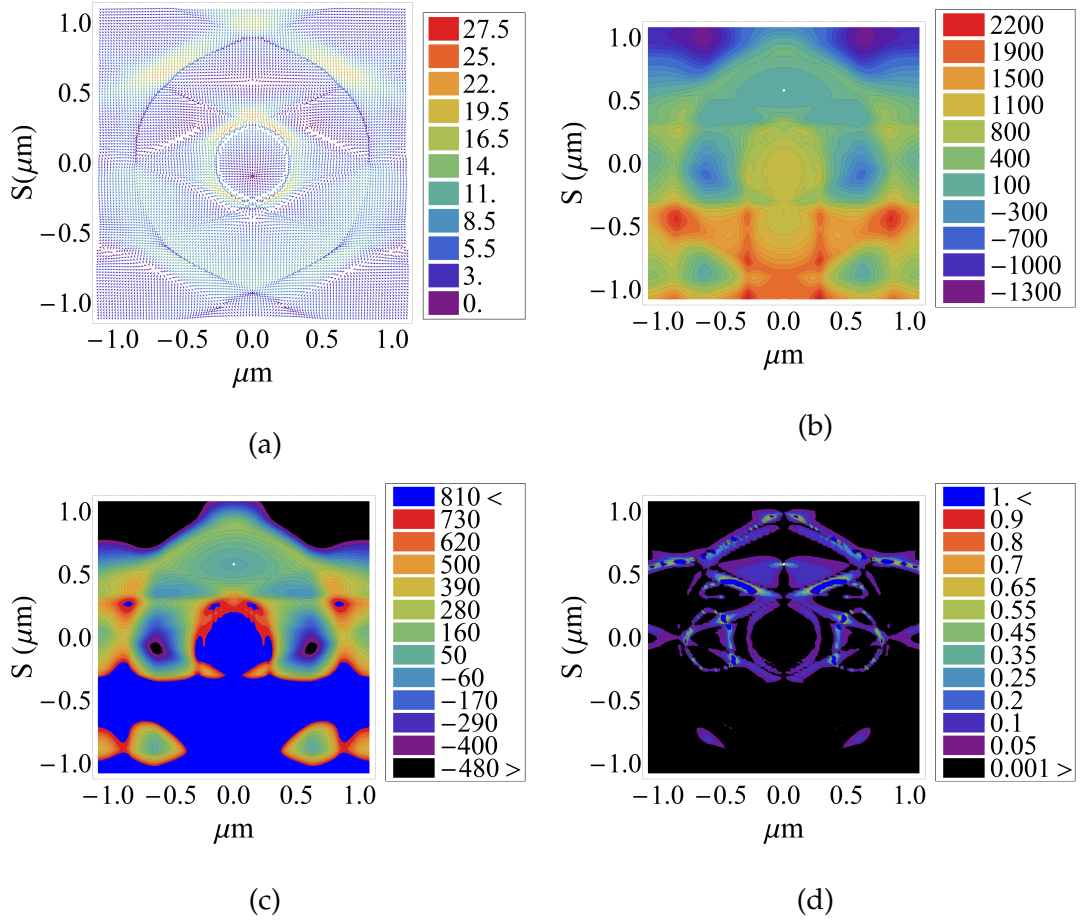

Figure 3.4: (a) The force field for a solid circle, $R_{inner} = 0.3$. A stable trapping point is illustrated along the beam axis, at $S = 0.58$. (b) The scalar potential calculated from the full force field, and (c) a close-up of the potential. (d) The absolute value of the net work normalized by the potential, $\left|\frac{W_{net}(x,y)}{U(x,y)}\right|$.

This trend in the on-axis trapping point shifting up the beam axis in the direction of propagation continues, until finally for $R_{inner} > 0.5\,\mu m$ all on-axis trapping is lost. As was mentioned previously the region surrounding the focal point shows forces pushing the particle away from the focal point of the beam. The size of this region grows with each incremental step in the radius of the inner particle cavity. Figure 3.5 illustrates the force fields for all inner cavity sizes greater than $0.3\,\mu m$ which were examined.

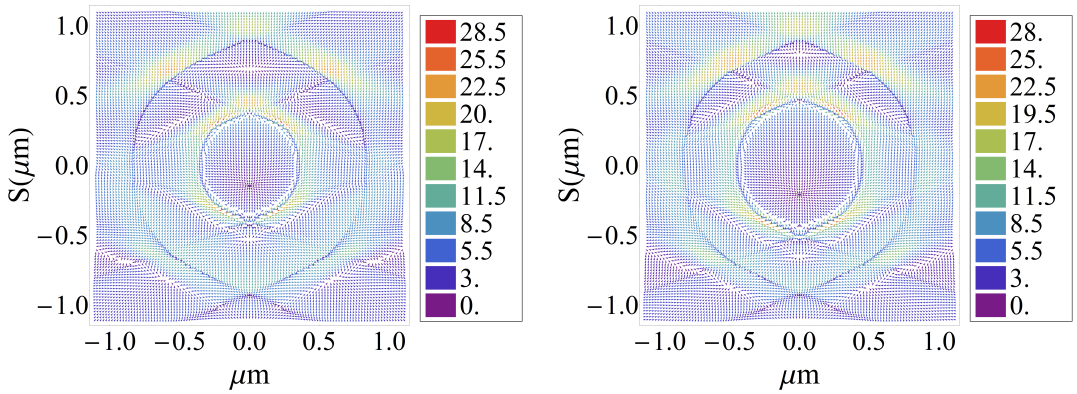

(a) $R_{inner} = 0.4$

(b) $R_{inner} = 0.5$

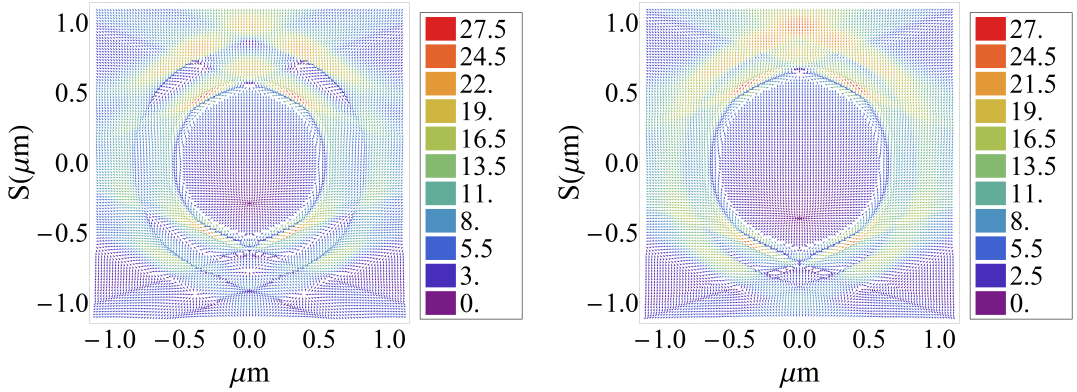

(c) $R_{inner} = 0.6$

(d) $R_{inner} = 0.7$

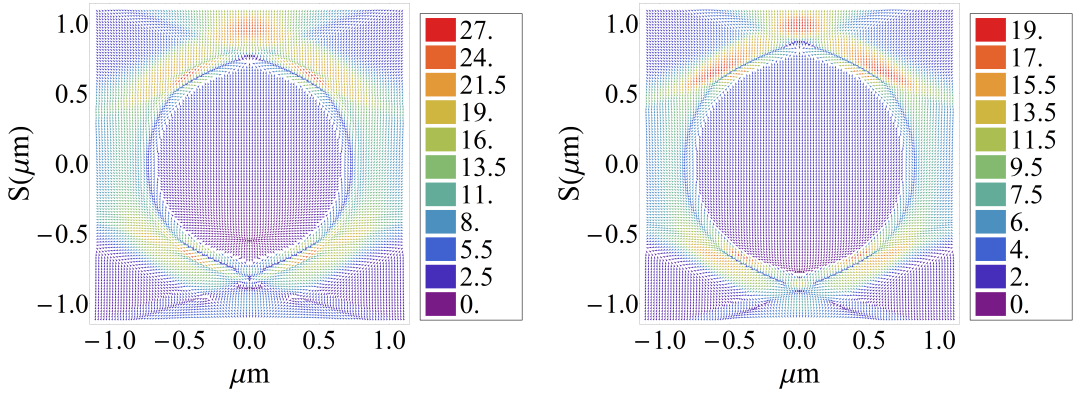

(e) $R_{inner} = 0.8$

(f) $R_{inner} = 0.9$

Figure 3.5: The force fields for $0.4\,\mu m \leq R_{inner} \leq 0.9\,\mu m$

CHAPTER 4

Geometric Optics vs Mie Scattering

4.1 Introduction

As was discussed in previous chapters, geometric optics is an efficient and intuitive means to calculate the momentum transfer from a beam to an arbitrary particle. Our previous discussion examined the geometric optics result for the forces acting upon a two dimensional hollow dielectric particle as a function of inner cavity radius. This investigation was performed with full understanding that overestimation of the scattering force is inherent in the geometric optics picture if the particle size is on the order of, or less than, the wavelength of the incident light.

When the size of particle, the internal cavity or any other length characteristic of the particle structure is reduced to the scale of the incident radiation wavelength one must expect the results of geometric optics to become inaccurate. For example the magnitude of the radiation pressure on a scatterer smaller than the wavelength of incident radiation should be less than that predicted by geometric optics, due to diffraction of the radiation back into the forward scattering direction.

From Babinet's principle these effects must apply to a hole in a dielectric medium as well and are thus applicable to the experiments of Wilking and collaborators.[9] Their data in particular exhibits the initially surprising phenomenon of reentrant trapping. In a series of experiments on the trapping of

rings, in which the outer radius was held constant while the inner radius was steadily increased, they find that as the inner cavity is initially increased the scattering force was increased and the trapping force reduced. At a critical void size, the particle became impossible to trap. However, as the size of the cavity was further increased trapping once again became possible. We were not able to directly reproduce this reentrant trapping in our geometric optics simulation. We believe the reasons for this are two-fold. First the seemingly small differences in the shape geometry, for example using a circle rather than a square with rounded edges, appear to play a large role in the trapping behavior of the shape. This will be discussed in detail in the next chapter, where we examine the trapping behavior of a planar L shape. Secondly the geometric optics calculation fails to account for diffraction. In Wilking and collaborators' experiment a 633 nm wavelength was used and reentrant trapping was found for a ring with a thickness of approximately 1050 nm, or 1.66 times the wavelength of incident light.

More generally we expect that accounting for diffraction effects in laser trapping becomes increasingly important as the structure of a several micron scale particle become more complex, with features in the sub-micron range.

In this regime multiple approximations are available, including the discrete dipole approximation,[68] which has no dependence on particle geometry or size, or when the scattering center is sufficiently small compared to the wavelength of the incident light it is permissible to treat the scatterer as a point dipole, resulting in the Rayleigh scattering approximation. This yields an analytically tractable solution for the scattered radiation field and thus the momentum transfer per unit time from the incident beam to the object.

Alternatively, if the scatterer is too large to be treated as a point dipole, there are numerous approaches based on the original calculation by Mie, wherein the system is solved exactly; using the scattered, incident and com-

bined electromagnetic fields. As the actual description of the fields depends upon both the particle and beam geometry numerous theories and methods have been developed. These theories include Lorenz-Mie Theory, and Generalized Lorenz-Mie Theory. Lorenz-Mie Theory describes the fields for a spherical particle in the presence of a plane wave. Generalized Lorenz-Mie Theory describes the electromagnetic scattering of an arbitrary light beam by a spherical particle[69] and has been extended to describe the scattering of infinite cylinders.[27] Many of these calculations were initially performed to study the distribution of scattered radiation intensity as a function of angle and therefore did not consider the momentum transfer to the object. Such considerations are fairly straightforward as the Maxwell stress tensor can be directly calculated from the known radiation fields.

The Lorenz-Mie theory and all of its derivative theories require the computationally demanding calculation of scattering coefficients and in the case of the Generalized Lorentz-Mie theory the beam shape coefficients. Our numerical geometric optics implementation is, in contrast, straightforward to implement and not very computationally demanding. As was stated previously, geometric optics overestimates the scattering force imparted by each ray, the question is how large is this overestimation? Specifically how large is the overestimation of the scattering force in the geometric optics approximation for particles with feature sizes on the order of the wavelength of incident light? In the following sections we derive the scattering coefficients for a pair of concentric infinite cylinders. The coefficients are then used to describe the total field, incident plus scattered, which is used with the Maxwell Stress tensor to calculate the net momentum flux. The total momentum transfer using the exact solution for the cross section of a pair of infinite concentric cylinders is compared to that found using the numerical geometric optics simulation for a variety of inner cavity radii.

4.2 Background

4.2.1 Mie scattering - the exact solution

We begin, as always, with Maxwell's equations. For Maxwell's equations (SI units) in an infinite medium, absent of sources

$$\begin{aligned} \nabla \cdot \mathbf{B} &= 0, & \nabla \times \mathbf{E} + \frac{\partial \mathbf{B}}{\partial t} &= 0 \\ \nabla \cdot \mathbf{D} &= 0, & \nabla \times \mathbf{H} - \frac{\partial \mathbf{D}}{\partial t} &= 0. \end{aligned} \tag{4.1}$$

For a plane wave with harmonic time dependence, $e^{-i\omega t}$ the $\partial \mathbf{B}/\partial t$ and $\partial \mathbf{D}/\partial t$ terms simply become $-i\omega B$ and $-i\omega D$, respectively. For uniform isotropic dielectric medium, where ϵ is the permittivity of the medium, $\mathbf{D} = \epsilon \mathbf{E}$ these equations reduce to

$$\nabla \times \mathbf{E} = i\omega\mu\mathbf{H}, \qquad \nabla \times \mathbf{H} = -i\omega\epsilon\mathbf{E} \tag{4.2}$$

Combining the equations in 4.1 and 4.2 we find that both the electric and magnetic fields satisfy the Helmholtz wave equation

$$\nabla^2\mathbf{E} + \omega^2\epsilon\mu\mathbf{E} = 0 \qquad \nabla^2\mathbf{H} + \omega^2\epsilon\mu\mathbf{H} = 0 \tag{4.3}$$

In order to test our contention that the geometric optics based calculations over estimate the scattering force, we will complete the full scattering problem for a plane wave impinging on a dielectric cylinder with a concentric cylinder cavity. From this solution we will determine the momentum transfer to the cylinder from the appropriate integrals of the Maxwell stress tensor.

As is well known from scattering from a spherically symmetric potential in non-relativistic quantum mechanics, it is useful to exploit the symmetry of the scatterer by decomposing the incident plane waves into spherical ones, see e.g. Sakurai.[70] Here a cylindrical wave expansion is called for. We note however

that the incident radiation fields satisfying the wave equations in equation 4.3 are vector fields, unlike the scalar quantum wave functions. A more complicated expansion of the incoming plane waves into vector cylindrical harmonics is therefore required. This vector cylindrical harmonic description of both the incident and scattered fields necessitates a new basis set which must satisfy all of Maxwell's equations. As this is not commonly considered we briefly review this expansion here.

To begin we define a vector function $\mathbf{M}$ using a scalar function, ψ and a pilot vector $\mathbf{c}$

$$\mathbf{M} = \nabla \times (\mathbf{c}\psi) \tag{4.4}$$

To completely describe the system a second vector is necessary, perpendicular to both $\mathbf{M}$ and the pilot vector, while simultaneously satisfying Maxwell's equations,

$$\frac{\nabla \times \mathbf{M}}{k} = \mathbf{N} \tag{4.5}$$

The pilot vector, $\mathbf{c}$, and the scalar wave equation can be chosen on the basis of the scattering geometry of the particle of interest. The complete derivation of solutions to the wave equation, in either spherical or cylindrical coordinates, as well as the resulting vector wave equations are available from multiple sources; including Bohren and Huffman,[58] J. D. Jackson[61] and H.C. Van de Hulst.[38]

4.2.1.1 Cylindrical Vector Expansion

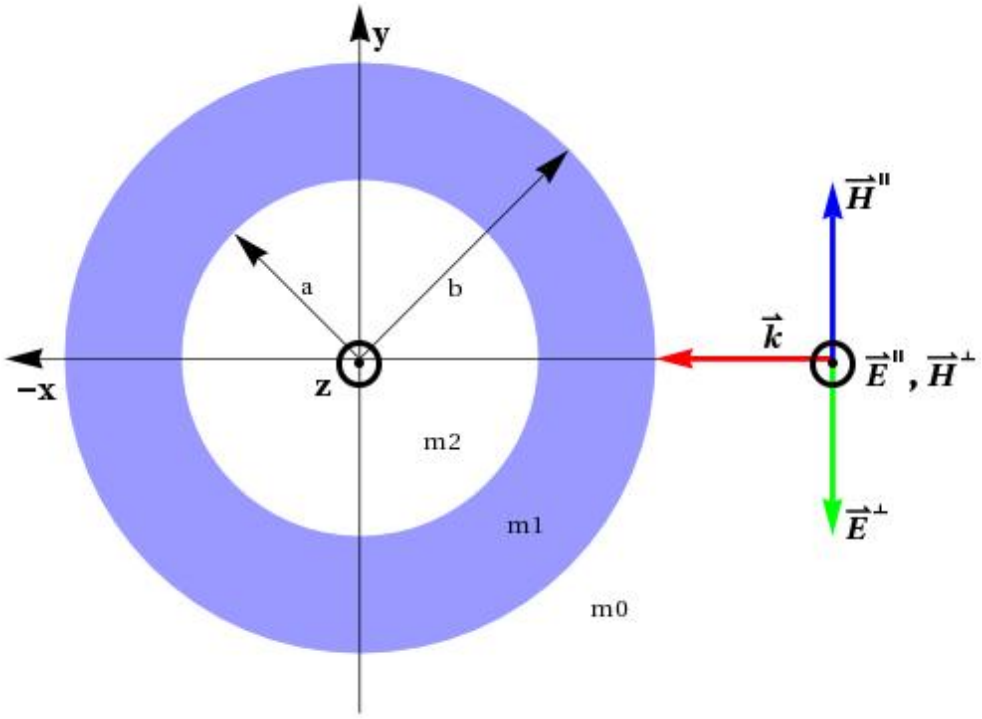

Figure 4.1: Cross-sectional view of the cylinder.

To calculate the momentum transfer from a plane wave to a cylindrical object one must first expand the incident field into cylindrical wave vectors. The cylinder is defined in Figure 4.1. As shown there, the outer radius is defined as $r_{outer} = b$ and the inner radius $r_{inner} = a$. The cylinder is composed of a uniform dielectric of refractive index m_1, which differs from that of the surrounding medium, $m_0 = 1$. The inner cylindrical area $(r < a)$ may be considered to have a third refractive index m_2. For the case of a cylindrical void, $m_0 = m_2$, but the calculation allows for the determination of momentum transfer to a more complex, "core-shell" structure, or filled cylinder with $m_2 \neq m_0$ and $m_2 \neq m_1$. Following the derivation outlined in Bohren and Huffman[58] for perpendicular incidence, with the cylinder axis along $\hat{z}$, the electric field can

be expanded in orthogonal cylindrical vector harmonics

$$\mathbf{M}_n^{(1,2)} = km\left(\frac{in}{\rho}Z_n^{(1,2)}(\rho)\,\hat{r} - Z'n^{(1,2)}(\rho)\,\hat{\phi}\right)e^{in\phi}, \tag{4.6}$$

$$\mathbf{N}_n^{(1,2)} = kmZ_n^{(1,2)}(\rho)\,e^{in\phi}\hat{z}, \tag{4.7}$$

where n is an integer, $Z_n^{(1)}(\rho) = J_n(\rho)$ and $Z_n^{(2)} = H_n^{(1)}(\rho)$, $Z_n'(\rho) = \frac{\partial Z_n(\rho)}{\partial\rho}$, $\rho = kmr$, and m is the refractive index, where $m = \sqrt{\frac{\mu\epsilon}{\mu_\circ\epsilon_\circ}}$.

The incident field, $\mathbf{E}_{inc} = \mathbf{E}_\circ e^{-i(\mathbf{k}\cdot\hat{\mathbf{x}}+\omega t)}$, parallel or perpendicular to the x-z plane, can be expressed as

$$\mathbf{E}_{inc}^{\parallel} = \sum_{n=-\infty}^{\infty} E_n\mathbf{N}_n^{(1)}, \tag{4.8}$$

$$\mathbf{E}_{inc}^{\perp} = -i\sum_{n=-\infty}^{\infty} E_n\mathbf{M}_n^{(1)}. \tag{4.9}$$

where the time dependence has been suppressed and $E_n = \frac{E_\circ(-i)^n}{km}$. Using Maxwell's equation, $\bigtriangledown \times \mathbf{E} = -\mu_\circ\frac{\partial\mathbf{H}}{\partial t}$, the incident magnetic fields are then

$$\mathbf{H}_{inc}^{\parallel} = -\frac{ikm}{\omega\mu_\circ}\sum_{n=-\infty}^{\infty} E_n\mathbf{M}_n \tag{4.10}$$

$$\mathbf{H}_{inc}^{\perp} = -\frac{km}{\omega\mu_\circ}\sum_{n=-\infty}^{\infty} E_n\mathbf{N}_n. \tag{4.11}$$

The internal and scattered external fields can be expanded as follows
For parallel incidence

$r > b$

$$\mathbf{E}^{\parallel} = -\sum_{n=-\infty}^{\infty} E_n a_n \mathbf{N}_n^{(2)}$$
$$\mathbf{H}^{\parallel} = \frac{ikm_0}{\omega\mu_\circ} \sum_{n=-\infty}^{\infty} E_n a_n \mathbf{M}_n^{(2)}$$

$b > r > a$

$$\mathbf{E}^{\parallel} = \sum_{n=-\infty}^{\infty} E_n \left[b_n \mathbf{N}_n^{(1)} - c_n \mathbf{N}_n^{(2)} \right]$$
$$\mathbf{H}^{\parallel} = -\frac{ikm_1}{\omega\mu_\circ} \sum_{n=-\infty}^{\infty} E_n \left[b_n \mathbf{M}_n^{(1)} - c_n \mathbf{M}_n^{(2)} \right]$$

$a > r$

$$\mathbf{E}^{\parallel} = \sum_{n=-\infty}^{\infty} E_n d_n \mathbf{N}_n^{(1)}$$
$$\mathbf{H}^{\parallel} = -\frac{ikm_2}{\omega\mu_\circ} \sum_{n=-\infty}^{\infty} E_n d_n \mathbf{M}_n^{(1)}$$

For perpendicular incidence

$r > b$

$$\mathbf{E}^{\perp} = i \sum_{n=-\infty}^{\infty} E_n f_n \mathbf{M}_n^{(2)}$$
$$\mathbf{H}^{\perp} = \frac{km_0}{\omega\mu_\circ} \sum_{n=-\infty}^{\infty} E_n f_n \mathbf{N}_n^{(2)}$$

$b > r > a$

$$\mathbf{E}^{\perp} = -i \sum_{n=-\infty}^{\infty} E_n \left[g_n \mathbf{M}_n^{(1)} - h_n \mathbf{M}_n^{(2)} \right]$$
$$\mathbf{H}^{\perp} = -\frac{km_1}{\omega\mu_\circ} \sum_{n=-\infty}^{\infty} E_n \left[g_n \mathbf{N}_n^{(1)} - h_n \mathbf{N}_n^{(2)} \right]$$

$a > r$

$$\mathbf{E}^{\perp} = -i \sum_{n=-\infty}^{\infty} E_n j_n \mathbf{M}_n^{(1)}$$
$$\mathbf{H}^{\perp} = -\frac{km_2}{\omega\mu_\circ} \sum_{n=-\infty}^{\infty} E_n j_n \mathbf{N}_n^{(1)}$$

Using these expressions the total fields, incident plus scattered, surrounding

the particle can be expressed as

$$\mathbf{E}^{\parallel} = \sum_{n=-\infty}^{\infty} E_n \left(\mathbf{N}_n^{(1)} - a_n \mathbf{N}_n^{(2)} \right), \tag{4.12}$$

$$\mathbf{H}^{\parallel} = -\frac{ikm_0}{\omega \mu_\circ} \sum_{n=-\infty}^{\infty} E_n \left(\mathbf{M}_n^{(1)} - a_n \mathbf{M}_n^{(2)} \right), \tag{4.13}$$

$$\mathbf{E}^{\perp} = -i \sum_{n=-\infty}^{\infty} E_n \left(\mathbf{M}_n^{(1)} - f_n \mathbf{M}_n^{(2)} \right), \tag{4.14}$$

$$\mathbf{H}^{\perp} = -\frac{km_0}{\omega \mu_\circ} \sum_{n=-\infty}^{\infty} E_n \left(\mathbf{N}_n^{(1)} - f_n \mathbf{N}_n^{(2)} \right). \tag{4.15}$$

The scattering coefficients for two concentric cylinders were derived as this particular geometry was chosen for study. These coefficients, a_n and f_n result from the boundary conditions at each cylinder interface

$$(\mathbf{E}_{inc} + \mathbf{E}_{scat} - \mathbf{E}_{int}) \times \hat{\mathbf{r}} = (\mathbf{H}_{inc} + \mathbf{E}_{scat} - \mathbf{H}_{int}) \times \hat{\mathbf{r}} = 0, \tag{4.16}$$

and have the values

$$a_n = \frac{\begin{vmatrix} m_0 J_n'(m_0\beta) & m_1 J_n'(m_1\beta) & -m_1 H_n'(m_1\beta) & 0 \\ J_n(m_0\beta) & J_n(m_1\beta) & -H_n(m_1\beta) & 0 \\ 0 & m_1 J_n'(m_1\alpha) & -m_1 H_n'(m_1\alpha) & -m_2 J_n'(m_2\alpha) \\ 0 & J_n(m_1\alpha) & -H_n(m_1\alpha) & -J_n(m_2\alpha) \end{vmatrix}}{\begin{vmatrix} m_0 H_n'(m_0\beta) & m_1 J_n'(m_1\beta) & -m_1 H_n'(m_1\beta) & 0 \\ H_n(m_0\beta) & J_n(m_1\beta) & -H_n(m_1\beta) & 0 \\ 0 & m_1 J_n'(m_1\alpha) & -m_1 H_n'(m_1\alpha) & -m_2 J_n'(m_2\alpha) \\ 0 & J_n(m_1\alpha) & -H_n(m_1\alpha) & -J_n(m_2\alpha) \end{vmatrix}}, \tag{4.17}$$

$$f_n = \frac{\begin{vmatrix} J_n'(m_0\beta) & J_n'(m_1\beta) & -H_n'(m_1\beta) & 0 \\ m_0 J_n(m_0\beta) & m_1 J_n(m_1\beta) & -m_1 H_n(m_1\beta) & 0 \\ 0 & J_n'(m_1\alpha) & -H_n'(m_1\alpha) & -J_n'(m_2\alpha) \\ 0 & m_1 J_n(m_1\alpha) & -m_1 H_n(m_1\alpha) & -m_2 J_n(m_2\alpha) \end{vmatrix}}{\begin{vmatrix} H_n'(m_0\beta) & J_n'(m_1\beta) & -H_n'(m_1\beta) & 0 \\ m_0 H_n(m_0\beta) & m_1 J_n(m_1\beta) & -m_1 H_n(m_1\beta) & 0 \\ 0 & J_n'(m_1\alpha) & -H_n'(m_1\alpha) & -J_n'(m_2\alpha) \\ 0 & m_1 J_n(m_1\alpha) & -m_1 H_n(m_1\alpha) & -m_2 J_n(m_2\alpha) \end{vmatrix}}. \tag{4.18}$$

where $\alpha = kr_a$, $\beta = kr_b$, the radii illustrated in figure 4.1. We note that a similar derivation was first completed by Kerker and Matijevic in 1961.[71]

The net momentum flux can be found using the total fields in the time averaged Maxwell stress tensor

$$\left\langle T_{\alpha\beta} \right\rangle = \frac{1}{2} Re \left[\epsilon_0 E_{n\alpha} E_{l\beta}^* + \mu_0 H_{n\alpha} H_{l\beta}^* - \frac{1}{2} \left(\epsilon_0 \left| E_{nl} \right|^2 + \mu_0 \left| H_{nl} \right|^2 \right) \delta_{\alpha\beta} \right]. \tag{4.19}$$

The total momentum transferred to the cylinder is then

$$\Delta \mathbf{p}_x = \int_0^{2\pi} \left(\hat{\mathbf{x}} \cdot \left\langle \mathbf{T}_{\alpha,\beta}^{tot} \right\rangle \cdot \hat{\mathbf{r}} \right) r \mathrm{d}\phi. \tag{4.20}$$

Referring back to equations 4.21 and 4.22, the Maxwell stress tensor will have ϕ dependence that goes as $e^{i(n-l)\phi}$. This combined with the $cos(\phi)$ and $sin(\phi)$ terms introduced by $\hat{x}$ will limit the allowed values of l to $l = (n \pm 1)$. Taking the limit as $r \to \infty$ and averaging over a period, the total momentum transfer is found to be

$$\Delta \mathbf{p}_x^{\parallel} = \frac{\left| E_\circ \right|^2}{8 k m_0 \mu_\circ \omega^2} \left[\left(k^2 m_0^2 \pi^2 + 4 \epsilon_\circ \mu_\circ \omega^2 \right) \left(a_{n-1}^* + a_{n+1}^* - 2 a_n \left(a_{n-1}^* + a_{n+1}^* - 1 \right) \right) \right], \tag{4.21}$$

$$\Delta \mathbf{p}_x^{\perp} = \frac{\left| E_\circ \right|^2}{8 k m_0 \mu_\circ \omega^2} \left[\left(4 k^2 m_0^2 + \pi^2 \epsilon_\circ \mu_\circ \omega^2 \right) \left(2 f_n \left(f_{n-1}^* + f_{n+1}^* - 1 \right) - f_{n-1}^* - f_{n+1}^* \right) \right]. \tag{4.22}$$

These values are then averaged over polarizations and normalized by the incident momentum per unit length,

$$p_{inc} = \int_{-b}^{b} \hat{x} \cdot \mathbf{T}^{inc}_{\alpha,\beta} \cdot \hat{x} \, \mathrm{d}x. \tag{4.23}$$

4.3 Numerical evaluation of the momentum transfer

The total force transferred to a two dimensional cross section of a pair of infinite concentric cylinders was calculated numerically by decomposing a non-focused beam, of width equal to that of the particles outer diameter, into 10^6 rays, each with unit momentum. Each ray was injected with a direction of incidence normal to the cylinder axis and allowed four intersections. The scattering force for each intersection was found using the algorithm outlined in chapter 2. The beam aperture was set equal to the diameter of the circle and the shape held centered over the aperture. In this configuration the scattering force is the only force possible, as all gradient forces will cancel by symmetry. Once the total force on the shape had been found this value was divided by the number of rays injected, resulting in a normalized scattering force.

The scattering force, per unit length, was examined as a function of inner cylinder radius. Holding the outer radius constant at 5 μm the inner radius was steadily increased and the scattering force calculated using both Generalized Lorenz-Mie theory and the numeric geometric optics simulation. This process allowed examination of both cavity sizes and wall thicknesses on the order of the wavelength of incident light, $\lambda = 400$ nm.

4.3.1 Very small cavities or very thin rings

As is illustrated in Figure 4.2, for small cavity sizes, $\frac{R_{outer} - R_{inner}}{\lambda} > 8$ we find that the numerical optics simulation actually underestimates the scattering force.

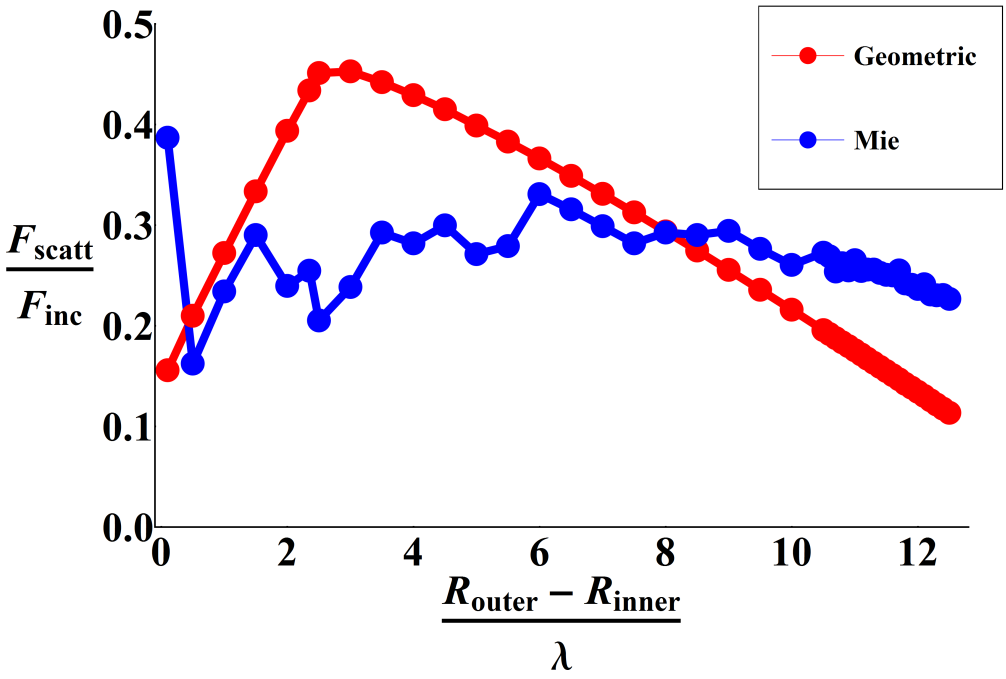

Figure 4.2: Geometric ray optics and Mie result for the normalized scattering force for a pair of concentric dielectric cylinders, $\frac{r_{outer}}{\lambda} = 12.5$, and indices of refraction $m_0 = 1.33, m_1 = 1.66, m_2 = 1.33$ as a function of r_{inner}, where $\lambda = 400$ nm

This underestimation increases with decreasing cavity size. However, we note that the error made in the computation of the scattering force from very small cavities is not significant in computing the overall trapping force. While the corrections due to physical optics are large relative to the geometric optics calculation, they are still small forces when compared to the larger gradient forces. These gradient forces are neglected here since we used an unfocused incident beam, but in the typical laser trapping geometry scattering from small cavities is a sub-dominant correction to the geometric optics result. We make similar statements with regard to the case of very large cavities, i.e. very thin rings.

Examining the interaction of the incident field with the inner cavity from both the Mie and numerical standpoints offers some insight into underestimation of the scattering force on the part of geometric optics. In the numerical simulations the interaction of the ray and any interface is binary, the ray either intersects and transfers momentum or it does not. As we are using an unfocused beam increasing the inner cavity radius serves to directly increase the likelihood of intersection. For very small cavities, the geometric optics cross section is simply the geometric cross section of the cavity which goes to zero in the limit of a point scatterer. We expect, however, the full physical optics result to reduce to the Rayleigh limit for such a small cavity. For that case we know there is a residual, finite momentum transfer. Thus the geometric solution must underestimate the momentum transfer, as is seen. Indeed, we see a decrease in the underestimation of the scattering force as the inner cavity size is increased.

In the other extreme, cavity sizes large enough to leave a ring of dielectric of thickness less than the wavelength of incident light, we again see underestimation of the total scattering force on the part of the numerical geometric optics simulation. From the geometric optics standpoint any ray moving through

the higher dielectric media is going to experience the two interfaces which are nearly parallel. As will be discussed in the next chapter passage through a dielectric slab, passing through two parallel interfaces, simply translates the ray along the slab; there is no change in direction of the ray vector. Using the full physical optics solution accounts for diffraction about both the edges of the outer ring and the inner ring, redirecting the direction of light propagation. As all of the light is propagating in the positive y direction any diffraction about the shape would result in a scattering force.

4.3.2 Ring thickness of order λ

In this regime the cavity size is such that the remaining ring thickness is on the order of the wavelength of incoming radiation. It is in this size regime that we expect to observe the actual momentum transfer, (i.e. as calculated from the full physical optics based analysis) to be less than that obtained in the geometric optics approximation. We find this indeed to be the case. In this intermediate regime, we find that the geometric ray optics simulations overestimate the scattering force by as much as a factor of two.

Returning briefly to the experiments conducted by Wilking and collaborators we see this overestimation on the part of geometric optics simulation illustrated in direct comparison to the experimental results. As both the particle geometry and size differ between the experimental and simulation results, the correct particle shape from those used in the simulations was chosen based upon scaled total dielectric area. The equations used in geometric ray optics have no dependence on the particle size and an outer radius of $1\,\mu m$ was therefore used. The scaling factor, β, can be determined as follows

$$\pi \left(\beta R_{outer}\right)^2 = L_{\circ}^2, \tag{4.24}$$

where $L_{\circ}$ is the edge length of the particle used experimentally. As $R_{inner} =$

$1.0\,\mu m$ simple algebraic manipulation gives us $\beta = \frac{L_\circ}{\sqrt{\pi}}$. Using the total area of dielectric contained in a cross section of the particle displayed in 4.3a, $A_{exp} = L_\circ^2 - \pi R_{in,exp}^2$. With this value it is possible to determine the correct inner radius, of those used in the simulations, for direct comparison to the experimental results

$$A_{exp} = \pi\beta^2 \left(R_{outer}^2 - R_{inner}^2 \right), \tag{4.25}$$

$$R_{inner} = \sqrt{R_{outer}^2 - \frac{A}{\pi\beta^2}}\,. \tag{4.26}$$

Using Wilking's reported values, $L_\circ = 4.5\,\mu m$ and $R_{in,exp} = 0.4\,\mu m$, we find that $\beta = 2.538$ and the unscaled inner radius which results in an equal cross sectional area of dielectric is $R_{inner} = 0.157\,\mu m$ or $\approx 0.2\,\mu m$. With the correct inner radius chosen we applied the scaling factor β to both the inner and outer radii, resulting in values of $R_{outer} = 2.538\,\mu m$ and $R_{inner} = 0.507\,\mu m$. The ring thickness for our scaled particle, normalized by the wavelength used in Wilking's experiment, 633 nm, is therefore $\frac{R_{outer,scaled} - R_{inner,scaled}}{\lambda} = 3.208$. Referring back to figure 4.2 this value falls exactly in the region where overestimation of the scattering force by the geometric optics simulation is at its highest.

For trapping of a two dimensional symmetric particle, with its axis of symmetry located along the beam axis, any scattering forces will be in the direction of beam incidence. All others will cancel by symmetry. This is, therefore, a perfect test case to examine the effect the geometric optics simulation overestimation of the scattering force has on the trapping behavior of the particle.

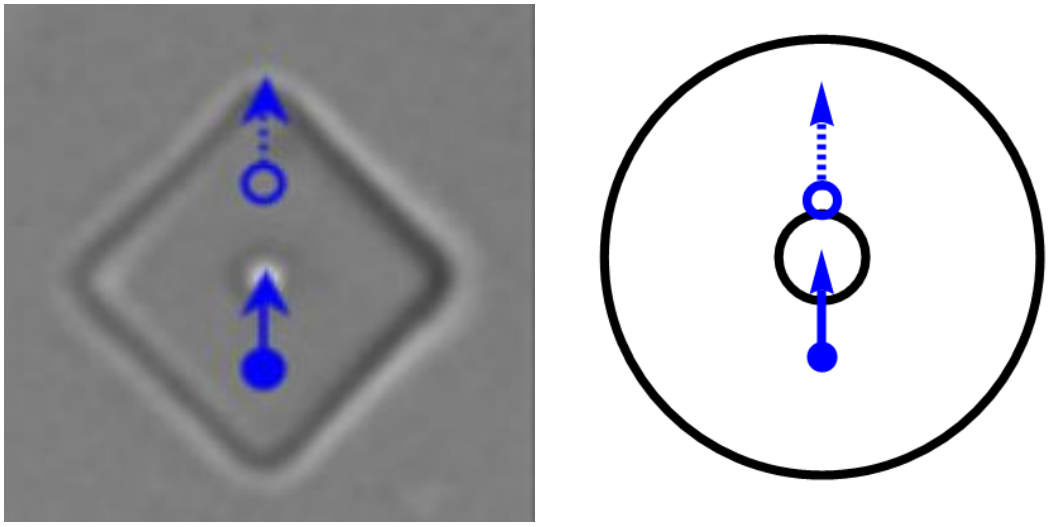

(a) (b)

Figure 4.3: On axis trapping for (a) Wilking and collaborator's[9] colloidal dielectric diamond, edge lengths 4.5 μm and cavity diameter 0.8 μm, (b) A circular shape with approximately the same area of dielectric material (following direct scaling), $R_{outer} = 1.0\,\mu m$, $R_{inner} = 0.2\,\mu m$. The blue circles represent the position of the focal point of the beam in both cases; with solid circles denoting stable trapping and open circles representing short-lived metastable trapping.

Figure 4.3 beautifully illustrates this overestimation. Our geometric optics simulation find the same on axis trapping points, but due to overestimation of the scattering forces both are shifted up the beam axis. The blue arrow in both images denotes the direction of beam incidence. The solid blue circle represents the focal point of the beam for a long lived stable trapping position of the particle. We can see that in this stable trapping position, where the gradient force dominates, the stable trapping position found through our simulations is very near to that found experimentally. The open circle in fig 4.3a represents the position of the focal point of the beam for an experimentally found short lived metastable trapping state.

Examination of fig 4.3b drives home the overestimation of the scattering

force on the part of geometric ray optics. At the metastable trapping point the potential well depth will, by definition, be smaller than that for a long lived stable trapping point. The scattering forces are therefore making a larger contribution and are no longer sub-dominant. As the open circle in fig 4.3b is lower than that found in fig 4.3a the metastable trapping position found in our simulation occurs with the center of the particle shifted up along the beam axis.

As the stable trapping position calculated using geometric optics was examined in detail in section 3.3.2.2 of chapter 3 we shall refrain from discussing them again. For the metastable trapping position we do find a potential minimum, fig 4.4.

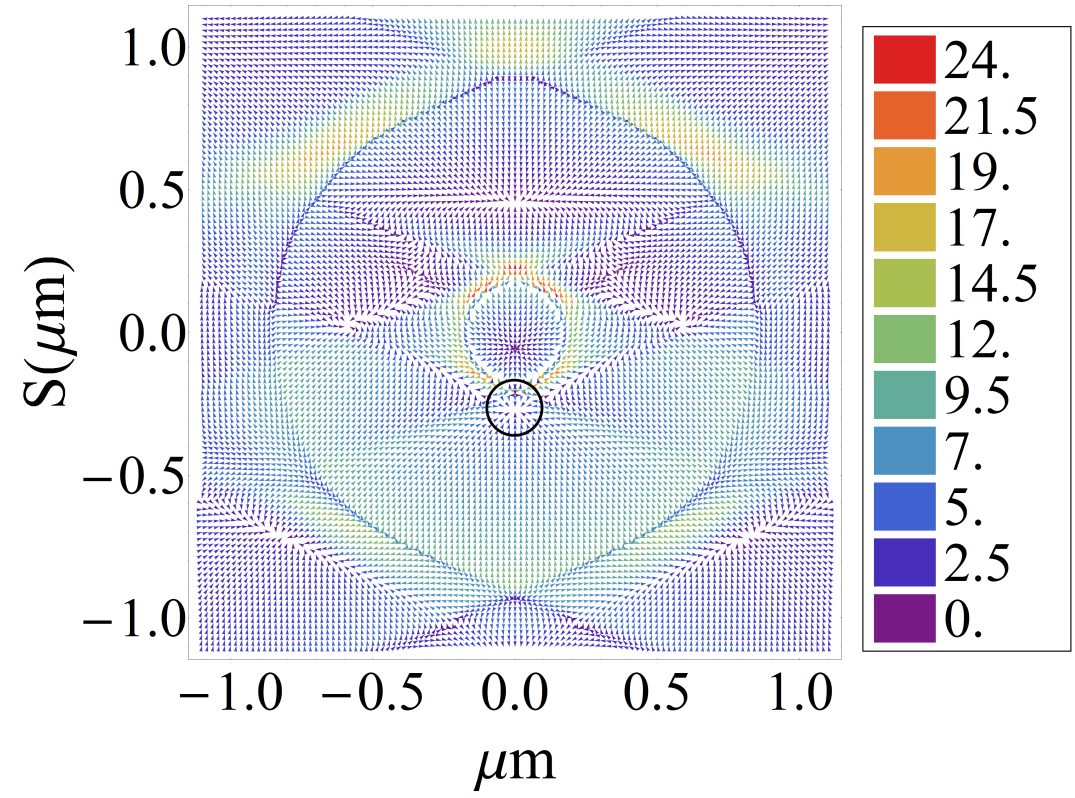

(a)

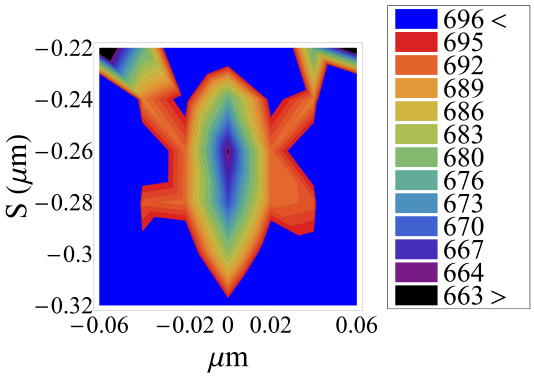

(b)

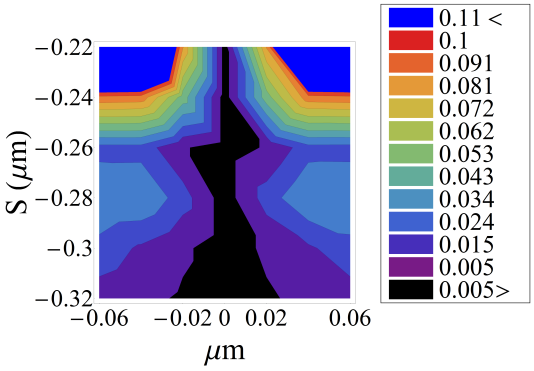

(c)

Figure 4.4: (a) The force field calculated for the particle illustrated in figure 4.3b, the black circle encompasses the region of metastable trapping. (b) The potential surface in this region, well depth $\approx 29\,k_B T$. (c) The magnitude of the net work, calculated using a closed integral about each point in the force field array, normalized by the potential at that point.

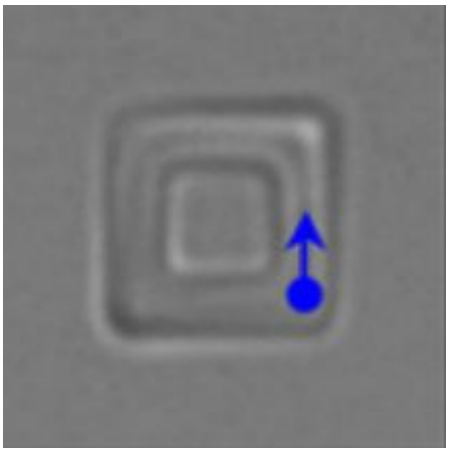

Figure 4.5: The particle for which reentrant trapping occurred in Wilking and collaborator's experiments. The blue circle represents the focal point of the beam and the blue arrow the direction of beam propagation. The particle dimensions are $L_\circ = 4.5\,\mu m$ for the outer edges and $L_i = 2.5$ for the inner cavity edges.[9]

Returning to the reentrant trapping results of Wilking and collaborator's experiments it is tempting to attribute the geometric optics failure to find reentrant trapping completely to diffraction effects. Wilking's reentrant trapping particle, fig 4.5, had a ring thickness of approximately a micron, where $L_\circ = 4.5\,\mu m$ and the length of the inner square cavity $L_i = 2.4\,\mu m$. If shape geometry were not a contributing factor we would be able to switch between $L_\circ$ and R_{outer} seamlessly. If we assume this is the case we have a 1 micron ring thickness, for the square particle which exhibited reentrant trapping, and incident radiation wavelength of $633\,nm$ in Wilking's experiment and $\frac{R_{outer}-R_{inner}}{\lambda} = 1.66$. Referring back to figure 4.2 we see the overestimation of the scattering force by the geometric optics calculation is at a minimum in this range of values. Diffraction effects cannot, then, be the sole cause of the reentrant trapping being missed by the geometric optics simulation for this particular particle geometry. As will be shown in the next chapter both the particle geometry and diffraction play a role in the trapping behavior, and we

do in fact find stable trapping for a rectangular shape whose geometry mimics the third dimension of Wilking's particle.

From these results we find that the overall effect of geometric optic's neglect of diffraction is most pronounced in cases where the gradient and scattering force are in delicate balance. For symmetric particles on-axis metastable trapping points could quite possibly be missed by the geometric optics if any of the characteristic particle lengths are on the order of the wavelength of the incident radiation. Off-axis, where the scattering forces cannot directly cancel, the non-zero net scattering force coupled with geometric optics overestimation will likely lead to stable trapping points being missed by the geometric optics calculation. These points highlight the importance of going beyond the Ashkin approximation and its generalization presented here when considering the trapping force of laser tweezers on a particle with internal dimensions comparable to the wavelength of the trapping radiation.

CHAPTER 5

Trapping Behavior of Non-Symmetric Shapes

5.1 Introduction

An L shape was chosen as the model for investigation of the trapping behavior of non-symmetric shapes. Beyond the introduction of torques, the planar nature of the L shape gives rise to several interesting phenomena from the ray optics standpoint. As will be discussed in the following sections, a ray of light, averaged over polarizations and passing through two parallel interfaces, can only result in a scattering force. In order to exert a force against the direction of beam propagation the ray must travel a path through two perpendicular interfaces. Additionally, incident rays with $\theta_i < \theta_c$ will experience solely total internal reflection for each intersection with a perpendicular interface, until a parallel interface is reached, allowing only for scattering forces.

An L shape can therefore only trap with any portion of the higher index media positioned below the focal point if its shorter axis is sufficiently thin that the internal rays intersect a perpendicular interface and are still carrying enough momentum that the resulting gradient force can offset the scattering force. If the longer axis of the planar shape is perpendicular to the direction of beam incidence trapping is only possible with all of the higher dielectric media positioned above the focal point of the beam. In the next section both cases, the longer axis of the shape parallel or perpendicular to the beam axis, will be examined analytically.

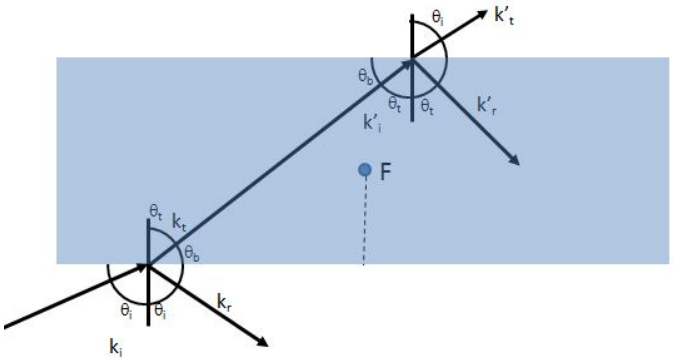

Figure 5.1: Possible angles of incidence and transmission for a ray intersecting an infinite slab.

5.2 Modes of ray propagation for planar shapes

5.2.1 Long axis perpendicular to the direction of beam incidence

In the interest of simplicity we first consider an infinitely long shape with parallel boundaries oriented perpendicular to the direction of beam incidence and positioned below the focal point of the beam. As is illustrated in figure 5.1 the angle of incidence for the ray entering the higher dielectric media is exactly equal to the angle of transmission for the ray leaving the higher dielectric media. Any change in the ray momentum is accounted for by the fraction of light reflected at each interface, which by conservation of momentum results in a force on the higher dielectric in the direction of ray propagation. Adding edges, and therefore perpendicular interfaces, to the boundaries of higher dielectric allows for a net change in the component of the ray parallel to the direction of beam incidence, figure 5.2. Using $\theta_t = \sin^{-1}\left(\frac{\sin\theta_i}{m}\right)$, $\theta_b = \frac{\pi}{2} - \theta_t$, and $\theta_t^* = \sin^{-1}\left(\sqrt{m^2 - \sin^2\theta_i}\right)$, we can define $\rho_1 = \frac{\cos\theta_t}{\cos\theta_i}$ for the first intersection with the ray incident from the lower dielectric medium, n_1 and $\rho_2 = \frac{\cos\theta_t^*}{\cos\theta_b}$ for the ray incident from the higher dielectric medium, n_2;

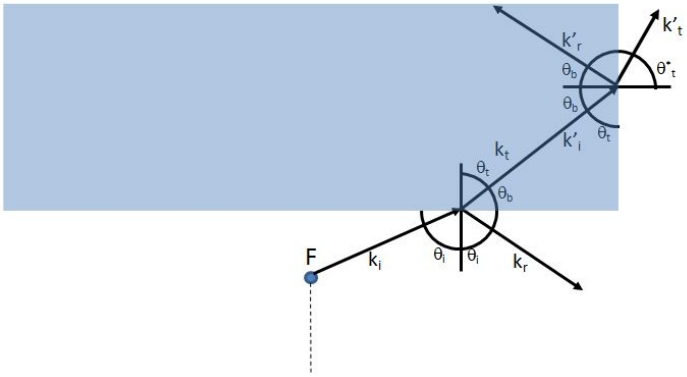

Figure 5.2: Possible angles of incidence and transmission for a ray intersecting a slab with edges. The slab is positioned above the focal point, F, as there is greater likelihood of intersecting the edges in this position.

where $m = \frac{n_2}{n_1}$. From the definitions of θ_t^*, θ_b and θ_t there will be some angle of incidence, θ_i for which the second intersection always results in total internal reflection. Starting at the second intersection, and using the relationship between $\theta_b = \frac{\pi}{2} - \theta_t$, for total internal reflection at the second interface $\theta_t = cos^{-1}\left(\frac{1}{m}\right)$. The critical angle of incidence at the first intersection is therefore $\theta_c = sin^{-1}\left(\sqrt{m^2-1}\right)$. Reexamination of ρ_2,

$$\begin{aligned} \rho_2 &= \frac{\cos\theta_t^*}{\cos\theta_b} \\ &= \frac{\cos\left(\sin^{-1}\left(\sqrt{m^2-sin^2\theta_i}\right)\right)}{\cos\theta_b} \\ &= \frac{\sqrt{1-\left(\sqrt{m^2-\sin^2\theta_i}\right)^2}}{\cos\theta_b} \\ &= \frac{\sqrt{1+\sin^2\theta_i-m^2}}{\cos\theta_b} \end{aligned} \tag{5.1}$$

shows that ρ_2 becomes imaginary for values of $\theta_i < \theta_c$. In other words, at the second intersection the ray will experience total internal reflection rather than transmission from the high index medium to the low index medium.

Additionally as the value of m for the second intersection, $m' = \frac{1}{m}$, the Fresnel equations, averaged over polarizations, are only dependent upon the

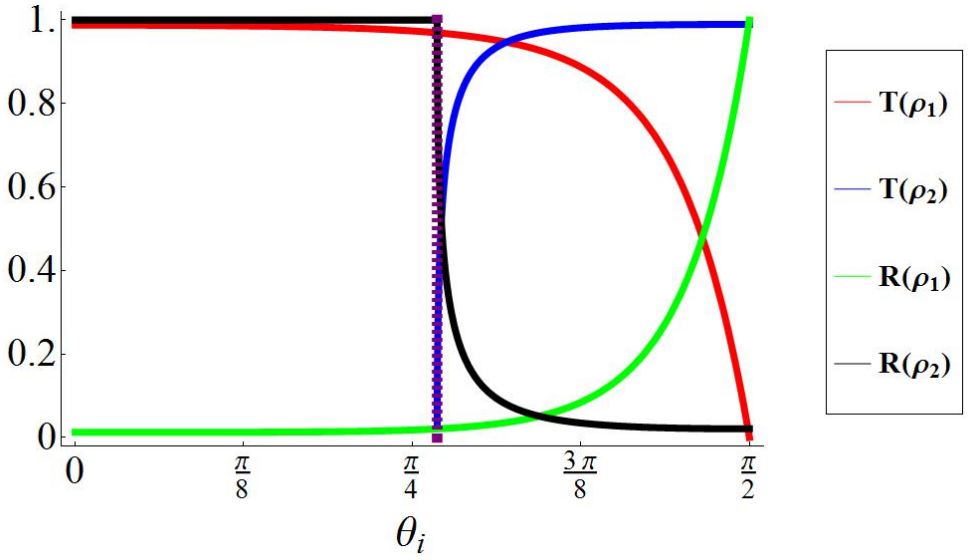

Figure 5.3: Fraction of momentum transmitted and reflected at each interface as a function of angle of incidence, θ_i for a slab with two perpendicular interfaces and $m = 1.25$, $\theta_c \approx \frac{4\pi}{15}$ and represented by a purple dashed line.

value of ρ. We can therefore generally define

$$R(\rho) = \frac{1}{2}\left(\left(\frac{1-m\rho}{1+m\rho}\right)^2 + \left(\frac{\rho-m}{\rho+m}\right)^2\right)$$
$$T(\rho) = \frac{m\rho}{2}\left(\left(\frac{2}{1+m\rho}\right)^2 + \left(\frac{2}{\rho+m}\right)^2\right), \tag{5.2}$$

and using these functions examine the transmission and reflection coefficients for both the first and second points of intersection, $T_1 = T(\rho_1)$, $R_1 = R(\rho_1)$, $T_2 = T(\rho_2)$ and $R_2 = R(\rho_2)$. These functions are plotted as a function of θ_i for $m = 1.25$ in figure 5.3. Referring to figure 5.2 once again we see that the components of the incident ray at the first intersection can be expressed as $(sin(\theta_i), cos(\theta_i))$ and those of the transmitted ray at the second intersection as $(cos(\theta_t^*), sin(\theta_t^*))$. As transmission at the second intersection requires that $\theta_i < \theta_c$, the component of the transmitted ray at the second intersection parallel to the direction of beam incidence will always be larger than the same component of the incident ray. These transmitted rays can therefore only con-

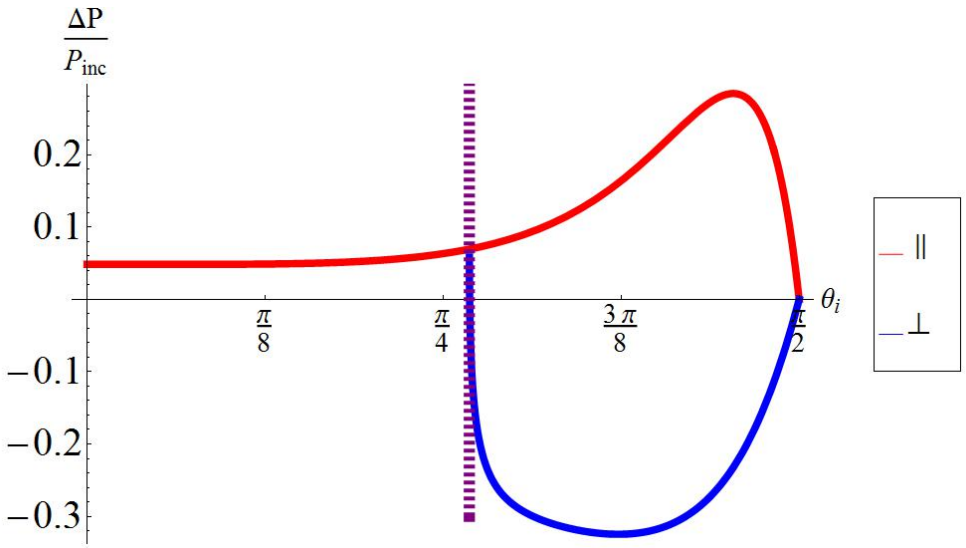

Figure 5.4: Comparison of the net force, following two intersections with either two parallel interfaces (red) or two perpendicular interfaces (blue), for a slab oriented with its long axis perpendicular to the direction of beam incidence; $m = 1.25$, $\theta_c \approx \frac{4\pi}{15}$ (purple dashed line).

tribute to the trapping force. Figure 5.4 illustrates the net force, following two intersections, for rays intersecting two parallel planes and rays intersecting two perpendicular planes as a function of angle. Where the component of the net force parallel to the direction of beam incidence which is transferred to the slab can be calculated as,

$$\begin{aligned} \Delta p^{\parallel} &= (1+R_1)\cos\theta_i - T_1\cos\theta_t + T_1\left((1+R_1)\cos\theta_t - T_2\cos\theta_i\right) \\ &= \left(1+R_1-T_1^2\right)\cos\theta_i + T_1R_1\cos\theta_t \qquad (5.3) \\ \Delta p^{\perp} &= (1+R_1)\cos\theta_i - T_1\cos\theta_t + T_1\left((1-R_2)\cos\theta_t - T_2\sin\theta_t^*\right) \\ &= (1+R_1)\cos\theta_i - T_1R_2\cos\theta_t - T_1T_2\sin\theta_t^* \qquad (5.4) \end{aligned}$$

5.2.2 Long axis parallel to the direction of beam incidence

The same arguments hold for case in which the long axis of the slab is oriented parallel to the direction of beam incidence. The difference is the trapping

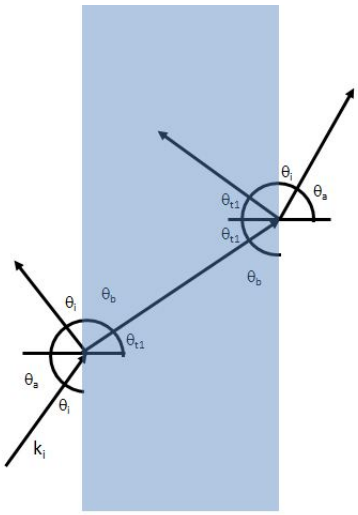

Figure 5.5: Angles of incidence and transmission for a vertical slab

position. Any rays intersecting the sides of the slab will still result in purely scattering forces. Rays incident upon the base of the slab will interact with two perpendicular interfaces, leaving either the option of total internal reflection or a contribution to the trapping force, as explained above. Referring to figure 5.5 we can define the component of the net force parallel to the direction of beam incidence as

$$\begin{aligned} \rho_3 &= \frac{\cos\theta_{t1}}{\cos\theta_a} \\ \Delta p_{wall} &= \left(1 - R_3 - T_3^2\right)\cos\theta_i - T_3 R_3 \sin\theta_t \end{aligned} \tag{5.5}$$

for rays intercepting the sides of the slab. For rays intersecting the base of the slab, figure 5.6, the parallel force component can be expressed as

$$\begin{aligned} \Delta p_{base} &= (1 + R_1)\cos\theta_i - T_1\cos\theta_t + T_1\left[(1 - R_2)\cos\theta_t - T_2\sin\theta_t^*\right] \\ &= (1 + R_1)\cos\theta_i - T_1 R_2\cos\theta_t - T_1 T_2\sin\theta_t^*. \end{aligned} \tag{5.6}$$

If the angle of incidence for rays intersecting the base of the plank is smaller than the critical angle the ray will experience total internal reflection until an interface parallel to the interface of the rays initial intersection, or the top of

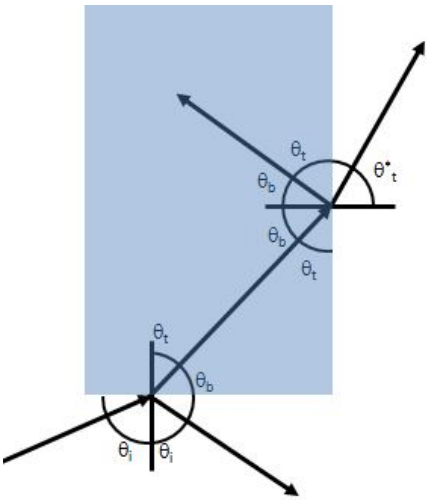

Figure 5.6: Angles of incidence and transmission for a ray entering the floor of the slab and exiting via a perpendicular wall

the shape, is reached. The total internal reflection parallel force component can therefore be expressed as

$$\Delta p_{base}^{TIR} = \left(1 + R_1 - T_1^2\right) \cos\theta_i + T_1 R_1 \cos\theta_t. \tag{5.7}$$

The Heaviside step function was used to correctly assign total internal reflection or transmission for rays intersecting the base of the shape as a function of θ_i. The contribution to the total force on the slab (following two intersections of the ray) was examined for rays initially intersecting the side of the slab, the base of the slab, or the total contribution for both the side and the base. As is illustrated in figure 5.7 any incident rays intersecting the slab at angles $\theta_i < \theta_c$ can only contribute a scattering force. In the case of rays intersecting the base, this scattering force contribution is due to total internal reflection. Rays intersecting the base at angles greater than the critical angle immediately begin to contribute a trapping force.

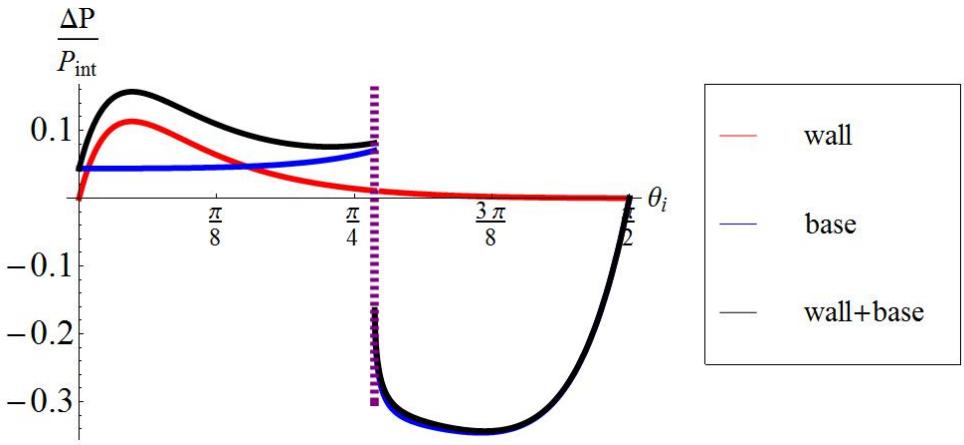

Figure 5.7: Component of the force parallel to the direction of beam incidence for a vertical slab, with its long axis parallel to the direction of incidence, as a function of the angle of incidence; θ_i, $m = 1.25$.. The force is decomposed into contributions due to intersection of the ray with the wall (red), which is parallel to the beam axis, and the base (blue), which is perpendicular to the beam axis, and the total force (black).

5.3 Simulation methods

For the L shape, line segments, illustrated in fig 5.8, set the length of each leg.

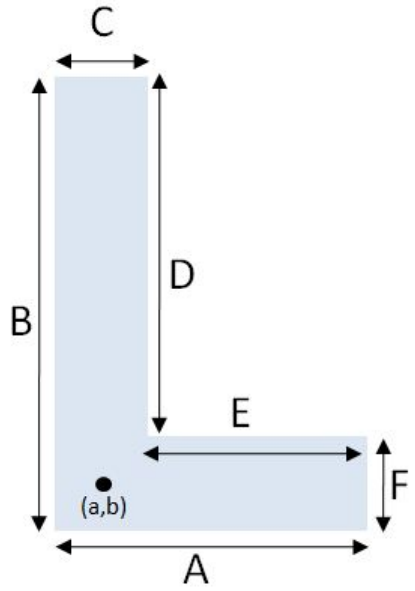

Figure 5.8: The vectors and point defining the L shape.

The leg lengths were used to define a set of six points

$$\begin{aligned} P_1 &= \left(a - \tfrac{C}{2}, b - \tfrac{F}{2}\right), \\ P_2 &= \left(a - \tfrac{C}{2} + A, b - \tfrac{F}{2}\right), \\ P_3 &= \left(a - \tfrac{C}{2}, b - \tfrac{F}{2} + F\right), \\ P_4 &= \left(a - \tfrac{C}{2} - E, b - \tfrac{F}{2}\right), \\ P_5 &= \left(a - \tfrac{C}{2} - E, b - \tfrac{F}{2} + D\right), \\ P_6 &= \left(a - \tfrac{C}{2}, b - \tfrac{F}{2} + D\right), \end{aligned} \tag{5.8}$$

and the vectors between them used to describe the shape boundaries.

5.4 Field sampling

The choice of step size for translating the shape through the sampling field is fairly straightforward for a shape with infinite axes of symmetry. In that case there is no change in trapping behavior with shape rotation. The outer di-

ameter of the symmetric shape was held constant and as interaction of highly angled rays with the shape boundaries result in trapping, the bounds of the sampling field can be reasonably be set to slightly larger than the diameter of the shape.

For a shape with only one or no symmetry axis the sampling field must be made large enough that all of the shape boundaries can interact with the beam at all orientations. In the case of the L shape small changes in shape position in relation to the focal point of the beam were found to have a large impact on the direction of forces for the shape and the net torque following rotation of the shape at that point. Additionally, as one would like to be able to iteratively increase the length of the leg and rotate the shape through multiple angles about the COM, the size of the sampling field cannot be kept constant. For the L shape the initial boundaries of the sampling field were defined as the length of leg B plus the length of leg C in both directions. This accounted for the $\theta = 0$ and $\pm\frac{\pi}{2}$ orientations of the L shape. This area was discretized into one thousand points and stable trapping checked for at each point. If a stable trapping point was found a new region was defined surrounding that point, using an area of eight steps in both the positive and negative x and y directions. The step size was decreased and a lattice of forty points evenly distributed throughout the sampling area was defined, the process repeated and stable trapping points searched for once again. This process was iterated up to four times or until the forces around the chosen stable trapping point were so small that the region of stable trapping had functionally been defined.

Once the stable trapping point and/or region had been selected a square area with lengths equal to two times the length of leg C was defined, centered on the stable trapping point and the field sampled once again. Stable trapping was checked for at each point and if a stable trapping point was found the field was redefined, again with using a square with edge lengths equal to two

times the length of leg C, around the new stable trapping point.

5.4.1 Torques for non-symmetric shapes

For a non-symmetric shape, such as a chevron, stable trapping is not only a function of the gradient and scattering forces, but also the net torque imparted to the particle by the beam. The simulation process is more involved for non-symmetric shapes as particle orientation with respect to the beam has a direct impact on the particle's trapping behavior. To simulate the non-symmetric shape and beam interactions statically the shape must be rotated and allowed to sample the field over a range of angles, as it cannot reorient spontaneously in response to imparted torques. As the shape position is determined using coordinates (a,b), and the boundaries defined from this point; rotation of the shape is a two step process. The shape is initially held at zero rotation and the center of mass is calculated based upon the shape boundaries. Using the example of a L shape illustrated in figure 5.8, centered at point (a,b) with the longer leg parallel to the direction of beam incidence, the COM can be calculated as

$$COM = \frac{BC(2a - 2b + B) + F(2b(2C - E) - CB + E(2a + C - E))}{2(BC + EF)}, \tag{5.9}$$

using the substitutions $A = C + E$ and $D = B - F$. Following this calculation each point defining the boundaries of the shape, equations 5.8, are then rotated about the COM. The now redefined shape boundaries are allowed to interact with the injected rays representing the beam, a net momentum value calculated using the process described previously in chapter 2, the shape is translated to the next point in the field sampling lattice and the process is repeated.

5.5 Stable trapping

To verify the stability of each trapping point the L shape is held at the previously found possibly stable trapping point and rotated, stepwise, through angles $-\pi \leq \theta \leq \pi$, with $\Delta\theta = \frac{\pi}{100}$. The positive y-axis represents $\theta = 0$ with θ increasing in the counterclockwise direction. If rotation of the L shape about its center of mass, in either the positive or negative θ direction, results in a restoring torque; and if the restoring torques are equal and opposite for opposite directions of rotation, the particle is still considered to be at possibly stable trapping point. To verify stable trapping the scalar potential and net work for the closed integral about each point in the force field is examined, with the potential defining stable trapping points and the net work verifying that a scalar potential can be used. The potential for each vector field is calculated stepwise using the dot product of the force with the change in position. The net work is calculated by taking the line integral about each point, using the average of two adjacent force vectors. For a particle to be stably trapped the all of the following must be true

1. The force vector field demonstrates stable trapping, all vectors pointing inward at that point.

2. Any rotation of the particle results in a restoring torque at that point **and** the restoring torques are equal and opposite in both directions.

3. The scalar potential field shows a well depth of at least $4k_BT$, the approximate thermal energy of a system equilibrated with its surroundings at room temperature.

4. A scalar potential field can be used, which is verified by a value for the net work of ≈ 0.

5.6 Simulation results

Ray optics simulations were performed to investigate the interplay of the ray being allowed to intersect perpendicular interfaces with the balance of torque required for the shape to stably trap. A 10mW beam entering a lens with numerical aperture of 1.4, traveling through bulk media with dielectric constant $n_1 = 1.33$ and interacting with dielectric material $n_2 = 1.66$ was decomposed into 1000 discrete rays. Each shape was first rotated about its center of mass from angles $\theta = -\pi$ to π. Following rotation the shape was allowed to sample a region large enough that in any direction no portion of the higher dielectric intersected the focal point of the beam. For angles at which a stable trapping point was found the shape was then rotated about its center of mass once again through angles $\theta_{trap} \pm \frac{\pi}{25}$ to verify restoring torques existed upon rotation. Referring back to figure 5.8 the leg length E was initially set to zero and incremented up to $E = 3.0$ μ m in steps of $\Delta E = 0.1$. For each shape trapping points were found for multiple angles of rotation. Each of these trapping points were examined and the final stable trapping point selected based upon the torque at that angle of rotation, the depth of the potential well and the value of the net work at the point being examined.

Ideally the beam would be discretized into more than 1000 rays. Due to the shear number of iterations necessary for sampling of 31 shapes, each rotated through 200 angles and run through repeated iterations of field sampling, a larger sample size for the beam would have led to prohibitively long run times for the code. If one were investigating the trapping behavior of a smaller sampling of shape sizes, or were to modify the code for parallel computing (perhaps running one point in the sampling field, or one angle, on each thread) a larger number of rays could easily be used.

For the 1000 ray simulation trapping was found to occur for shapes with

leg lengths $0 \leq L(E) \leq 0.3$ and $2.2 \leq L(E) \leq 3.0$. Any values of $L(E)$ in the range $0.4 \leq L(E) \leq 2.1$ did not stably trap. Figures 5.9 and 5.10 illustrate the angles each shape trapped at, as a function of their leg length. For reference the blue dot in each illustration represents the focal point and the red dot represents the shapes center of mass, about which it was rotated.

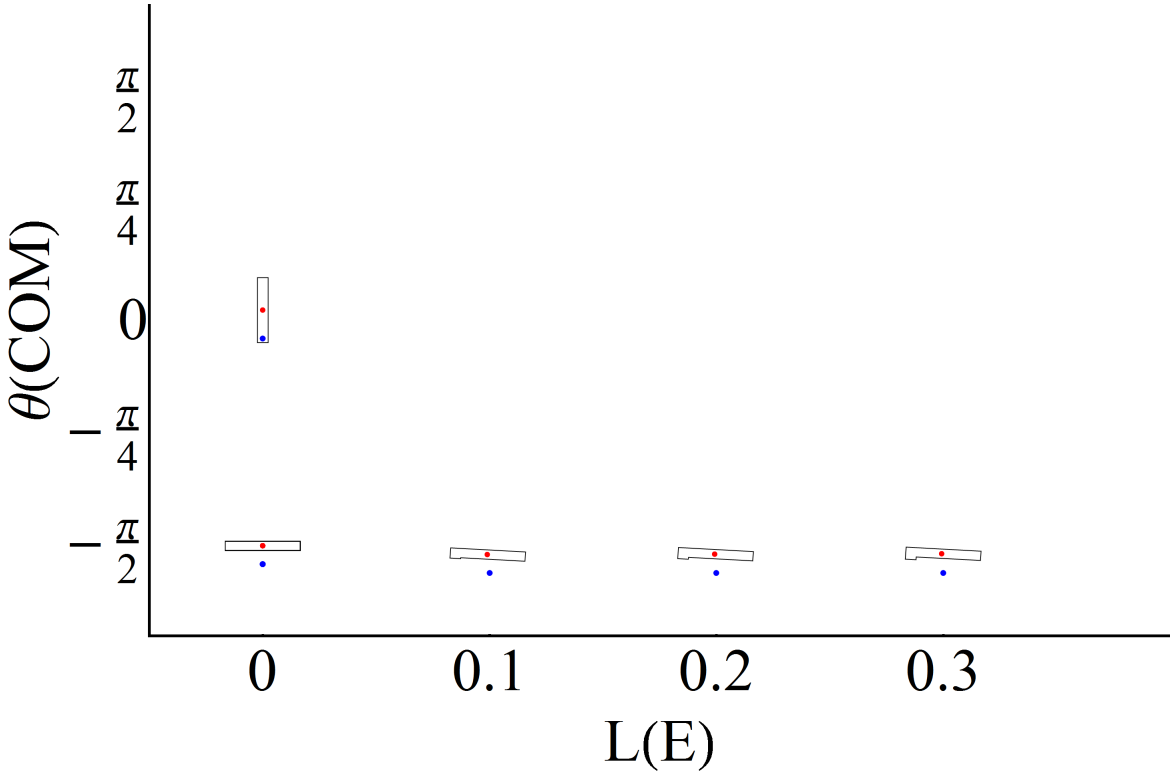

Figure 5.9: Trapping angle, rotated about the COM, as a function of leg length for shapes with $0 \leq L(E) \leq 0.3$. L(E) is the length of segment E, the red dot is the center of mass, and the blue dot is the focal point of the beam.

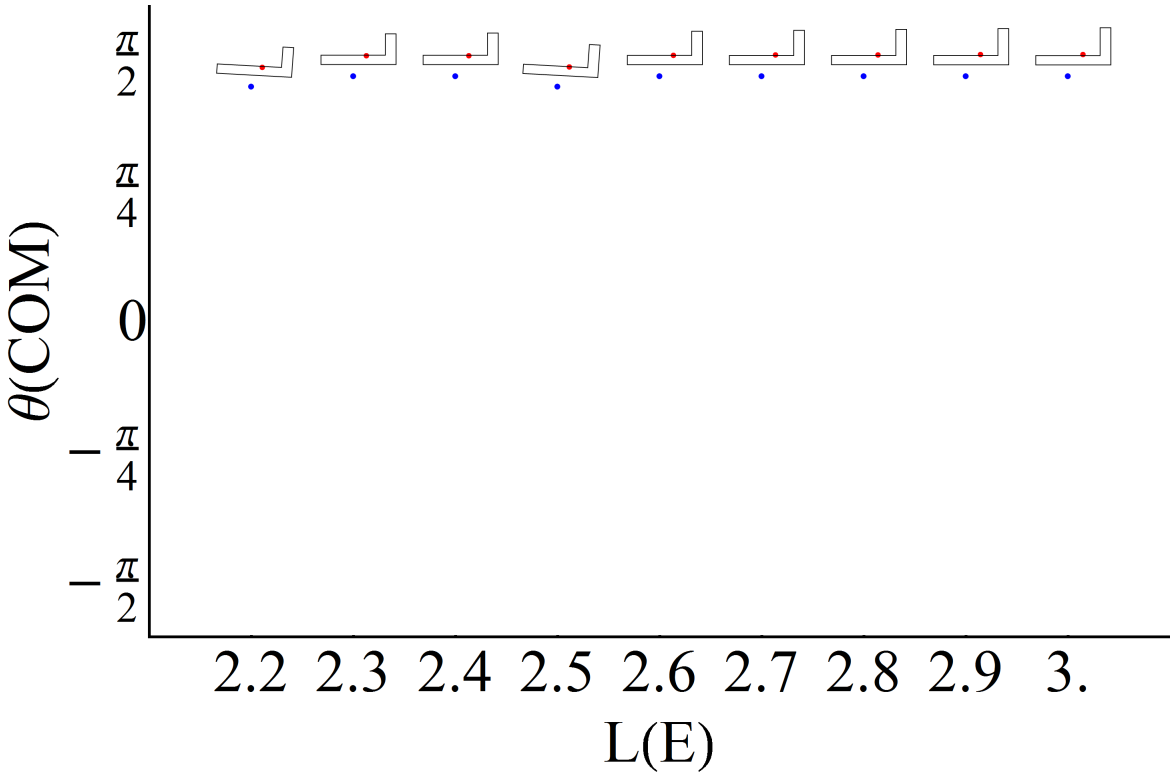

Figure 5.10: Trapping angle, rotated about the COM, as a function of leg length for shapes with $2.2 \leq L(E) \leq 3.0$. L(E) is the length of segment E, the red dot is the center of mass, and the blue dot is the focal point of the beam.

Referring to figure 5.11 we see somewhat stable trapping with the base slightly below the focal point of the beam for a slab with its long axis parallel to the direction of beam incidence, in agreement with the analytical derivation above. Figure 5.11b displays a well depth of approximately 70 $k_B t$. The ratio of the net work, for a closed integral about each point, to the potential in figure 5.11c shows values of $< 0.5\%$ in the region of stable trapping. Figure 5.11d displays a strong restoring torque following rotation of the shape about its center of mass in the $\pm\theta$ direction. In each of the following figures the white dot in (b) , (c) and (e) represents the position of the particle's center of mass and the purple arrow in (e) represents the direction of beam propagation.

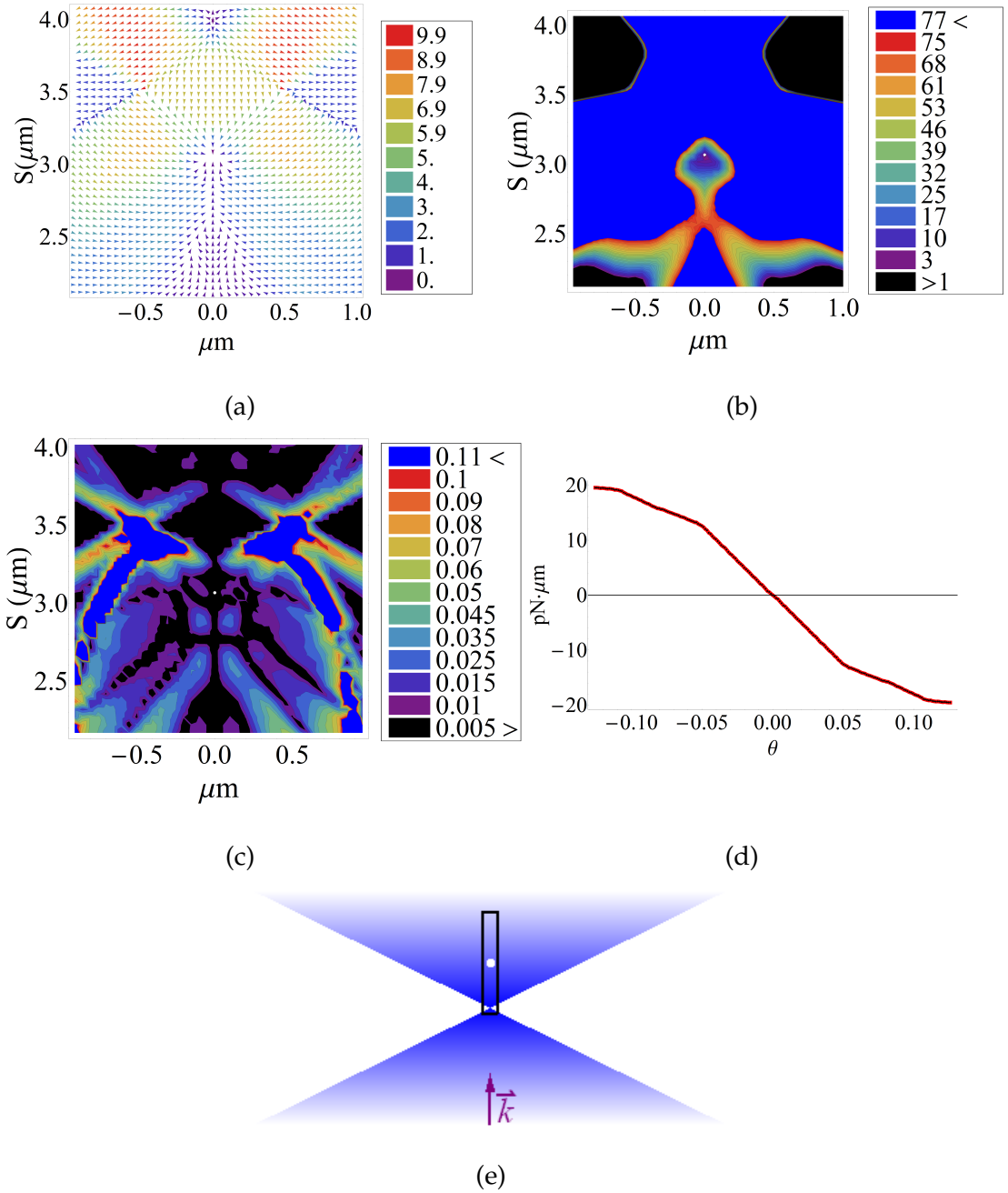

Figure 5.11: The trapping parameters for L(B) =7.0 μm and L(A) = 1.0 μm, oriented at $\theta = 0$. (a) The force field, units pN, and stable trapping with the particle's COM at position (0.0 μm, 3.1 μm) (b) the scalar potential, well depth $\approx 70\,k_BT$ (c) the net work normalized by the potential, with values of $< 0.5\%$ in the region of stable trapping (d) the torque about the particle's center of mass, with restoring torques reaching values of $\pm 20\,pN \cdot \mu m$ (e) An illustration of the shape in relation to the focal point of the beam.

Stable trapping is also found for the same shape, rotated about its center of mass by $\theta_{rot} = \frac{\pi}{2}$. The position of the shape, relative to the focal point once again matches that predicted analytically. The restoring torques, figure 5.12d, are understandably smaller than those found in the $\theta_{rot} = 0$ case, discussed previously. In the $\theta_{rot} = \frac{\pi}{2}$ a slight rotation in either direction is much less likely to change the path of an incident ray from intersecting parallel interfaces to intersecting perpendicular interfaces. The potential shows a depth of $\approx 80\,k_B T$ and the magnitude of the net work is $< 0.5\%$ of the potential.

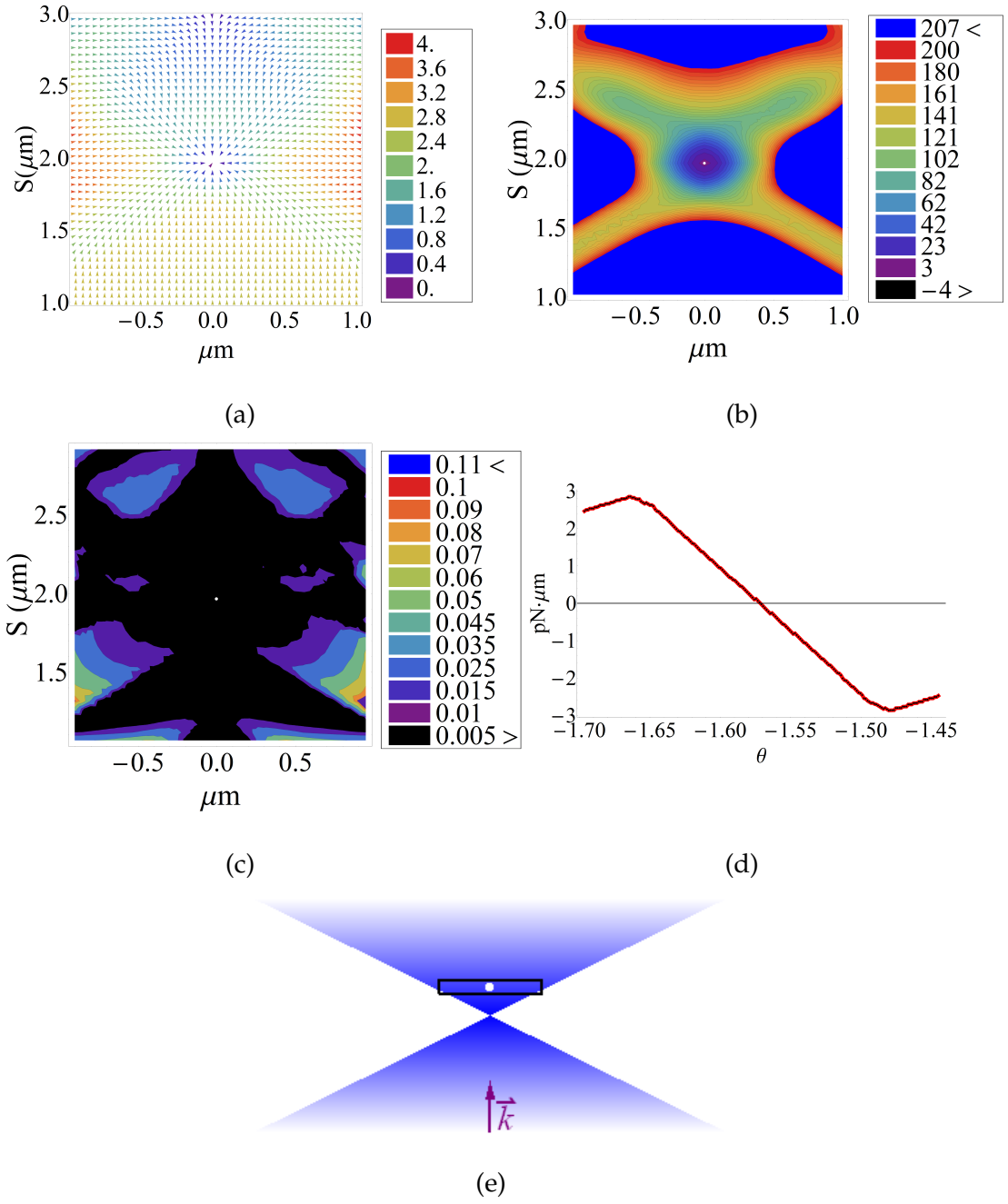

Figure 5.12: The trapping parameters for L(B)=7.0 μm and L(A)=1.0 μm, oriented at $\theta = \frac{\pi}{2}$. (a) The force field, units pN, showing stable trapping with the particle's COM at (0.0 μm, 2.0 μm) (b) the scalar potential, with a well depth of $\approx 80\,k_B T$, (c) the net work normalized by the potential, which is less than 0.5% in the region of stable trapping (d) the torque about the particles center of mass, with the restoring torque reaching values of $\pm 3\,pN \cdot \mu m$, (e) an illustration of the shape in relation to the focal point of the beam.

The addition of a small leg, breaking the rotational and geometric symmetry of the shape, has a direct effect on the shapes trapping behavior. Figures 5.13a, 5.14a and 5.15a illustrate a steady reduction in the gradient force along trapping axis of the particle; starting with a maximum value of $5.4\,pN$ for $L(E) = 0.1$ and leading to a maximum value of $5\,pN$ for $L(E) = 0.3$. Examination of the upper right quadrant of all three force vector fields shows a break in the symmetry of the force field directly correlated to the break in the shape symmetry. We note that while there is a shift of the stable trapping point off-axis with the addition of a small leg, this shift is due to the resulting change in the particle's COM; not a lateral shift of the particle. Rather than shifting the entire shape off-axis, to compensate for the additional leg, the particle's long axis remains centered over the focal point of the beam and the change in force is initially compensated for via rotation about the particle's center of mass. Each additional step in leg length results in an upward shift, along the beam axis. A steady increase in the restoring torque for rotation in the negative θ direction (counterclockwise) and corresponding decrease in the restoring torque for rotation in the positive θ direction is also observed in direct correlation to increasing leg length.

Positive θ rotation, for the small range of values allowed, corresponds to a greater number of rays that would have previously intersected the base and went on to intersect the parallel wall opposite, now intersecting the base and continuing on to intersect the perpendicular vertical wall on the right. This, as discussed previously, would result in a gradient force for each ray intersecting the perpendicular wall and lead to a negative restoring torque. At the opposite end of the shape increased leg length increases the probability of rays going through the two vertical parallel interfaces; increasing the scattering force in this section of the shape.

Negative θ rotation (clockwise) would place more of the base of the short

leg in the path of incident rays. Some of these rays will also go on to intersect a perpendicular wall, with the likelihood of perpendicular wall intersection decreasing as the leg length is increased. Once again rays entering the opposite side of the shape that, prior to rotation, would have intersected a perpendicular interface are now more likely to intersect the parallel interface directly opposite, leading to only a scattering force.

This qualitative description is bore out in figures 5.13d, 5.14d and 5.15d, where we see an increase in the restoring torque for positive rotation and a decrease in the restoring torque for negative rotation. The consistent increase in the restoring torque for positive rotation can be attributed to the relative areas of the regions interacting with the beam. The rightmost vertical wall is anywhere from 10 to ≈ 3 times the length of the leg. Changes in the orientation of the right vertical wall would therefore have a greater effect on the restoring torque. The relatively small scattering forces on the opposite end of the shape add to the restoring torque. For negative rotation increasing the leg length increases the number of rays that can experience two intersections with the vertical, parallel, segments of the leg, offsetting the gradient force. As the leg length is increased we see a steady decrease in the restoring torque for negative rotation.

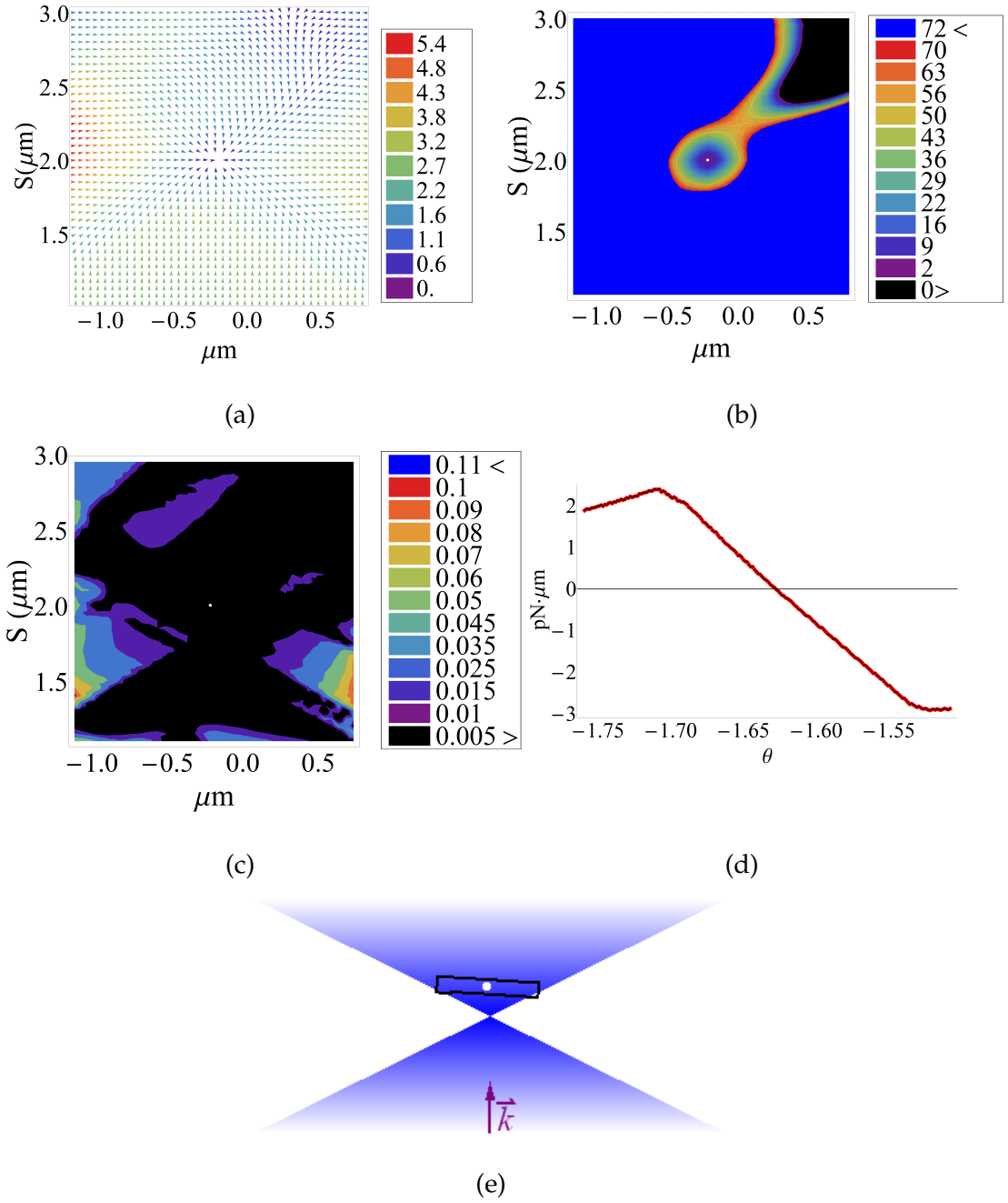

Figure 5.13: The trapping parameters for L(B) =7.0 μm and L(A)=1.1 μm, oriented at $\theta = -\frac{13\pi}{25}$. (a) The force field, units pN, displays stable trapping with the particle's COM at (-0.2 μm, 2.0 μm) (b) the scalar potential, well depth of $\approx 50\,k_B T$, (c) the ratio of the net work and the potential, which is less than 0.5% in the region of stable trapping (d) the torque about the particles center of mass, (e) an illustration of the shape relative to the focal point of the beam.

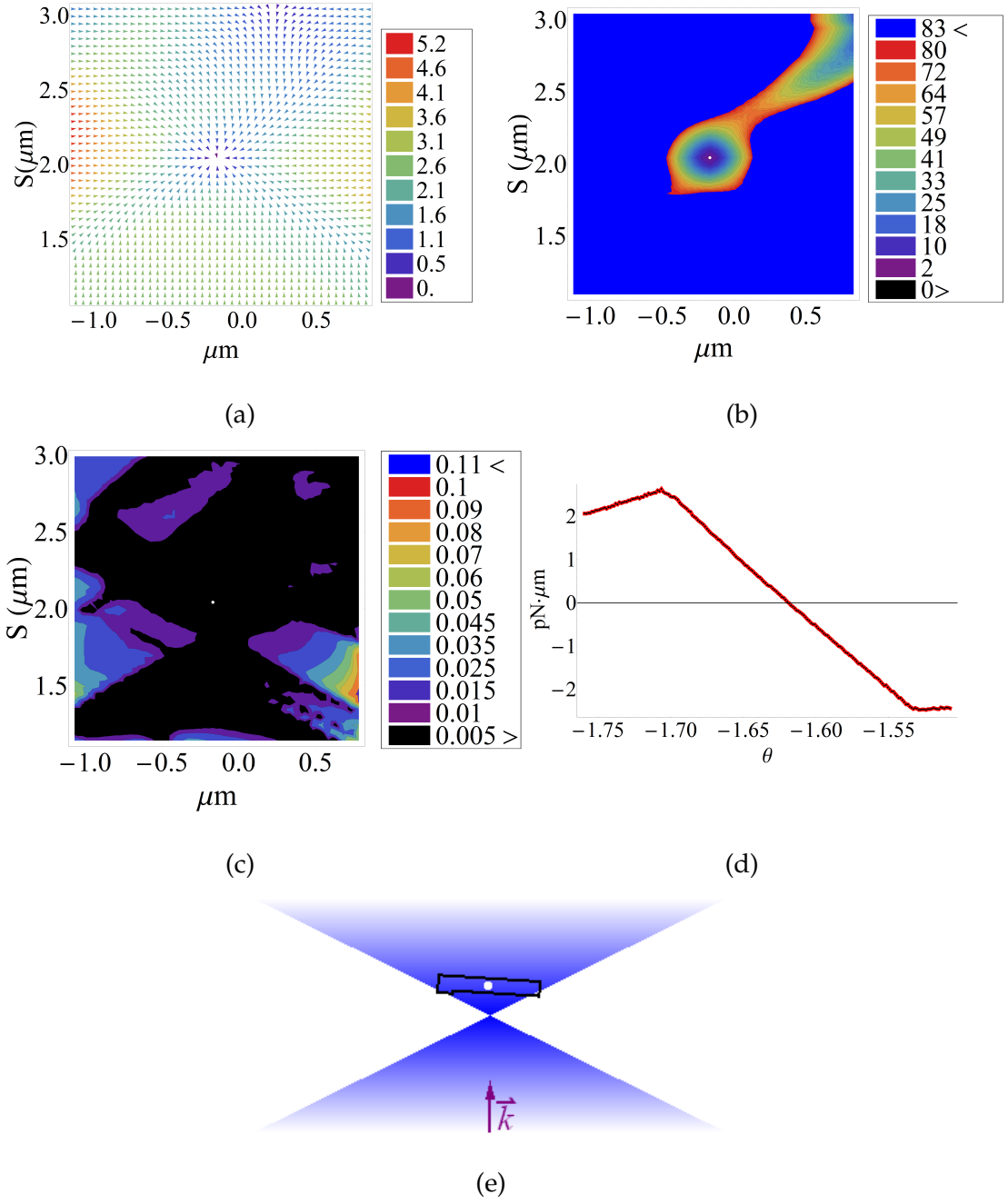

Figure 5.14: The trapping parameters for L(B)=7 μm and L(A)=1.2 μm, oriented at $\theta = -\frac{13\pi}{25}$. (a) The force field, units pN, displays stable trapping with the particle's COM at (-0.2 μm, 2.05 μm) (b) the scalar potential, well depth $\approx 60\,k_B T$, (c) the ratio of the net work and the potential, which is less than 0.5% in the region of stable trapping, (d) the torque about the particle's center of mass, (e) an illustration of the shape relative to the focal point of the beam.

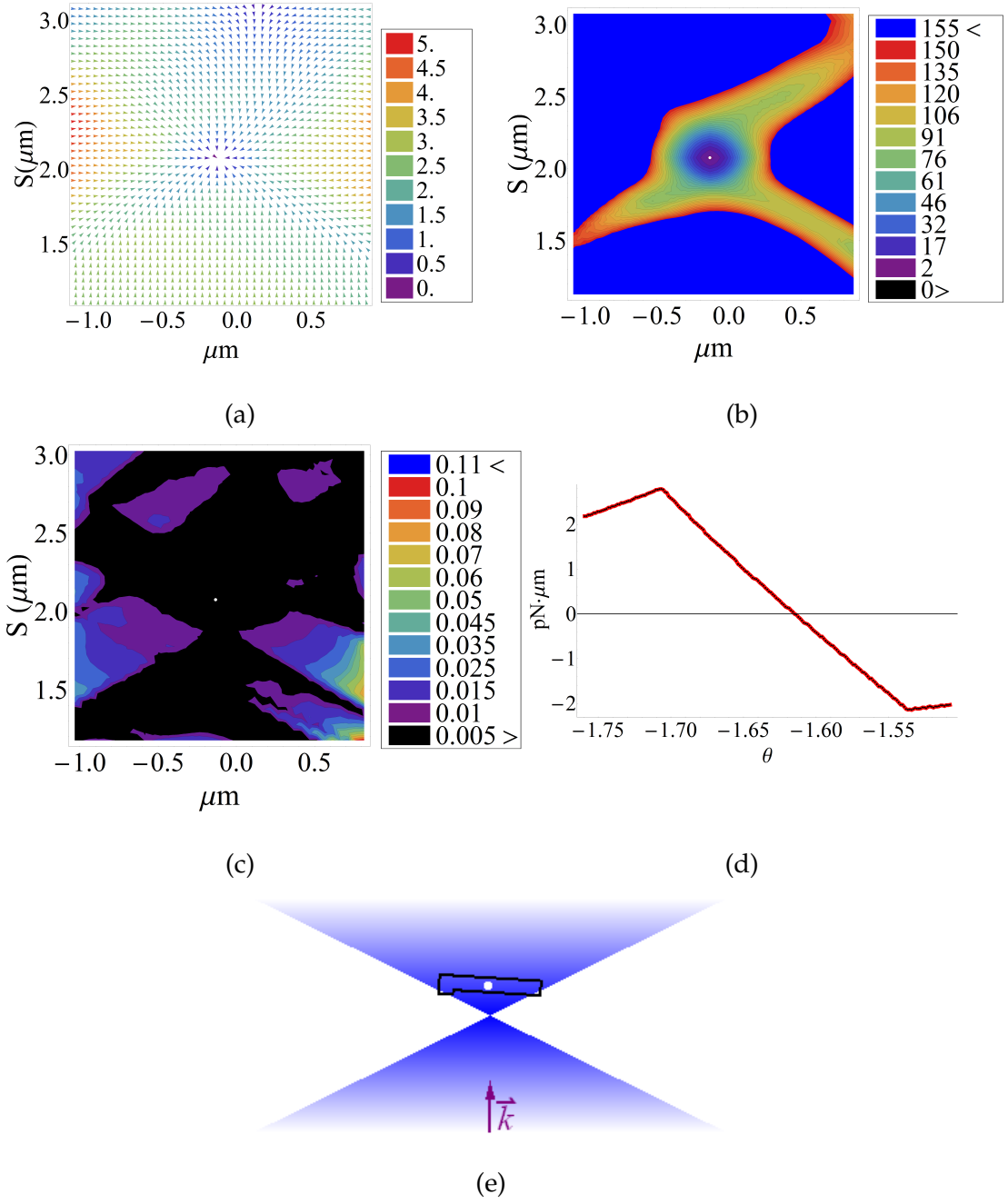

Figure 5.15: The trapping parameters for a slab, dimensions 7 μm by 1.3 μm, oriented at $\theta = -\frac{13\pi}{25}$. (a) The force field, units pN, displays stable trapping with the particle's COM at (-0.2μm, 2.10μm) (b) the scalar potential, well depth $\approx 80\,k_B T$, (c) the ratio of the net work and the potential, which is less than 0.5% in the region of stable trapping, (d) the torque about the particles center of mass, (e) an illustration of the shape relative to the focal point of the beam.

Shapes with L(A) greater than 1.3μm, but less than 3.2 μm showed no points of stable trapping. We see the first hints of stable trapping for the L(A)=3.2 μm case. While the potential well is rather shallow, $\Delta U = 13\, k_B T$ as is illustrated in figure 5.16b, we nevertheless see very low values for the net work normalized by the potential ($< 0.5\%$) and restoring torques of approximately $\pm 5\, pN \cdot \mu m$. We note that the force field, potential surface and torque were calculated for this geometry rotated about the center of mass by $\frac{\pi}{2}$ and no stable trapping was observed.

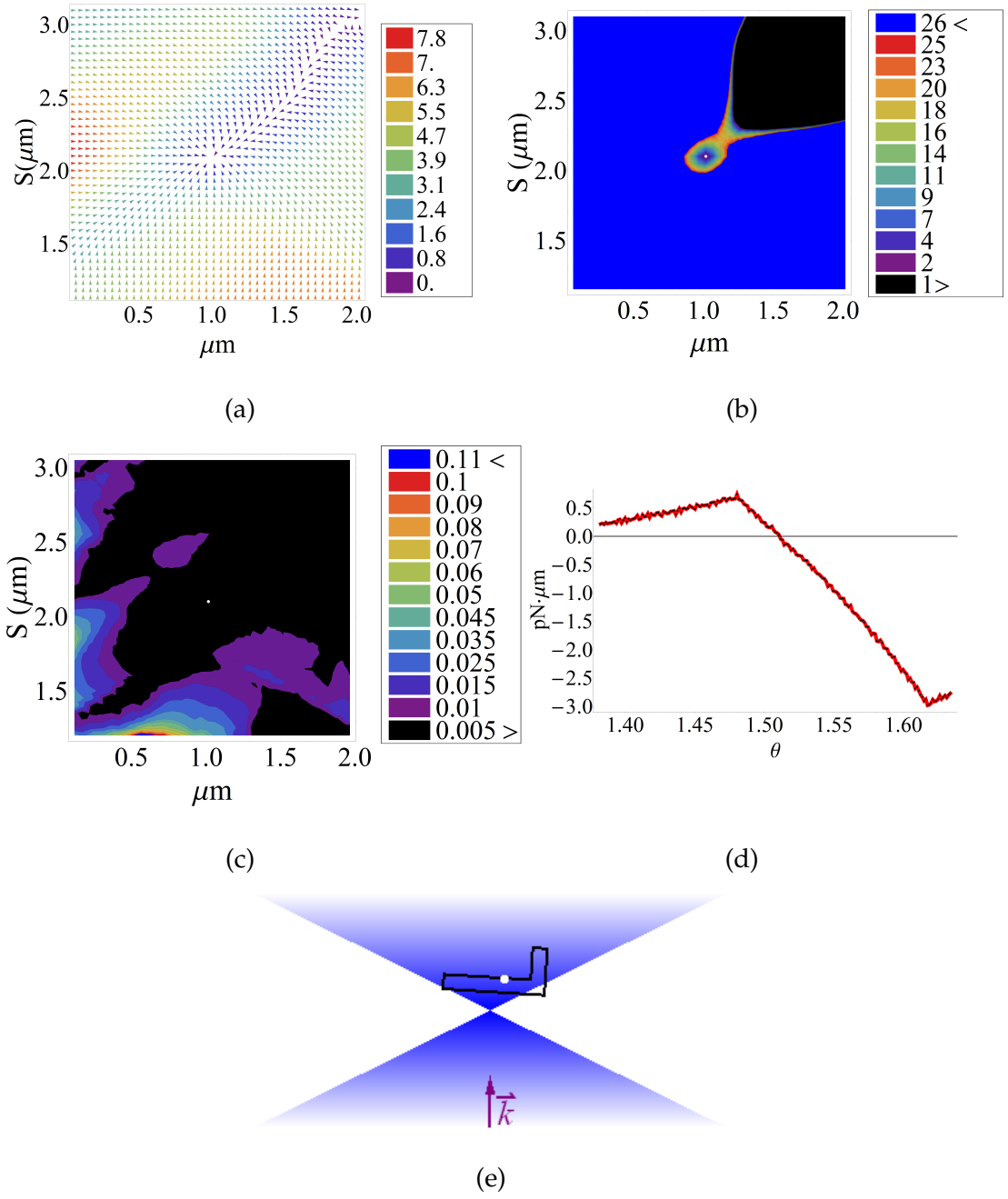

Figure 5.16: The trapping parameters L(B)=7.0 μm and L(A)=3.2 μm, oriented at $\theta = \frac{12\pi}{25}$. (a) The force field, units pN, displays stable trapping with the particle's COM at (1.0 μm, 2.1 μm), (b) the scalar potential, well depth $\approx 13\,k_BT$, (c) the ratio of the net work and the potential, which is less than 0.5% in the region of stable trapping, (d) the torque about the particles center of mass, with restoring torques of $\approx 0.5\,pN \cdot \mu m$, (e) an illustration of the shape relative to the focal point of the beam.

For shapes with L(A) greater than 3.3 μm, essentially the same behavior was observed across all leg lengths. This can be attributed to very small changes in the length of the leg relative to the total leg length. The orientation of the shape in its stable trapping positions, $\theta = \frac{\pi}{2}$, offers some insight into the increased restoring force for negative rotation and decreased restoring force for positive rotation. Negative rotation would result in some of the rays which previously would have passed through two parallel interfaces on the right side of the shape, shifted slightly to the right and gone on to intersect the vertical wall of the leg, now missing the leg entirely. This would lead to a decrease in the gradient force on that side. On the opposite end of the shape the vertical wall now becomes available for perpendicular intersections, leading to an increase in the gradient force in this region. If we recall that the shape is being rotated about its center of mass, represented by the red dot in figure 5.10, we see that fewer highly angled rays will enter on the right side. The critical angle must be less than the angle of incidence for perpendicular intersections not to result in total internal reflection; more of the rays will now, therefore, experience total internal reflection up the leg and exit via a parallel interface. This leads to a reduced gradient force and an increased scattering force. At the other end of the shape only scattering forces become possible, for large enough rotations, which would serve as a restoring force. The total restoring force for positive rotations is therefore much smaller than those found for negative rotation.

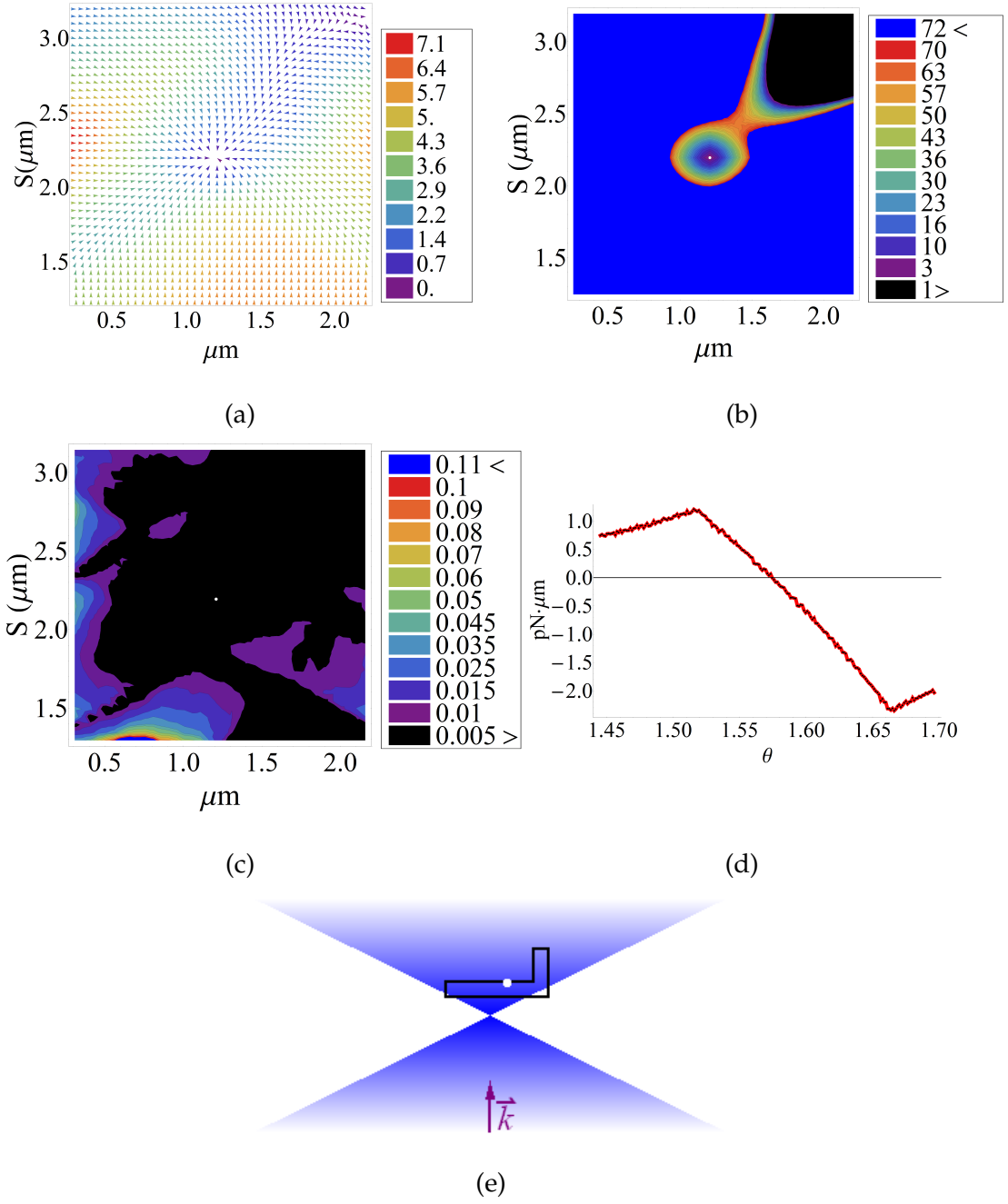

Figure 5.17: The trapping parameters for L(B)=7 μm and L(A)=3.3 μm, oriented at $\theta = \frac{\pi}{2}$. (a) The force field, units pN, with stable trapping displayed at position (1.2 μm, 2.4 μm) (b) the scalar potential, well depth $\approx 60\,k_B T$, (c) the ratio of the net work and the potential, which is less than 0.5% in the region of stable trapping, (d) the torque about the particles center of mass, with restoring torques greater than $1.0\,pN \cdot \mu m$ in magnitude, (e) an illustration of the shape relative to the focal point of the beam.

5.7 Shape geometry and trapping behavior

In the previous chapter we established that neglecting diffraction plays a definite role in the geometric optics calculation's inability to reproduce the reentrant trapping found by Wilking and collaborators, due to overestimation of the scattering force. From comparison of the scattering force calculated using the full physical optics solution and that found using geometric optics we observed that diffraction could not be the only contributing factor; geometry must play a role as well.

In this chapter we illustrated the role parallel or perpendicular interfaces play in the trapping behavior of a shape. It is exactly these perpendicular interfaces, which do not exist in a circular shape, which make reentrant trapping possible for Wilking's shape. This effect of perpendicular interfaces is first illustrated in figure 5.11. Figure 5.18 reproduces both the image of the particle which experiences reentrant trapping and the image of the vertical slab, described previously, in its stable trapping position relative to the focal point of the beam.

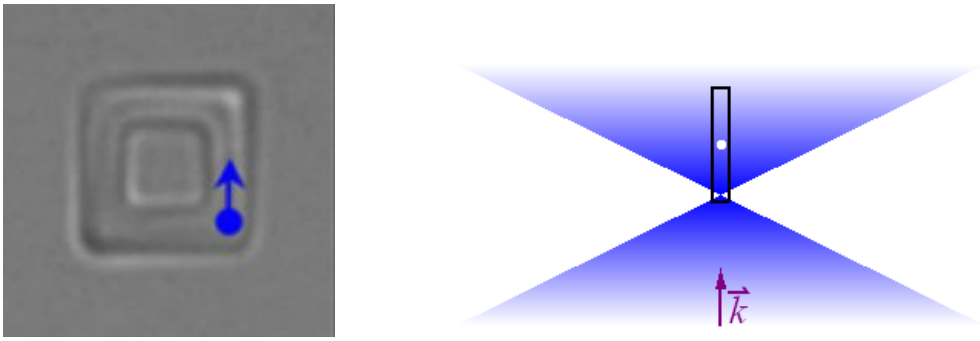

(a) (b)

Figure 5.18: (a) Wilking's shape which displays reentrant trapping, the blue circle denotes the focal point and the blue arrow the direction of beam incidence.(b) The stable trapping position of a vertical slab relative to the focal point of the beam

Rotating the reentrant trapping shape, figure 5.18a, about the beam axis by $\frac{\pi}{2}$, we essentially have a dielectric rod. We see from figure 5.18b stable trapping does occur for this geometry, with the stable trapping point at approximately the same position found experimentally by Wilking and collaborators. Considering the problem in three dimensions we see the reentrant trapping particle is not simply a dielectric rod, there are non-symmetric features at the top and bottom of the shape which were shown previously to cause rotation of the two dimensional shape about its center of mass, so that the long axis lies perpendicular to the direction of beam incidence. Why then would the shape not trap with the focal point of the beam exactly in the center of the particle cavity? We know from experimental results that this is not the case and examination of two shapes with similar geometry offers some insight.

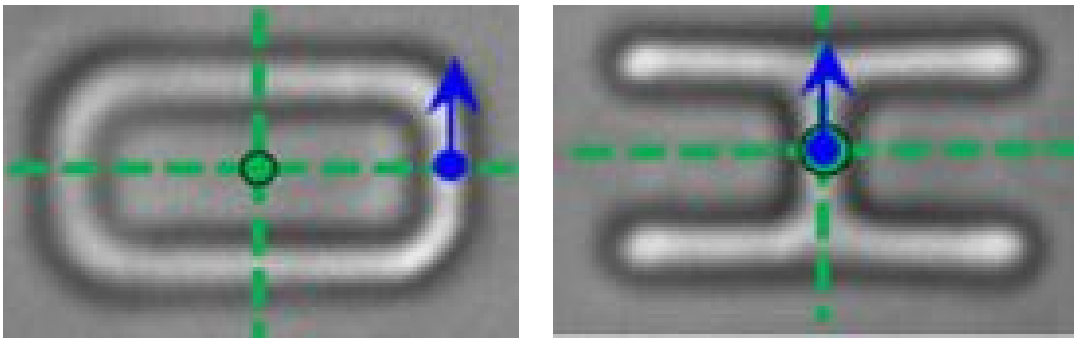

(a) (b)

Figure 5.19: (a) A colloidal dielectric O shape and (b) H shape stably trapped by Wilking and collaborators. Blue circles denote the focal point of the beam, blue arrows the direction of beam incidence, green circles twofold rotation axis and green dashed lines mirror planes for each particle

As outlined in this chapter, the key to gradient forces for planar particles is intersections of the incident ray with two perpendicular interfaces. From the ray optics standpoint a plank like shape with its long axis oriented perpendicular to the direction of beam incidence stable trapping can only occur

in positions above the focal point of the beam. For positions below the focal point of the beam scattering forces will dominate as the bulk of the incident rays will pass through two parallel interfaces. If the slab is oriented vertically a larger fraction of the incident rays will, after intersecting the relatively small base of the shape, go on to intersect a perpendicular interface.

The O shape shown in figure 5.19a is an example of a particle with both trapping options available. If the particle were shifted so that the focal point of the beam was directly at the point of twofold rotation in the center of the particle, the bulk of the incident rays would only interact with the two long legs of the shape. While the long leg located above the beam axis in this position could contribute to the trapping forces, it can only do so via the intersection of a ray leaving the lower leg with a perpendicular interface. Additionally any trapping forces the upper leg could contribute would have to overcome the scattering forces for the portion of the shape positioned below the focal point of the beam.

In the experimentally observed trapping position the bulk of the scattering interfaces are shifted out of path of the beam, with the shorter leg positioned along the beam axis. In this position, from the ray optics standpoint, rays on the left side of the beam axis would intersect the base of the shape, pass through two parallel interfaces and go on to intersect a perpendicular interface. As these rays are moving from lower to higher index the refracted ray intersecting a perpendicular interface will bend inward towards the unit normal, resulting in a contribution to the scattering force. Rays entering the shape on the opposite side will intersect two parallel interfaces and go on to intersect a perpendicular interface at the top of the shape. The refracted ray at this interface will once again bend inwards toward the unit normal. This inward bend will result in a contribution to the gradient force. The particle traps with one of its symmetry planes parallel to the focal point of the beam and at this

position we see that an equal portion of rays can follow the opposite paths described. This serves to not only balance the forces on the particle but to balance the torques as well. The long leg at the base of the shape experiences a net force in the direction of beam incidence. The long leg at the top experiences a net force in the opposite direction.

The H shape, figure 5.19b has a geometry which makes it possible to take advantage of both the gradient forces resulting from positioning a long plank oriented perpendicular to the direction of beam incidence above the focal point of the beam and rays which intersect the base of the H and go on to internally intersect the vertical wall of the shape. These combined gradient forces are sufficient to overcome the scattering force resulting from the lower leg being positioned below the focal point of the beam.

5.7.1 Reentrant trapping

As we have shown the trapping behavior of a variety of shapes can be understood and correctly predicted from the geometric ray optics standpoint. In the limit that any of the characteristic particle dimensions are on the order of the wavelength of the incident radiation we find overestimation of the scattering force on the part of ray optics by as much as a factor of two. This overestimation of the scattering force is not however solely responsible for our geometric ray optics inability to reproduce the reentrant trapping result using the shapes discussed in chapter 3. We see that to fully understand the trapping behavior of any shape one must investigate all of the characteristic geometries which together make the three dimensional object being studied. Additionally, a square with rounded edges cannot be approximated as a circle.

Circles, spheres or cylinders are often used to approximate similar geometries as their symmetry leads to much greater simplicity in the development

of analytic solutions to describe the scattering or trapping behavior of these shapes. As experimentalists fabricate ever more complicated micron scale particles, closed form analytic solutions appropriate for these geometries either do not exit or become intractable in their development. As our modified geometric optics numerical simulation only requires input of the bounds of the shape being investigated and, within the limits of particle dimensions on the order of the wavelength of incident light, returns accurate results our approach is attractive both for its simplicity and its ability to calculate the forces on more complicated shape geometries.

CHAPTER 6

Conclusions

In this dissertation we have presented a modified geometric optics calculation which can be used for any geometry. The trapping behavior for both the cross section of a pair of infinite concentric cylinders and a two dimensional planar shape was examined. These geometries allowed investigation of the effects of particle geometry, characteristic particle dimensions and particle symmetry on trapping behavior. We find that our modified numerical geometric optics approach successfully reproduces the results of Ashkin's closed form solution when applied to solid circular dielectric particles.

For circular particles with outer dimensions on length scales in the geometric optics regime, but inner features on the length scale of the incident wavelength of light we find that geometric optics overestimates the scattering force by as much as a factor of two. In the comparison between an experimentally trapped planar dielectric particle with a small cavity and a two dimensional shape we find we are able to reproduce the on-axis trapping, including the metastable trapping, experimentally observed. We find however, an overestimation of the scattering force on the part of the geometric optics calculation, which results in the trapping points located by our simulation being shifted up, along the beam axis, from trapping points observed experimentally . We are not able to reproduce reentrant trapping observed by Wilking and collaborators for a square "ring" using a circular geometry.

We attribute this lack of agreement to both diffraction and particle geom-

etry. As geometric optics does not account for diffraction the scattering force experienced by the particle in geometric optics, especially in the case of the particle dimensions being examined, serves to wash out possible metastable trapping points. Geometry also plays a large role in this particular disagreement between the results of the geometric optics simulation and Wilking's experimental observations. The particle which displayed reentrant trapping is planar and therefore has perpendicular interfaces. As was shown both analytically and numerically these perpendicular interfaces contribute greatly to the trapping of the particle. Simulations of the trapping of a two dimensional rectangular shape, which mimics the secondary geometry of the reentrant trapping particle, shows that the modified geometric optics approach is able to reproduce this trapping point and that the net torque at this position is zero.

Bibliography

[1] Ashkin, A. Forces of a single-beam gradient laser trap on a dielectric sphere in the ray optics regime. *Methods Cell Biol* **1998**, *55*, 1–27.

[2] Ashkin, A. Acceleration and trapping of particles by radiation pressure. *Physical Review Letters* **1970**, *24*, pp. 156–159.

[3] Grier, D. G. A revolution in optical manipulation. *Nature* **2003**, *82*, 3985–3987.

[4] Smith, D.; Tans, S. J.; Smith, S.; Grimes, S.; Anderson, D.; Bustamante, C. The bacteriophage ϕ29 portal motor can package DNA against a large external force. *Nature* **2001**, *413*, 748 – 752.

[5] Kuo, S.; Sheetz, M. P. Force of single kinesin molecules measured with optical tweezers. *Science* **1993**, *260*, 232 –234.

[6] Tan, Y.; Sun, D.; Wang, J.; Huang, W. Mechanical Characterization of Human Red Blood Cells Under Different Osmotic Conditions by Robotic Manipulation With Optical Tweezers. *Biomedical Engineering, IEEE Transactions on* **2010**, *57*, 1816 –1825.

[7] Selhuber-Unkel, C.; Zins, I.; Schubert, O.; C., S.; Oddershede, L. B. Quantitative Optical Trapping of Single Gold Nanorods. *Nano Letters* **2008**, *8*, 2998–3003, PMID: 18720978.

[8] Bar-Ziv, A.; Moses, E.; Nelson, P. Dynamic excitations in membranes induced by optical tweezers. *Biophys J* **1998**, *75*, 294–320.

[9] Wilking, J. N.; Mason, T. G. Multiple trapped states and angular Kramers hopping of complex dielectric shapes in a simple optical trap. *Europhysics Letters* **2008**, *81*, 58005.

[10] Dufresne, E. R.; Grier, D. G. Optical tweezer arrays and optical substrates created with diffractive optics. *Review of Scientific Instruments* **1998**, *69*, 1974–1977.

[11] Dufresne, E. R.; Spalding, G. C.; Dearing, M. T.; Sheets, S. A.; Grier, D. G. Computer-generated holographic optical tweezer arrays. *Review of Scientific Instruments* **2001**, *72*, 1810–1816.

[12] Lee, S. H.; Grier, D. G. Holographic microscopy of holographically trapped three-dimensional structures. *Opt. Express* **2007**, *15*, 1505–1512.

[13] Hörner, F.; Woerdemann, M.; Mller, S.; Maier, B.; Denz, C. Full 3D translational and rotational optical control of multiple rod-shaped bacteria. *Journal of Biophotonics* **2010**, *3*, 468–475.

[14] Sasaki, K.; Koshioka, M.; Misawa, H.; Kitamura, N.; Masuhara, H. Pattern formation and flow control of fine particles by laser-scanning micromanipulation. *Opt. Lett.* **1991**, *16*, 1463–1465.

[15] Nambiar, R.; Meiners, J.-C. Fast position measurements with scanning line optical tweezers. *Opt. Lett.* **2002**, *27*, 836–838.

[16] Speidel, M.; Friedrich, L.; Rohrbach, A. Interferometric 3D tracking of several particlesin a scanning laser focus. *Opt. Express* **2009**, *17*, 1003–1015.

[17] Gahagan, K.; Swartzlander, G. Simultaneous trapping of low-index and high-index microparticles observed with an optical-vortex trap. *Journal of the Optical Society of America, B. 16*.

[18] Eckerskorn, N.; Zeng, N.; Shvedov, V.; Krolikowski, W.; Rode, A. Effect of polarization on transport of particles in air by optical vortex beam. *Journal of Optics A: Pure and Applied Optics* **2012**, *14*, 055302–055307.

[19] Gahagan, K.; Swartzlander, G. Trapping of low-index microparticles in an optical vortex. *Journal of the Optical Society of America, B. 15*.

[20] Arlt, J.; Garces-Chavez, V.; Sibbett, W.; Dholakia, K. Optical micromanipulation using a Bessel light beam. *Optics Communications* **2001**, *197*, 239 – 245.

[21] Milne, G.; Dholakia, K.; McGloin, D.; Volke-Sepulveda, K.; Zemánek, P. Transverse particle dynamics in a Bessel beam. *Opt. Express* **2007**, *15*, 13972–13987.

[22] Ahluwalia, B.; Lø vhaugen, P.; Hellesø, O. Waveguide trapping of hollow glass spheres. *Optics Letters 36*.

[23] Gustafson, B. A. S. In *Light Scattering Reviews 4*; Kokhanosvsky, A. A., Ed.; Praxis Publishing Ltd, 2009; p 6.

[24] Mazolli, A.; Maia Neto, P. A.; Nussenzveig, H. M. Theory of trapping forces in optical tweezers. *Proceedings of the Royal Society of London. Series A: Mathematical, Physical and Engineering Sciences* **2003**, *459*, 3021–3041.

[25] Neves, A. A. R.; Fontes, A.; de Y. Pozzo, L.; de Thomaz, A. A.; Chillce, E.; Rodriguez, E.; Barbosa, L. C.; Cesar, C. L. Electromagnetic forces for an arbitrary optical trapping of a spherical dielectric. *Opt. Express* **2006**, *14*, 13101–13106.

[26] Hu, Y.; Nieminen, T. A.; Bickford, L. R.; Drezek, R. A. Concentric Sphere Mie Theory Model: Applications to Nanoshell Spectra Prediction and Design of Anti-Reflection Coatings for Optical Traps. 2008; `http://www.opticsinfobase.org/abstract.cfm?URI=BIOMED-2008-BTuF12`.

[27] Ren, K. F.; Gréhan, G.; Gouesbet, G. Scattering of a Gaussian beam by

an infinite cylinder in the framework of generalized Lorenz–Mie theory: formulation and numerical results. *J. Opt. Soc. Am. A* **1997**, *14*, 3014–3025.

[28] Boyde, L.; Ekpenyong, A.; Whyte, G.; Guck, J. Comparison of stresses on homogeneous spheroids in the optical stretcher computed with geometrical optics and generalized Lorenz-Mie theory. *Appl. Opt.* **2012**, *51*, 7934–7944.

[29] Purcell, E. M.; Pennypacker, C. R. Scattering and Absorption of Light by Nonspherical Dielectric Grains. *The Astrophysical Journal* **1973**, *186*, 705 – 714.

[30] Yurkin, M.; Hoekstra, A. The discrete dipole approximation: An overview and recent developments. *Journal of Quantitative Spectroscopy and Radiative Transfer* **2007**, *106*, 558 – 589, IX Conference on Electromagnetic and Light Scattering by Non-Spherical Particles.

[31] Hoekstra, A. G.; Frijlink, M.; Waters, L. B. F. M.; Sloot, P. M. A. Radiation forces in the discrete-dipole approximation. *J. Opt. Soc. Am. A* **2001**, *18*, 1944–1953.

[32] Kimura, H.; Mann, I. Radiation Pressure Cross Section for Fluffy Aggregates. *J. Quant. Spectrosc. Radiat. Transfer* **1998**, *60*, 425–438.

[33] Nieminen, T.; Rubinsztein-Dunlop, H.; Heckenberg, N. Calculation and optical measurement of laser trapping forces on non-spherical particles. *Journal of Quantitative Spectroscopy and Radiative Transfer* **2001**, *70*, 627 – 637, Light Scattering by Non-Spherical Particles.

[34] Wong, V.; Ratner, M. A. Explicit computation of gradient and nongradient contributions to optical forces in the discrete-dipole approximation. *J. Opt. Soc. Am. B* **2006**, *23*, 1801–1814.

[35] Smith, P.; Ashkin, A.; Tomlinson, W. Four-wave mixing in an artificial Kerr medium. *Optics Letters 6*.

[36] Roosen, G.; Imbert, C. Optical Levitation by Means of Two Horizontal Laser Beams: A Theoretical and Experimental Study. *Physics Letters 59A*.

[37] Ashkin, A. Forces of a single-beam gradient laser trap on a dielectric sphere in the ray optics regime. *Biophys J* **1992**, *61*, 569–582.

[38] Van de Hulst, H. *Light Scattering by Small Particles*; Dover Publications, Inc, 1981.

[39] Gauthier, R. C.; Wallace, S. Optical levitation of spheres: analytical development and numerical computations of the force equations. *J. Opt. Soc. Am. B* **1995**, *12*, 1680–1686.

[40] Kim, S. B.; Kim, S. S. Radiation forces on spheres in loosely focused Gaussian beam: ray-optics regime. *J. Opt. Soc. Am. B* **2006**, *23*, 897–903.

[41] Lee, K. S.; Yoon, S. Y.; Lee, K. H.; Kim, S. B.; Sung, H. J.; Kim, S. S. Radiation forces on a microsphere in an arbitrary refractive index profile. *J. Opt. Soc. Am. B* **2012**, *29*, 407–414.

[42] Oeder, A.; Stoebenau, S.; Sinzinger, S. Optimized free-form optical trapping systems. *Opt. Lett.* **2012**, *37*, 274–276.

[43] Zhou, J.-H.; Ren, H.-L.; Cai, J.; Li, Y.-M. Ray-tracing methodology: application of spatial analytic geometry in the ray-optic model of optical tweezers. *Appl. Opt.* **2008**, *47*, 6307–6314.

[44] MacDonald, M.; Paterson, L.; Sibbett, W.; Dholakia, K.; Bryant, P. Trapping and manipulation of low-index particles in a two-dimensional interferometric optical trap. *Optics Letters 26*.

[45] Garcés-Chávez, V.; Volke-Sepulveda, K.; Chávez-Cerda, W., S.and Sibbett; Dholakia, K. Transfer of orbital angular momentum to an optically trapped low-index particle. *Physical Review A* **2002**, *66*, 063402.

[46] Gauthier, R. C. Laser-Trapping Properties of Dual-Component Spheres. *Appl. Opt.* **2002**, *41*, 7135–7144.

[47] Rodrigo, P.; Daria, V.; Glückstad, J. Real-time interactive optical micromanipulation of a mixture of high- and low-index particles. *Optics Express* **2004**, *12*, 1417–1425.

[48] Lee, K. H.; Kim, S. B.; Yoon, S. Y.; Lee, K. S.; Jung, J. H.; Sung, H. J. Behavior of Double Emulsions in a Cross-Type Optical Separation System. *Langmuir* **2012**, *28*, 7343–7349.

[49] Kim, S. B.; Lee, K. H.; Kim, S. S.; Sung, H. J. Optical force on a pair of concentric spheres in a focused laser beam: ray-optics regime. *J. Opt. Soc. Am. B* **2012**, *29*, 2531–2541.

[50] Cherney, D. P.; Bridges, T. E.; Harris, J. M. Optical Trapping of Unilamellar Phospholipid Vesicles: Investigation of the Effect of Optical Forces on the Lipid Membrane Shape by Confocal-Raman Microscopy. *Analytical Chemistry* **2004**, *76*, 4920–4928, PMID: 15373424.

[51] Bendix, P. M.; Oddershede, L. B. Expanding the Optical Trapping Range of Lipid Vesicles to the Nanoscale. *Nano Letters* **2011**, *11*, 5431–5437.

[52] Gauthier, R. C. Theoretical investigation of the optical trapping force and torque on cylindrical micro-objects. *J. Opt. Soc. Am. B* **1997**, *14*, 3323–3333.

[53] Simpson, S. H.; Hanna, S. Optical trapping of microrods: variation with size and refractive index. *J. Opt. Soc. Am. A* **2011**, *28*, 850–858.

[54] Simpson, S. H.; Hanna, S. Holographic optical trapping of microrods and nanowires. *J. Opt. Soc. Am. A* **2010**, *27*, 1255–1264.

[55] Ashkin, A.; Dziedzic, J. M. Optical Trapping and Manipulation of Viruses and Bacteria. *Science* **1987**, *235*, pp. 1517–1520.

[56] Zhou, J.-H.; Zhong, M.-C.; Wang, Z.-Q.; Li, Y.-M. Calculation of optical forces on an ellipsoid using vectorial ray tracing method. *Opt. Express* **2012**, *20*, 14928–14937.

[57] Sraj, I.; Szatmary, A. C.; Marr, D. W. M.; Eggleton, C. D. Dynamic ray tracing for modeling optical cell manipulation. *Opt. Express* **2010**, *18*, 16702–16714.

[58] Bohren, C. F.; Huffman, D. R. *Absorption and Scattering of Light by Small Particles*; John Wiley & Sons, 1983.

[59] Born, M.; Wolf, E. *Principles of Optics: Electromagnetic Theory of Propagation, Interference and Diffraction of Light*; Cambridge University Press, 1999.

[60] Keller, J. B. Geometrical Theory of Diffraction. *Journal of the Optical Society of America* **1962**, *52*, 116–130.

[61] Jackson, J. D. *Classical Electrodynamics, 3rd Edition*; John Wiley & Sons, Inc, 1999.

[62] Perkins, T. T.; Quake, S. R.; Smith, D. E.; Chu, S. Relaxation of a Single DNA Molecule Observed by Optical Microscopy. *Science* **1994**, *264*, pp. 822–826.

[63] Quake, S.; Babcock, H.; Chu, S. The dynamics of partially extended single molecules of DNA. *Nature* **1997**, *388*, 151–154.

[64] Volke-Sepúlveda, K.; Chávez-Cerda, S.; Garcés-Chávez, V.; Dholakia, K. Three-dimensional optical forces and transfer of orbital angular momentum from multiringed light beams to spherical microparticles. *J. Opt. Soc. Am. B* **2004**, *21*, 1749–1757.

[65] Ramsay, W. T.; Bechu, M.; Bolanos Quinones, V. A.; Mei, Y.; Schmidt, O. G.; Paterson, L. Triple beam optical trap for microsyringe construction. **2011**, 809708–809708–9.

[66] Kasarova, S. N.; Sultanova, N. G.; Ivanov, C. D.; Nikolov, I. D. Analysis of the dispersion of optical plastic materials. *Optical Materials* **2007**, *29*, 1481 – 1490.

[67] Daimon, M.; Masumura, A. Measurement of the refractive index of distilled water from the near-infrared region to the ultraviolet region. *Appl. Opt.* **2007**, *46*, 3811–3820.

[68] Flatau, P.; Draine, B. Discrete-dipole approximation for scattering calculations. *J. Opt. Soc. Am. A* **1994**, *11*, 1491.

[69] Lock, J. A.; Gouesbet, G. Rigorous justification of the localized approximation to the beam-shape coefficients in generalized Lorenz-Mie theory. I. On-axis beams. *J. Opt. Soc. Am. A* **1994**, *11*, 2503–2515.

[70] Sakurai, J. *Modern Quantum Mechanics*; Pearson Education, 2006.

[71] Kerker, M.; Matijević, E. Scattering of Electromagnetic Waves from Concentric Infinite Cylinders. *J. Opt. Soc. Am.* **1961**, *51*, 506–508.